Dissertation
submitted to the
Combined Faculty of Mathematics, Engineering and Natural Sciences
of Heidelberg University, Germany
for the degree of
Doctor of Natural Sciences

Put forward by

M. Sc. Felix Harald Herrmann
born in Bad Friedrichshall (Germany)

Oral examination: 7th of May, 2025

Setup of a Reaction Microscope for the Cryogenic Storage Ring CSR and first Measurements

Referees:

Prof. Dr. Thomas Pfeifer
Priv.-Doz. Dr. Wolfgang Quint

Aufbau eines Reaktionsmikroskops für den kryogenen Speicherring CSR und erste Messungen

Diese Arbeit beschreibt den Aufbau des ersten kryogenen Reaktionsmikroskops, einer neuen experimentellen Aperatur im kryogenen Speicherring CSR. Die zentralen technischen Komponenten des Reaktionsmikroskops werden beschrieben. Eine Auswahl von ersten Experimenten wird vorgestellt.
Die Photo-Elektronen-Ablösung von CH^- wird untersucht um Photo-Elektron Spektroskopie zu demonstrieren. Alle sichtbaren Strukturen konnten bekannten Übergängen vom molekularen Ion zum Neutralen zugeordnet werden.
Die Si^- + Ar Kollision wird als Beispiel einer Interaktion zwischen einem negativen Ion und einem neutralen Target angeführt. Die korrelierte Interaktion zwischen dem Projektil und Target Elektron wird als der Prozess für Elektronenablösung mit gleichzeitiger Targetionisation identifiziert. Das gemessene Verhältnis der Streuquerschnitte mit und ohne gleichzeitige Targetionisation liegt eine Größenordnung über dem erwarteten Wert.
Der Elektronentransfer von einem neutralen He, Ne oder Ar Target auf ein Ar^+ Projektil wurde mit positivem Ionenstrahl untersucht. Übergänge in den Grundzustand und in angeregte Zustände des Projektils konnten für alle Targets bestimmt werden. Zusätzlich sieht man Targetübertragungsanregung für Argon und Elektronenübertrag in metastabile Ar^+ Zustände mit Helium und Neon Target. Der Projektil Streuwinkel wird durch Impulsübertrag auf das Rückstoßion bestimmt.

Setup of a Reaction Microscope for the Cryogenic Storage Ring CSR and first Measurements

This thesis describes the setup of the first cryogenic reaction microscope, a new addition to the Cryogenic Storage Ring CSR. A technical description of the major components of the reaction microscope is presented. Selected results of the first experiments are discussed.
The electron-photo-detachment from CH^- was investigated as a proof-of-principle experiment of photo-electron spectroscopy. All visible features correspond to known transitions from the molecular ion to the neutral.
The Si^- + Ar collision is used as an example of a negative ion - neutral interaction. The process for electron loss with simultaneous target ionization is identified as a correlated interaction of target and projectile electrons. The cross section ratio, with and without simultaneous target ionization, was found to be an order of magnitude higher than expected.
For positive ion beam, electron transfer from a He, Ne or Ar neutral gas target to a Ar^+ projectile was investigated. Transitions into ground and excited projectile states could be identified for all targets. In addition, transfer target excitation for Argon target and electron transfer into metastable Ar^+ states from Helium and Neon targets is seen. The projectile scattering angle is extracted by the momentum transfer on the recoil ion.

Contents

1 Introduction

The interaction of large numbers of particles explains many macroscopic properties of matter, e.g. the behavior of gases under pressure or the reflection of X-rays in crystals. And the extension of the particle model of classical physics in the early 20th century led to the development of quantum mechanics [1]. Even today, the interaction of small pieces of matter, like atoms, ions, molecules or clusters with each other, or with photons or electrons, is of great interest (e.g. [2, 3, 4]) and spans many fields from fundamental particle and laser physics to (astro-)chemistry. It is therefore no surprise, that a wide range of experimental techniques, like ion traps or accelerators, were developed to investigate the interaction of particles. In the context of this thesis the experimental capabilities offered by storage rings and reaction microscopes are of particular interest.

A storage ring allows to investigate rare or hard to produce ions, e.g. ions in high charge states or exotic ions which need to be bred online [5]. The Cryogenic Storage Ring CSR provides a specialized environment for the examination of cold (molecular) ions, offering long storage times for ions in a wide range of masses. The cooled inner walls suppress radiative (blackbody) excitation of the stored ions [6]. This allows for experiments on, for example, dissociative recombination with rotationally cold molecules [7], or ion - neutral merged-beam experiments to determine reaction rates in interstellar clouds [8]. Recently, the long-standing mystery of the auto-fragmentation mechanism of C_2^- could be solved [9].

If a projectile beam (ion or neutral) interacts with a photon or a neutral target, fragmentation (for molecules) or ionization of either the target or the projectile can happen. A reaction microscope (ReMi) can retrieve the full 4π momentum image of a fragmentation or ionization event by coincident detection of the emitted electrons and recoil ions. They are used for many years either as a stand-alone setup [10] or as a part of a larger facility e.g. at the GSI in Darmstadt [11] or the free-electron laser FLASH [12]. And since the early planning stages of the Cryogenic Storage Ring, it was envisaged to also add a reaction microscope [13].

As a part of this thesis, this first cryogenic reaction microscope was set up. It is directly included in the cryogenic environment of the experimental vacuum of the CSR. The construction of the cryogenic reaction microscope CSR-ReMi presented many technical challenges, because of the ultra-high vacuum condition in the ring and the cryogenic environment. Special care was taken to not cut the ion beam passing through the reaction microscope. Also, the compatibility of the electric and especially the magnetic fields used by the reaction microscope with the electrostatic

Cryogenic Storage Ring needed to be ensured.

In Chapter 2, the Cryogenic Storage Ring CSR is introduced shortly, followed by a detailed technical description of the reaction microscope linear section in the CSR. To explain the working principle of the aptly named CSR-ReMi, the core components – the spectrometer to generate the extraction field, the position- and time-sensitive detectors and the magnetic coil system – are discussed individually. It is also explained how the momentum of the collected particles is retrieved. The supersonic gas jet to produce a neutral target for collision experiments and the laser system used for the photo-detachment experiment are also both outlined. Since the ion beam diameter is fairly broad ($\approx 2\,\mathrm{cm}$), a position correction will be explained to used to reduce the effective source volume for experiments with small scattering angle. A set of simple SIMION simulations was performed to ensure there are no strong distortions in the detector image and that the position correction can be used.

During this thesis, three different experiments were performed, each one focuses on a different kind of interaction which can be studied with the CSR-ReMi: the photo-detachment from a negative molecular ion, the interaction of negative ions with a neutral target leading to electron loss and target ionization and the interaction of positive ions with a neutral target leading to electron transfer from the target to the projectile.

Chapter 3 discussed electron-photo-detachment from CH^-. It was intended as a proof-of-concept experiment for the examination of the electronic structure of negative molecules in the cold environment of the CSR and to test the laser in-coupling and electron imaging system. The triple differential photo-electron momentum was determined, and all visible features were attributed to a known transition from the molecular ion to the neutral.

In chapter 4, the electron loss of a Si^- beam scattering with an Ar target was investigated. For electron loss, the electron emission angle follows roughly the expected emission angle for free electron scattering. Additionally, electron loss with simultaneous target ionization can be selected by demanding coincidence of electron, recoil ion and projectile hits. The process leading to simultaneous target ionization was identified as a correlated interaction between the projectile and target electrons. Surprisingly, the ratio of electron loss to electron loss with simultaneous target ionization was almost an order of magnitude above the expected value.

Chapter 5 studies electron transfer from helium, neon or argon targets to an Ar^+ projectile. The target ground state to projectile ground state and target ground state to excited projectile states transitions were identified. For $Ar^+ + Ar$, also target transfer excitation was seen. Capture into metastable Ar^+ states was identified by determining the population change over storage time.And the scattering angle of the projectile was determined by the momentum transfer to the recoil ion.

Finally, chapter 6 gives a short summary of the results and an outlook on future experiments and machine upgrades.

2 Experimental Setup

This section will give a short overview of the cryogenic storage ring CSR, the CSR-ReMi linear section and the working principle of a reaction microscope. The spectrometer, detectors and magnetic coil system of the CSR-ReMi will be discussed. The setup of the supersonic gas jet and the used laser system will be presented. The position correction method to reduce the effective source volume for small scattering angle will be explained, along with some SIMION simulations and an approximate method to determine the ion storage time. Finally, the vacuum quality in the CSR-ReMi central chamber will be estimated.

2.1 The Cryogenic Storage Ring (CSR)

Ion storage rings are useful tools to investigate e.g. ion-neutral interaction [2], electron-ion merged beams [14] and dissociative recombination [15]. Many studies where carried out in magnetic storage rings with high beam energy (MeV) [5]. For electrostatic storage rings, the accessible beam energies are usually limited to the keV range. But, since the ions are stored according to their kinetic energy-over-charge ratio E_{kin}/q, the storage is mass independent [16], allowing the storage of very large molecules [17].

The electrostatic Cryogenic Storage Ring (CSR) is located at the Max Planck Institute for Nuclear Physics in Heidelberg, Germany, a detailed description can be found in [6]. The newly installed reaction microscope in the CSR is the focus of this thesis.

Fig. 2.1 shows a schematic overview of the CSR (figure adapted from [2]). The ion beam orbit has $\approx 35\,\mathrm{m}$ circumference and is located inside two nested vacuum environments (the isolation vacuum and the experimental vacuum). Fig. 2.3 shows an overview of the linear section of the CSR reaction microscope (CSR-ReMi) with the nested vacuum chambers. The CSR-ReMi was installed in one of the linear sections. The CSR-ReMi linear section will be discussed in section 2.2.

The inner vacuum chambers of the CSR can be cooled to $< 5\,\mathrm{K}$ with a closed-cycle liquid helium cooling system, but the CSR can also be operated at room temperature for comparison measurements. In cryogenic operation, all chamber walls act as cryo pumps reducing the residual gas density to the order of $1000\,\mathrm{particles/cm^3}$. An additional effect of the cooled chamber walls is the reduction of black-body radiation in the CSR to an effective radiation field of $\approx 15 - 20\,\mathrm{K}$. This allows the study of the de-excitation of internal states in atomic and molecular ions (see e.g. [18, 19]).

The ion beam is produced in one of the two high-voltage platforms shown on the right of Fig. 2.1. The ions are accelerated towards the CSR by the voltage gradient between the platform and the CSR (the ion path is marked in red on the schema). The larger ion source platform 1 can produce beams up to ±300 keV per elementary charge and ion source platform 2 can produce beams with up ±60 keV per elementary charge (see [2]). The high-voltage platforms offer multiple source options (MISS, Penning source, ECR source, duoplasmatron source, Laser vaporisation source) and can produce positive and negative ion beams. As an electrostatic storage ring, the CSR stores ions according to the kinetic energy-over-charge ratio E_{kin}/q. The ion beam is mass selected by dipole magnets, in the injection beam line, deflecting the beam depending on its mass-over-charge ratio m/q. The ion beam is injected through one of the beam deflectors in the corner sections. Each corner contains four electrostatic deflectors with $6°, 39°, 39°$ and $6°$ deflection angle to keep the ion beam on a closed orbit.

There are multiple experiments at the CSR. The electron cooler can be used for electron capture experiments (e.g. [7]) and measurements on photo-detachment and

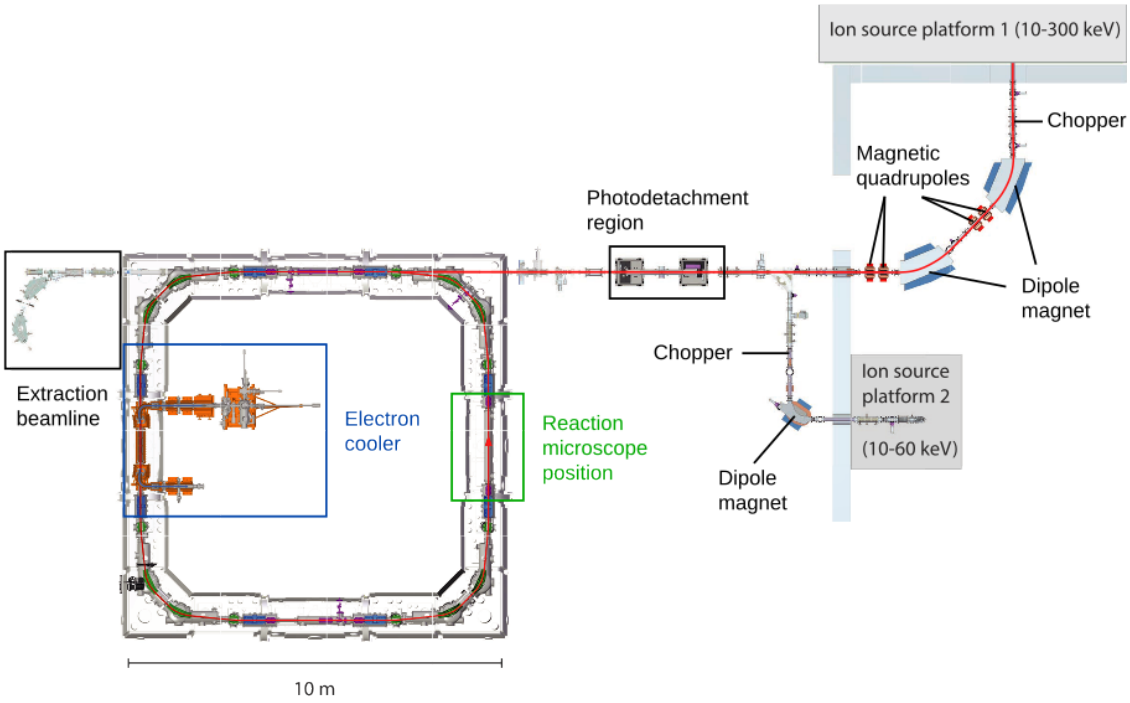

Figure 2.1: CSR overview, modified from [2]. The storage ring shown is on the left with the electron cooler (ECOOL) and the reaction microscope (green box) linear section marked. On the right are the high-voltage platforms and the injection beam line. The red line marks the ion beam path from the high voltage platform 1 to the CSR and the ion orbit inside the ring.

photo-dissociation [18]. In the linear section between the injection and extraction beam line, the ion beam can be merged with a neutral beam to study astrochemical reactions [2]. The remaining linear section is used for beam diagnosis and monitoring.

2.2 The CSR-ReMi Linear Section

Fig. 2.2 shows an overview of the CSR with the CSR-ReMi linear section in the front. The central chamber of the CSR-ReMi and the neutral detector are shown in the inserts. The central chamber is surrounded by the five copper coils used to generate the homogeneous magnetic field. The neutral detector is mounted downstream of the CSR-ReMi, in the corner section, after the 6° deflector. The ion beam is bent by the 6° deflector to stay on a closed orbit and thereby separated from the neutralized projectiles which hit the neutral detector.

The whole CSR is baked out to 450-500 K (depending on section) to reduce contaminants before a beam time and cooled down to ≈ 5 K during a beam time [6]. All materials need to be able to withstand the full temperature range. Parts with a rigid connection need to have matching thermal expansion coefficients to avoid stress (and worse-case cracks or ruptures) by thermal expansion and contraction. For the same reason, some flexible elements, like bellows in the vacuum chambers, are needed between parts connected to different mounting points. For all vacuum flanges in the 5 K section, Helicoflex seal from Technetics were used [20], because they can withstand the thermal transient.

Fig. 2.3 gives a more detailed overview of the CSR-ReMi linear section. The neutral detector ④ is also displayed forward of the linear section. The ion beam is indicated by a magenta line. In the spectrometer center, the ion beam is crossed with a laser (transparent yellow, see section 2.6) or a target from a supersonic gas jet (green line, see section 2.5). The ion (red) and electron (blue) paths are also indicated. The spectrometer ① is located inside the central ReMi chamber in the experimental vacuum of the CSR (see section 2.3.1). The experimental vacuum in the CSR can reach pressures of 10^{-13} mbar [6]. Since even small out-gassing rates would be detrimental to the vacuum, the parts in the experimental vacuum are almost exclusively constructed from BN2 stainless steel, high purity copper, titanium grade 2 and sintered ceramic. All parts are cleaned from surface contaminants, like machine oil, and metal parts are high temperature vacuum annealed to reduce hydrogen out-gassing [21]. The ion ② and electron detector ③ are located on the ends of the spectrometer. Since all electrodes and detectors are fully wired to the airside, both detectors can be operated as ion or electron detector without breaking the vacuum. The central chamber is connected to the CSR by two 62 cm long beamtube chambers. These chambers are NEG coated [22] to provide additional pumping before and during cool down. The holding struts of the central chamber

are constructed from thin (0.5 mm thickness) titanium sheet metal to reduce thermal conduction and bend in a zigzag fashion for structural rigidity. Additionally, the struts are thermally anchored to 40 K, since the cooling power at 40 K is higher than at 5 K. The central chamber and the beamtubes are surrounded by two layers of thermal shields. The inner shield is cooled to ≈ 40 K (⑤ dark blue) and the outer shield to ≈ 80 K (⑤ light blue). Both thermal shields are constructed out of 2 mm thick 99.5 % aluminum sheets, which are thermally connected to the 40 K and 80 K line of the Helium cooling lines, respectively. Additionally, the 80 K thermal shield is wrapped in 25 to 30 layers of multilayer insulation [23] to reduce thermal radiation input from room temperature. The five quadratic coils ⑥ to generate the homogeneous magnetic field and the eight compensation coils ⑦ are located outside the cryogenic section, more on the magnetic coils can be found in section 2.3.3. At the two adapter chambers, at the beginning and end of the ReMi linear section, the cold units ⑧ are mounted. The cold units are copper blocks connected

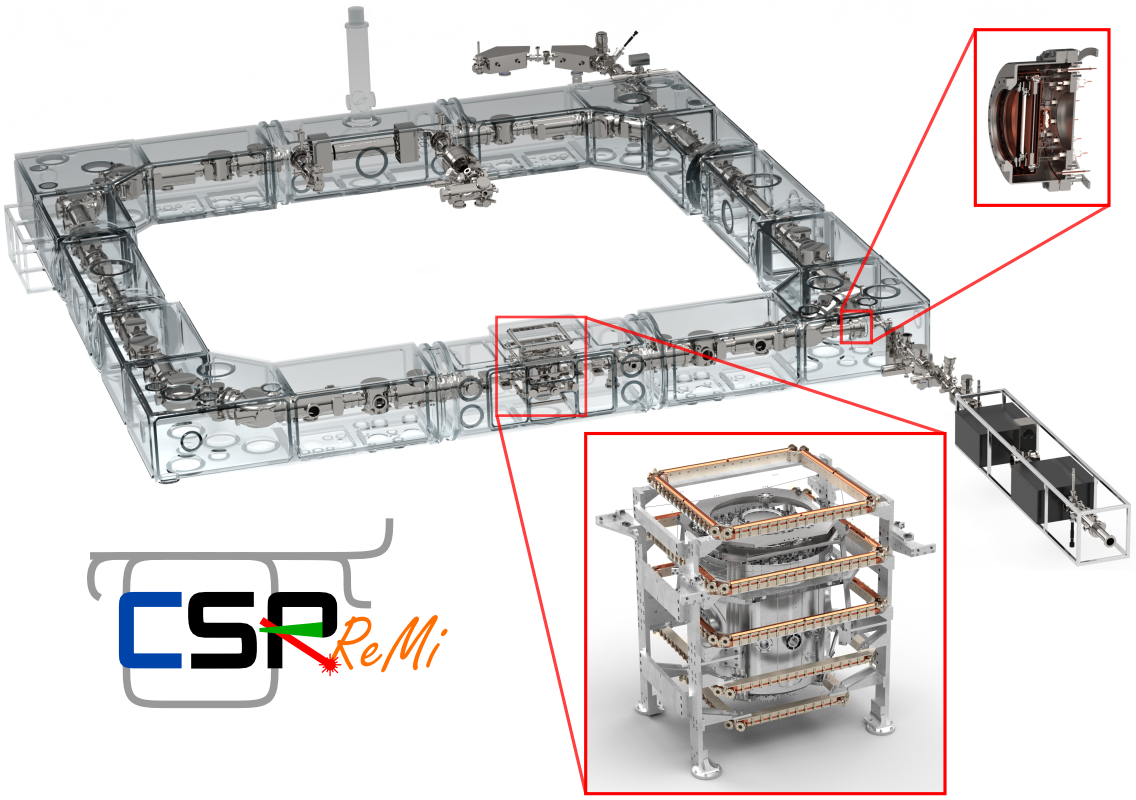

Figure 2.2: CSR overview with the reaction and neutral detector in the inserts. The injection beam line is on the right side, the linear section of the CSR-ReMi on the front. The lower insert shows the central chamber of the CSR-ReMi with part of the support frame. The top right insert displays the neutral detector. Logo adapted from a design by Viviane Schmidt.

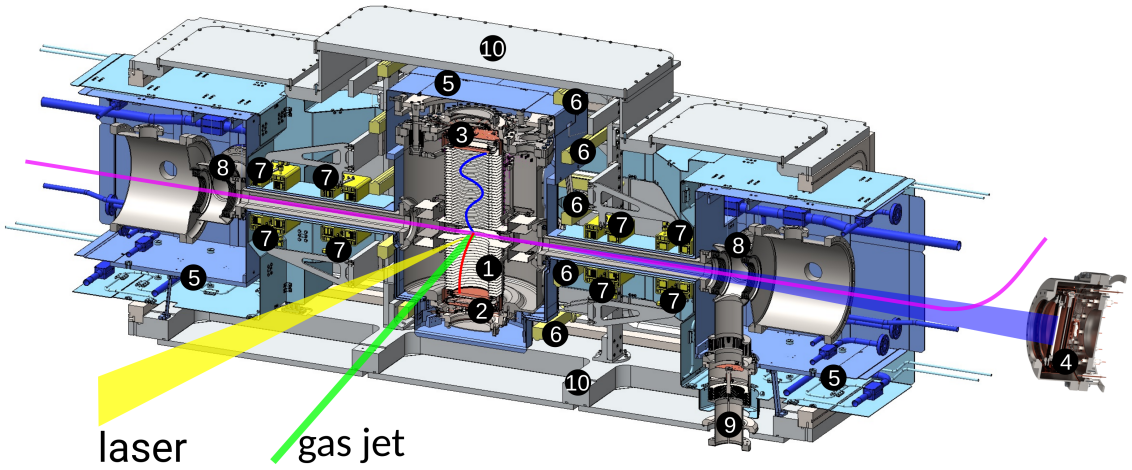

Figure 2.3: Overview of the CSR-ReMi linear section with the neutral detector in forward direction (distance not to scale). ① the spectrometer inside the central ReMi chamber (experimental vacuum), ② the ion detector, ③ the electron detector, ④ the neutral detector (in the corner section behind the 6° deflector), ⑤ thermal shields (light blue 80 K, dark blue 40 K, dark blue tubes represent Helium cooling lines), ⑥ coils for homogeneous magnetic field (at 300 K), ⑦ magnetic-field compensation coils (at 300 K), ⑧ adapter chambers with cold units, ⑨ pump port to 300 K, ⑩ isolation vacuum chamber. The gas jet (green line) and laser in-coupling (transparent yellow) are also marked, the ion beam is represented in magenta.

to the 2 K Helium cooling line [6]. To cool the inner chambers, they are connected to the cold units by annealed 99.997 % copper bands of 2 mm thickness. The adapter chambers connect the beamtubes of the ReMi linear section with the neighboring chamber, which contain the quadrupole optics for the ion beam and have a wider diameter. Additionally, the adapter chambers contain bellows to compensate for thermal expansion and contraction during bake out and cool down. The pump port goes downward from the forward adapter chamber and exits the cryogenic environment, to connect the experimental vacuum in the ReMi section with a turbomolecular pump [24] and a ion getter pump [25]. The pump port contains a movable copper aperture anchored to 40 K, which can be closed during cryogenic operation to reduce the cross-section area of the pump port (the pump port design is analogous to existing pump ports in the CSR [6]). The isolation vacuum chamber ⑩ surrounds the inner parts of the ReMi linear section and provide a 10^{-6} mbar vacuum for thermal isolation and to reduce the leak rate into the experimental vacuum.

Tab. 2.1 provides an overview of the basic parameters of the CSR-ReMi. The maximal electric and magnetic fields are limited by the break-down voltages of the

Table 2.1: Overview on basic parameters of the CSR-ReMi. The distances for the ion and electron detector are given from the interaction region in the spectrometer to the first grid. The neutral distance is given from the interaction region to the MCP front of the neutral detector.

property	ion	electron	neutral
distance from interaction centre	21.645 cm	30.645 cm	439.06 cm
active MCP diameter	120 mm		120 mm
typical electric field	1-2 V/cm		-
max. electric field	40 V/cm		-
typical magnetic field	5 Gauss		-
max. magnetic field	31 Gauss		-

plugs and wires installed in the ReMi section.

2.3 Reaction Microscope

A reaction microscope (ReMi) [26, 27] is a combined electron and ion detector to collect all charged particles produced in a fragmentation or ionization event. A ReMi is capable of retrieving all three momentum components of the particles detected in coincidence and can therefore generate a kinematically complete picture of the investigated event.

Fig. 2.4 shows a schematic overview of a reaction microscope. The ions and electrons producing event is marked, as a magenta seven-pointed star, in the interaction region of the ReMi spectrometer. The spectrometer is producing a electrostatic extraction field (transparent red arrow) to guide the electrons (blue line) and ions (red line) to two position- and time-sensitive detectors (here, MCP detectors with delay line readout, the experimental details of the detectors are discussed in section 2.3.2). In the simplest case, the electrostatic extraction field has a linear gradient over the whole spectrometer, but it is also possible to include e.g. a drift region for time focusing (see [28] ch. 2.2.1) or an electrostatic lens [29]. A homogeneous magnetic field (transparent blue arrows) is superimposed over the spectrometer to force the electrons on a cyclotron path. This allows for coincident detection of electrons and ions with the same extraction field. Most ReMi's use a pair of Helmholz coils to generate the magnetic field (see e.g. the TrapReMi [10] and the ReMi endstation at FLASH2 [12]), for the CSR-ReMi this was not possible, because of spatial constrains, instead the CSR-ReMi uses five square coils as discussed in section 2.3.3.

A ReMi can be oriented in two principal ways, with longitudinal (e.g. [10]) or transversal (e.g. [12]) extraction of the ions and electrons relative to the projectile beam (ion beam or laser pulse). For experiments with a stored ion beam, the longitudinal orientation offers the advantage that the electric and magnetic field

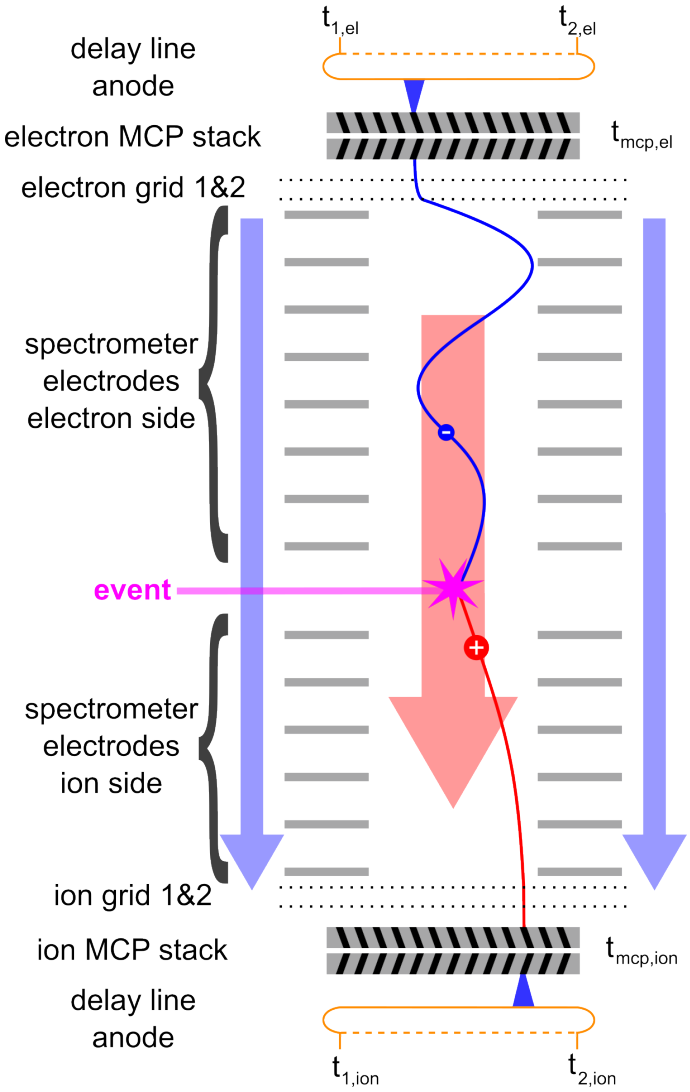

Figure 2.4: Schematic overview of a reaction microscope. The grey bars represent the spectrometer electrodes producing the electrostatic extraction field, symbolized by the transparent red arrow. The homogeneous magnetic field is represented by the transparent blue arrows. The magenta seven-pointed star marks the location of the event producing electrons and ions. The ion trajectory is marked in red and the electron path in blue. The gray and black plates symbolize the MCP stack, behind it is the delay-line anode in orange.

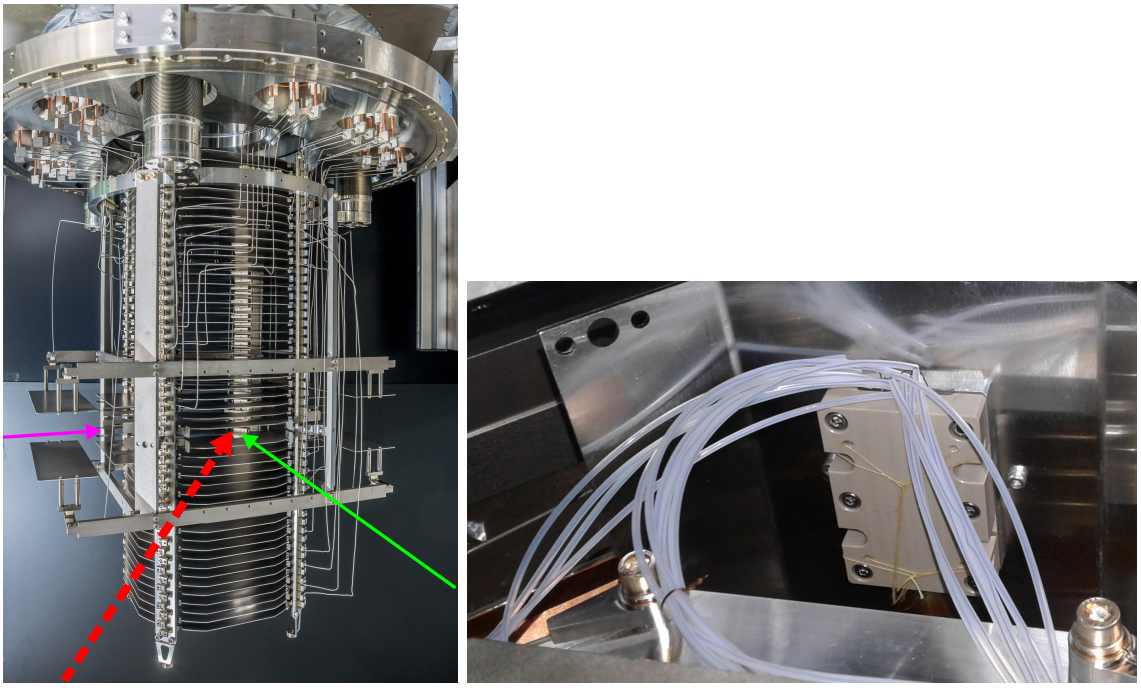

Figure 2.5: Left: The spectrometer before integration. The magenta arrow marks the ion beam, the red dashed arrow the laser and the green arrow the gas jet direction. The rectangular plates to the left and right are capacitor plates to compensate the influence of the spectrometer field on the ion beam. Picture by Ralf Lackner.
Right: One of the thermal anchors for the spectrometer cables inside the isolation vacuum, mounted to the 40 K thermal shield. The 0.25 mm manganin wire are in 1 mm Teflon tubing to reduce risk of damage to the Kapton isolation.

are aligned with the ion beam direction of travel and do therefore not change the ion beam trajectory. The disadvantage is that for longitudinal orientation a hole in the detectors is required, to allow the ion beam to pass through. In contrast, for transversal orientation, as in the CSR ReMi, the electric and magnetic fields will change the ion beam trajectory. It is then necessary to compensate the effect of these fields on the ion beam (see section 2.3.1 and 2.3.3 will discuss how this is realized).

2.3.1 Spectrometer

The spectrometer (see Fig. 2.5 left) of the CSR-ReMi is mounted in the central chamber of the ReMi linear section (see Fig. 2.3). It has an over all length of 51 cm and consists of 51 electrodes. The electron spectrometer arm has 30 electrodes and

the ion detector spectrometer arm has 21 electrodes. The spectrometer is mounted such that the thermal contraction of electrodes and detectors is symmetric to the interaction region. Each electrode was made of 1 mm titanium grade 2 sheet metal and a knife edge was milled onto the inner edge. The electrodes were high temperature vacuum annealed to reduce hydrogen out-gassing from the metal [21]. The electrode-to-electrode distance is 9 mm. The distance between the electrodes next to the interaction region is 19 mm, to allow for the laser and gas jet to pass through the spectrometer from the side (see Fig. 2.5 left gap in middle of spectrometer). The four electrodes around the interaction region are constructed out of two separated pieces to allow the ion-beam passage (window for ion beam into spectrometer has the dimensions 100 mm × 60 mm, same as the beam tube before and after the spectrometer to not restrict the beam). Each electrode is individually contacted by a bare 1 mm titanium wire to one of nine 7-fold high-voltage feedthroughs into the isolation vacuum. To compensate the influence of the electrostatic spectrometer field on the ion beam, a pair of capacitor plates is located before and after the spectrometer. In the isolation vacuum, each of the electrode pins is contacted to one of four 18-pin push-pull connectors[1] by a 0.25 mm Manganin wire with Kapton insulation [30]. Manganin wire of 0.25 mm diameter was selected to minimize thermal conduction from the 300 K side of the wire. Additionally, all wires are thermally anchored to the 40 K thermal shield by one of four custom-build thermal anchors pressing the wires on a sapphire plate (see Fig. 2.5 right). On the air side, the electrode voltages can be defined by a voltage divider or individual power supplies. Here, an iseg NHS 6005x power supply [31] was used with a voltage divider to supply the voltages to the spectrometer.

To gain an estimation of the electric field inhomogeneity, the electrode to electrode gap was measured on three positions (left corner, middle, right corner) for all four electrode sides using a set of final size pieces. The results are summarized in Fig. 2.6. The mean of 9.04 mm is within expected fabrication tolerances. Since each electrode has a thickness of 1 mm and the design gap between two electrodes is 9 mm, the variance of 0.24 corresponds to an expected electric field deviation of 2.4 %. The quality of the voltage divider is negligible compared to the distance variation.

The spectrometer is mounted on three manipulators (bellows in the top of Fig. 2.5 left). This allows to adjust the position, to align the spectrometer with the CSR ion beam according to the laser position grid established by sigma3D [32].

2.3.2 Detectors

The CSR-ReMi has three detectors: one (recoil) ion detector, one electron detector and one neutral fragments detector. In the current setup, the ion detector

[1] Fischer S 105 A038-130+ on the vacuum side

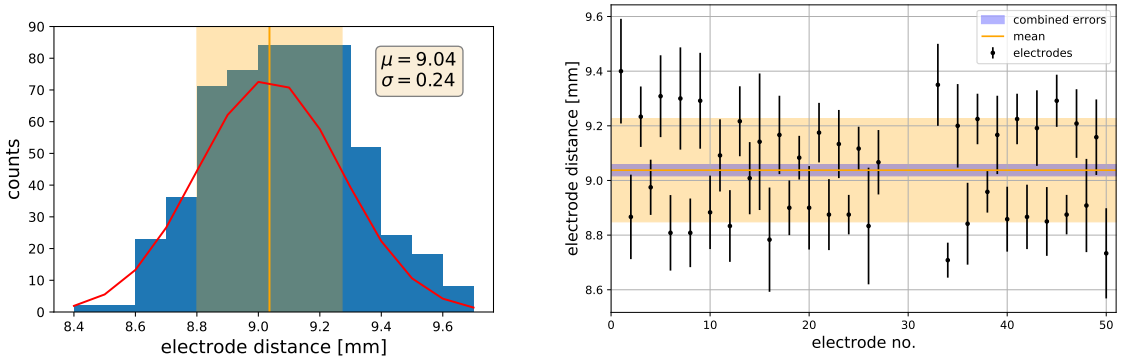

Figure 2.6: Left: Histogram of the electrode-to-electrode distance measurements, red line is a Gauss fit, orange line is the mean and orange shaded area corresponds to 1σ interval.
Right: Electrode distance for each electrode. Black points with error bars are determined by averaging individual distance measurements for one electrode pair.

is located at the top and the electron detector at the bottom end of the spectrometer. The neutral detector is mounted 4390.6 mm forward from the interaction region/spectrometer center behind the 6° deflector (see Fig. 2.2).

Fig. 2.7 shows an overview of the detector layout. The ion and electron detector use two grids (① and ②) of A4 stainless steel (type 1.4404) with a mesh size of 140 μm and a wire diameter of 20 µm (the transmission of one grid is $\approx 73.47\,\%$, therefore the total transmission through both grids is $\approx 53.98\,\%$) to provide a defined closing potential for the spectrometer (minimizes field penetration from the high voltage MCP fronts) and to accelerate slow ions or electrons sufficiently to produce a detector response. For the neutral detector no grids were mounted to increase overall detector efficiency, since the ion beam minimum energy of about 10 keV provides more than enough kinetic energy to trigger a detector response and for neutral particles no guiding fields or closing potentials are needed. The detector uses a chevron stack of two 120 mm Photonis microchannel plates (MCPs ③) [33] with an open area ratio (OAR) of ≥ 0.65 to amplify a hit (see A.2 for more details). The recharge pulse of the MCP can be used as a precise timing signal of the hit. Behind the MCP stack is the ring anode ④. And after that the electron cloud is collected by a so called delay line anode [34]. The CSR-ReMi uses a quadratic delay-line anode, which means there are two orthogonal layers of wire ⑤ helically wound over grooved ceramics fitted to the anode base plate ⑥. For the delay-line wire, a 0.2 mm diameter copper zirconium wire (0.2% zirconium) is used. Directly next to the signal wire, a reference wire for background subtraction is wound (an overview of the detector bias voltage can be seen in Tab. A.1). Distance between two parallel rounds of the wire is 0.5 mm. The electron cloud is collected by the

signal wire and produces a signal running into both directions from the hit position. If the arrival times t_1 and t_2 of the signal on both ends of the wire are measured, the hit position along the wire can be inferred by the time difference $t_1 - t_2$ (since the speed of light in the wire is constant).

The detectors are mounted with four mounting screws ⑪ to titanium holding brackets on the spectrometer (for the electron and ion detector, see Fig. 2.5 at the bottom end of the spectrometer) or to support struts directly to the chamber wall (for the neutral detector).

Since the detector is inside the cryogenic environment of the CSR, the MCP resistance will rise exponentially with falling temperature [35]. The recharge time increases with increasing MCP resistance (as for a RC circuit), at 5 K the detector would be unusable with a resistance in the TΩ range. To get an acceptable detector response, the MCPs are heated to around 40 K with two redundant 0.1 mm diameter Constantan heating wires mounted to a copper bride on the backside of the detector.The copper bride is electrically isolated from the MCPs (which are at up to 3 kV) with a sapphire clamping system ⑧. This heating system was inspired

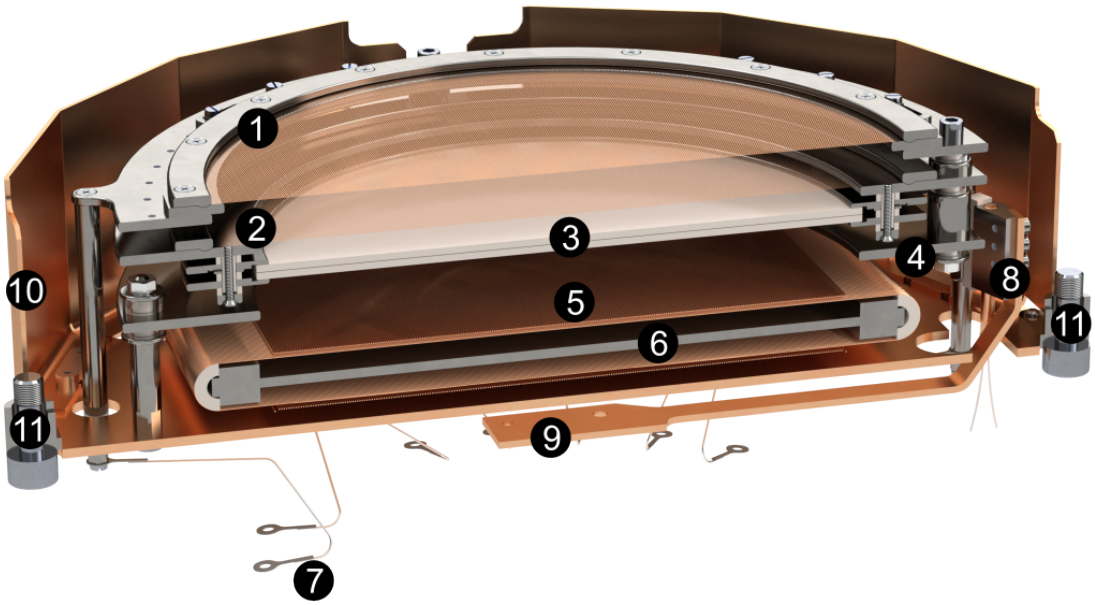

Figure 2.7: Detector overview. ① grid no 1 (not mounted for neutral detector), ② grid no 2 (not mounted for neutral detector), ③ MCP stack, ④ ring anode, ⑤ delay line wires, ⑥ delay line anode base plate, ⑦ connection wire to vacuum feedthrough, ⑧ sapphire clamping for MCP heater, ⑨ mounting point for MCP heater, ⑩ copper shield around detector, ⑪ mounting screws.

by the COMPACT detector [36] heater, already in use in the CSR. The detector is surrounded by a copper shield ⑩ to reduce thermal radiation from the heated MCPs to the surrounding.

To connect the signals and voltages, inside the experimental vacuum, to individual high voltage feedthroughs to the isolation vacuum, 0.5 mm A4 stainless steel wire (⑦ was used. In the isolation vacuum the detector cables are connected with 0.25 mm Kapton isolated Manganin wire [30] to SHV feedthroughs to air. The Manganin wire is thermally anchored to the 40 K shield, with the same thermal anchor design already mentioned in section 2.3.1. On the air side the SHV feedthroughs are connected with a breakout box. This box subtracts the reference and signal contacts, and contains a voltage divider to provide the correct voltages to all parts, see section A.1 for a circuit drawing. The detector voltages were supplied to the breakout box by ISEG NHQ 204M power supplies [37].

All detectors were tested at 20 K with a ^{241}Am source and a hole mask in a stand-alone cryogenic test chamber [38], before being installed in the CSR.

Detector Efficiency The ion and electron detector have each two grids with 53.98 % total transmission and a front MCP with an open are ratio of ≥ 0.65. The expected overall efficiency is 35.09 %.
Since the neutral detector has no mounted grids, the open area ratio is the main limiting factor of the detector efficiency and therefore, the efficiency of the neutral detector is expected to be around 65%.

Time-of-Flight Determination with the Neutral Detector

The ion beam, gas jet and even the used laser, in this thesis, are continuous and can not be used as triggers for the time-of-flight like for pulsed sources. Fig. 2.8 a) shows a schematic example of the neutral, electron and ion hit times relative to the actual event time t_0. Since the neutralized particle flies ballistically to the neutral detector, the time-of-flight of the charged particles $\mathrm{TOF}_{\mathrm{el/ion}}$ can be indirectly determined by

$$\mathrm{TOF}_{\mathrm{el/ion}} = t_{\mathrm{el/ion}} - t_{\mathrm{neut}} + \mathrm{TOF}_{\mathrm{neut}} \tag{2.1}$$

with $t_{\mathrm{el/ion}}$ the electron or ion-hit time, t_{neut} the neutral-hit time and $\mathrm{TOF}_{\mathrm{neut}}$ the time-of-flight of the neutralized projectile.

The momentum spread of the ion beam is small ($\Delta p_{\mathrm{beam}}/p_{\mathrm{beam}}$ is about 10^{-4}) and the momentum transfer to the target (or detached electron) is usually small compared to the beam energy. The neutralized projectile flight time is almost constant and can easily be calculated with

$$\mathrm{TOF}_{\mathrm{neut}} = \frac{s_{\mathrm{neut}}}{v_{\mathrm{beam}}} = \frac{s_{\mathrm{neut}}}{\sqrt{\frac{2E_{\mathrm{beam}}}{m_{\mathrm{beam}}}}} \tag{2.2}$$

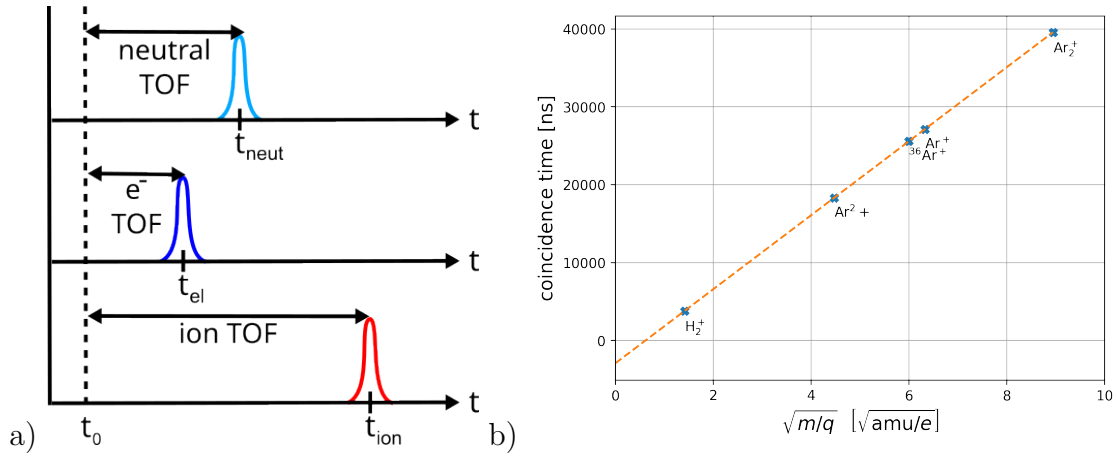

Figure 2.8: a) Scheme of time-of-flights and hit times relative to the actual event time t_0.
b) square root of the mass-over-charge ratio $\sqrt{m/q}$ vs coincidence time $t_{\text{ion}} - t_{\text{neut}}$ for Si^- (@ 300 keV) + Ar (interaction discussed chapter 4).

with $s_{\text{neut}} = 4390.6\,\text{mm}$ the flight distance of the neutralized projectile and the beam velocity $v_{\text{beam}} = \sqrt{(2E_{\text{beam}})/(m_{\text{beam}})}$ calculated from the beam energy E_{beam} and the mass of the projectile m_{beam}. Fig. 2.8 b) shows the square root of the mass-over-charge ratio $\sqrt{m/q}$ vs coincidence time $t_{\text{ion}} - t_{\text{neut}}$ for Si^- (@ 300 keV) + Ar (interaction discussed chapter 4) for different ions identified in the time-of-flight spectrum. The time offset for zero $\sqrt{m/q}$ is 2960 ns and differs 3.1 % from the calculated neutral time-of-flight of 3053 ns. In the experiment, the TOF spectrum origin position can be adjusted relative to the charged particles with zero momentum to get a better resolution in z/TOF direction. From the slope of the $\sqrt{m/q}$ plot, the voltage gradient experienced by the ion is 1.927 V/cm. This differs only 1.8 % from the expected voltage gradient of 1.961 V/cm.

Neutral Flight-Time Change from Energy Transfer Use Ar^+ (@ 30 keV) + Ar as an example system, since the change in flight time is larger for low beam velocities. The expected neutral flight time is then $\text{TOF}_{\text{neut}} = 11541\,\text{ns}$. For a energy transfer of $\Delta E = 15.8\,\text{eV}$ (Argon ionization energy [39]) the change in flight time is

$$\Delta t = \frac{s_{\text{neut}}}{v(E_{\text{beam}})} - \frac{s_{\text{neut}}}{v(E_{\text{beam}} + \Delta E)} = 3.04\,\text{ns}. \tag{2.3}$$

For 21 cm ion acceleration length in the spectrometer and 16 V ion acceleration voltage with singly charged ions, this time difference corresponds to a difference of 0.019 a.u. (a.u. denotes atomic units) in the p_z momentum.

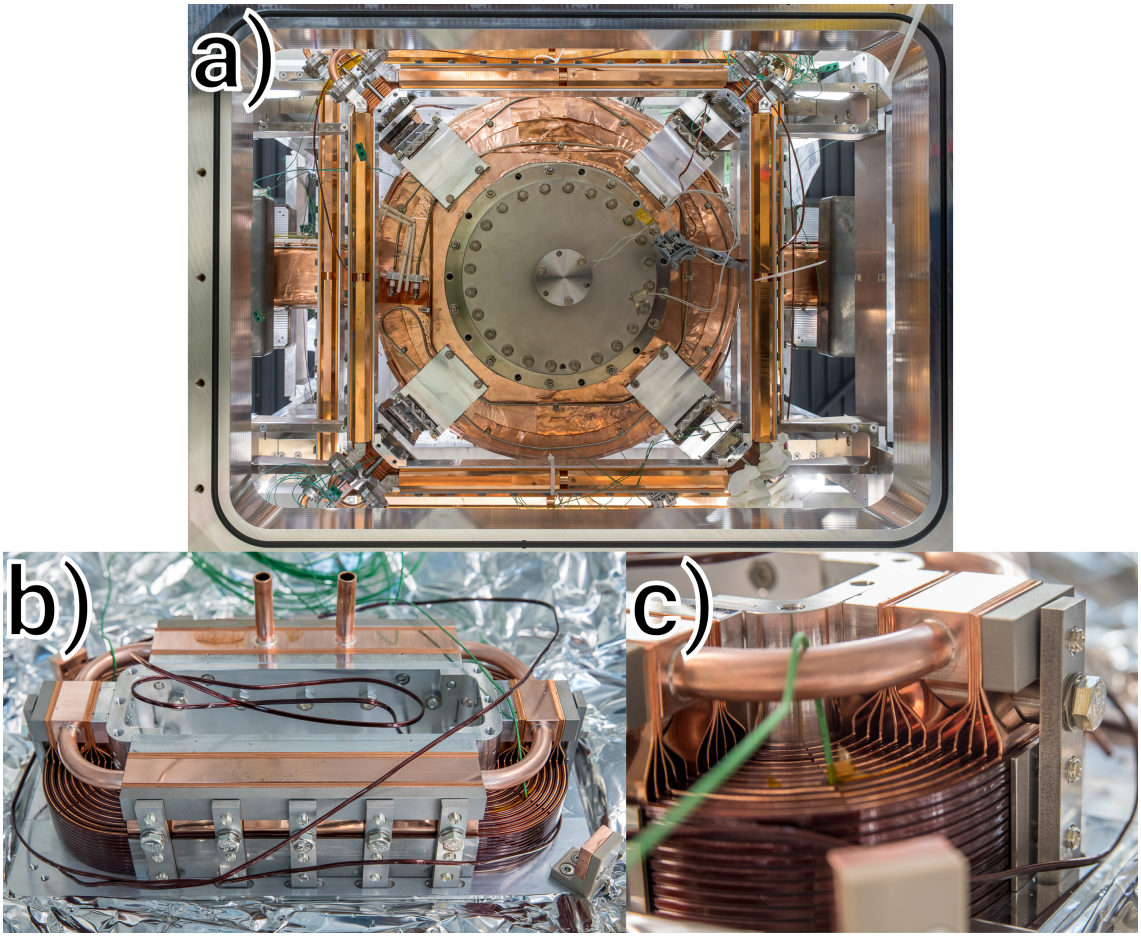

Figure 2.9: a) Lowest coil of the square coils for production of the homogeneous magnetic field viewed from below. b) Compensation coil. c) Detail of the water cooling of one of the compensation coils. Copper sheets are put between windings of the enamel copper wire and braced on the water cooling block.
Pictures by Ralf Lackner.

2.3.3 Magnetic Fields

Many ReMi's use a pair of Helmholtz coils (e.g. [12, 10]), but this is not possible for the CSR-ReMi. The spectrometer is 51 cm long and the needed Helmholtz coils would need to be so big, they would interfere with the operation of the CSR.

All coils in the CSR-ReMi are air-coils to avoid hysteresis, but the compensation coils have steel magnetic shielding to reduce edge-field bleeding into ReMi central section. The CSR-ReMi uses five quadratic coils positioned around the central chamber with the spectrometer. A set of five square coils will provide a field that is acceptable uniform near the center [40]. Merritt et al. [40] use coils of identical size

and vary the coil current to achieve a homogeneous field inside the coils. Because of the restricted space, the CSR-ReMi uses two large coils, two medium size coils and a small coil, similar to a Fanselau coil configuration (two pairs of larger and smaller coils) [41] with an additional small coil to extend the homogeneous magnetic field region over the whole spectrometer. Because of the deviations from ideal theoretical coil geometries the magnetic-field homogeneity was adjusted experimentally.
There are two quadratic coils with the inner diameters 690 mm × 690 mm, two coils with 630 mm × 630 mm and one coils with 470 mm × 470 mm inner diameter (see Fig. 2.9). The coils are constructed on a rectangular frame with 15 rounds on 5 layers made out of $4 \times 1\,\mathrm{mm}^2$ enameled copper wire. Every two rounds a piece of copper sheet metal is put between the wire wrappings to provide cooling to the wires (cf. Fig. 2.9). The copper sheet is clamped to a copper block, through which a water cooling tube runs.

Two pairs of small rectangular compensation coils are on the upstream and two pairs are on the downstream side of the central chamber to compensate the effect of the magnetic field on the ion beam. These eight compensation coils are rectangular with the inner diameter of 40.4 mm × 145 mm (cf. 2.9). The $2 \times 1\,\mathrm{mm}^2$ enameled copper wire is wound on the rectangular frame in 22 rounds on 11 layers. As for the coils for the homogeneous field, every two rounds a copper sheet is put between the windings and clamped to a water cooled copper block (see Fig. 2.9 c).
The current for the coils is supplied by 11 KEPCO BOP 20-20M (20 V, 20 A) and 2 KEPCO BOP 20-10M (20 V, 10 A) power supplies. All power supplies where tested to have current stability in the order of $\Delta I/I = 10^{-4}$.

The field maps for this magnetic coil configuration were simulated by Johannes Goullon with Opera3D. Manfred Grieser integrated these field maps into the G4beamline representation of the CSR. The inner pairs of compensation coils need to produce $-5.007\times$ the homogeneous field and the outer pair of compensation coils $3.636\times$ the homogeneous field to compensate the effect of the homogeneous field on the ion beam trajectory (see Fig. 2.10)

The overall magnetic field (in z direction) in the spectrometer was characterized with a commercial Hall probe[2] using a F. W. Bell SYPRIS Model 7010 Gauss/Teslameter, cf. Fig. 2.11. The deviation of the homogeneous magnetic field in z direction by the edge field of the compensation coils was determined to be below 1%. The edge field of the compensation coils is the main limiting factor of the homogeneity of the magnetic field, since the edge field of the compensation coils cause the hump between -400 and -200 mm and also a slight asymmetry between the magnetic field in ion beam and in gas jet direction.

[2]SYPRIS 6000 axial probe, SKU: HAD61-2508-05

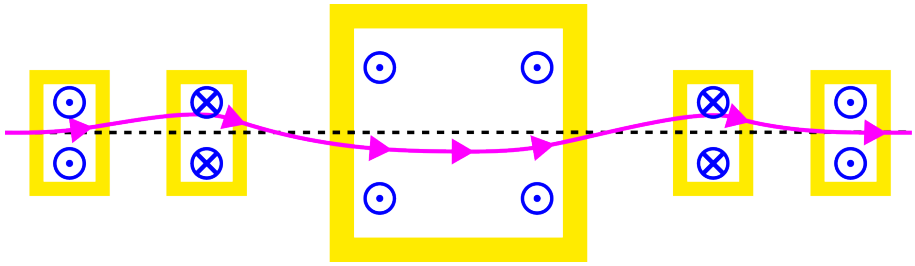

Figure 2.10: Schematic ion beam deflection by homogeneous magnetic field and the compensation field (top view, not to scale). The ion-beam is magenta, the coils are marked in yellow, the magnetic field direction is marked in blue. The ion beam trajectory in the interaction region is straight and the effect of the homogeneous magnetic field is compensated when the ion beam leaves the CSR-ReMi section.

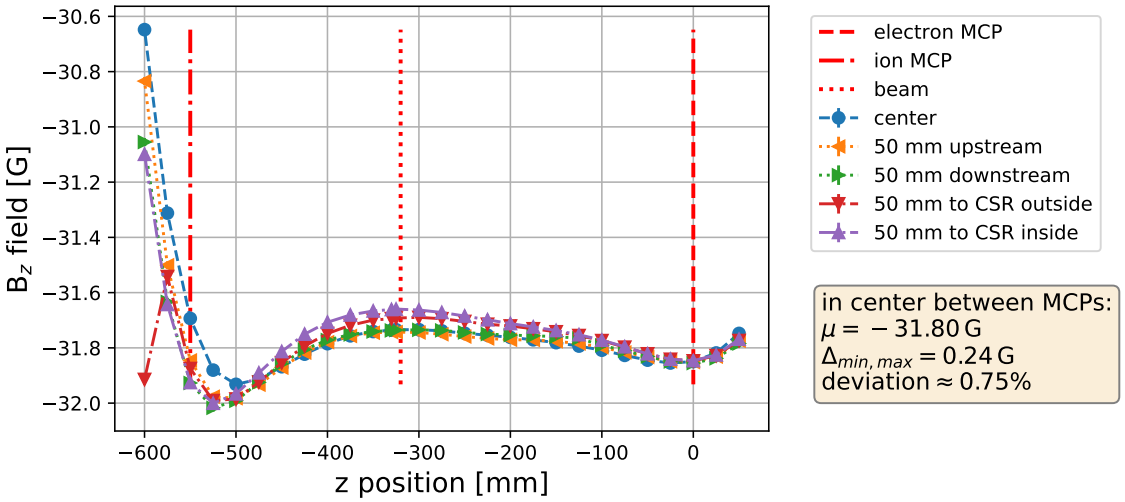

Figure 2.11: The magnetic field in the spectrometer with homogeneous and compensation field measured at five positions relative to the detector plane inside the spectrometer. The z position is relative to the electron detector MCP.

2.4 Data Acquisition and Analysis

Fig. 2.12 shows a block diagram overview of the data acquisition system. Starting from the detectors (the dashed box represents the vacuum environment inside the CSR), the detector signals are passed through feedthroughs to the airside and are out-coupled from high voltage by the breakout boxes. The breakout boxes also perform the analog background subtraction between the signal and reference delay line wires (see section A.1 for circuit diagram). The signals (MCP signal and x_1, x_2, y_1, y_2 delay line signals) of each detector are amplified by separated Ortec FTA820A [42] fast amplifiers. The MCP signals of the ion and the electron detector are passed through a constant-fraction discriminator (CFD) using the gate function to suppress the high count rate during injection. The data is digitized with a 16-channel RoentDek FADC8b/10-2 system. The RoentDek CoboldPC software [43] handles the data acquisition and coincidence detection and saves the events in list-mode-files. To avoid saturating the dynamical range of the ADC[3] individual signal where attenuated if necessary. This is mainly necessary for the neutral detector, but is checked occasionally, because the interference noise present in the CSR-ReMi is not constant and therefore the detector performance can change, see section 2.11.

For offline analysis the data can either be viewed with Cobold or extracted from the list-mode-files and investigated with external software. Additional data analysis was performed in Python. The analysis code is available 'as is' under `https://keeper.mpdl.mpg.de/d/44b876aa2e4f4325bec5/`. As a brief summary, the program retrieves full traces from the list-mode-file. The peak position is extracted from the traces to get the signal times (times saved as absolute timestamp starting from the beginning of the measurement). From the signal times, the hit position on the detectors is calculated with $c_{\mathrm{det}}(t_1 - t_2)$ with t_1, t_2 the signal times from both delay line ends and c_{det} a detector dependent conversion factor to length. Also, reflections and noise are suppressed by allowing only signals within a small window around $t_1 + t_2$, since the delay line wire length is constant and therefore the time sum for all real hits should be identical. The coincidence times between the neutral MCP time and the ion/electron MCP time is used to get the time-of-flight (see section 2.3.2). From the detector positions and time-of-flight the momentum components of an electron or ion can be calculated as described in section 2.4.1, then further analysis depending on the experiment can follow.

2.4.1 Momentum Reconstruction

This section is based on [28] ch. 2.2 and 2.5.
A charged particle is extracted from a (ideally point-like) source volume with a homogeneous electric field. The momentum components are calculated from the hit

[3] Analog-to-Digital Converter

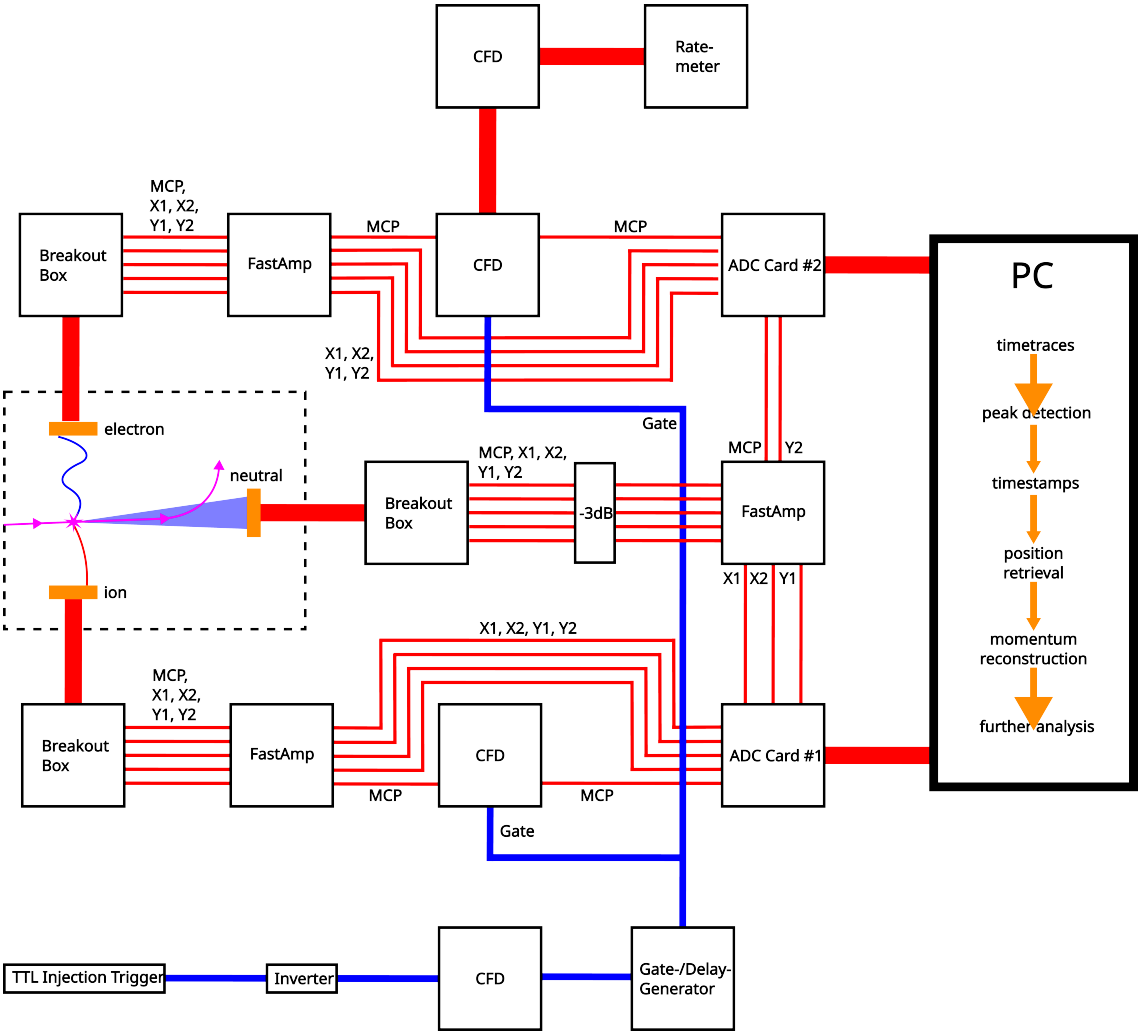

Figure 2.12: DAQ schema. The area in the dashed box represents the vacuum environment containing the CSR-ReMi with the electon, ion and neutral detector. The magenta line marks the ion beam. The MCP signal is passed through a CFD with a gate/veto function to suppress the injection flash. The delay line signals are not passed through the CFD and are digitized directly (with MCP as trigger).

position x and y on the detector and the time-of-flight.

Momentum along Spectrometer Axis/z axis

The spectrometer axis is aligned with the z axis of the ReMi reference frame. The momentum component p_z along the z axis can be calculated from the time-of-flight of the extracted particle, since the time-of-flight of a charged particle from the source point to the detector is then given by

$$t(p_z) = m\left(\frac{2a}{\sqrt{p_z^2 + 2mqU} \pm p_z} + \frac{d}{\sqrt{p_z^2 + 2mqU}}\right) \tag{2.4}$$

with the "±" sign in the first denominator depending on acceleration direction of the particle with respect to the z axis. The parameter a is the length over which the charged particle is accelerated, d denotes the drift region length, m is the mass of the charged particle (electron or recoil ion) and U the voltage applied over the acceleration region. To retrieve the momentum p_z in the general case, a numerical method is needed, e.g. by using Newtons method with $f(p_z) = t(p_z) - t'$.

If the extraction potential qU is larger as $E_z = p_z^2/(2m)$, different ion species and/or charge states are well-separated peaks in the TOF spectrum. The position of the peak for an ion is given by

$$t_0 = t(p_z = 0) = \sqrt{\frac{m}{qU}}(2a + d) \tag{2.5}$$

for $qU \gg E_z$. With this approximation and, since in this work no drift region is used, with $d = 0$, the momentum p_z calculation can be simplified to

$$p_z = \Delta t q \frac{U}{a} \tag{2.6}$$

with Δt the deviation form t_0.

Momentum in Detector Plane/xy Plane

To reconstruct the momentum in the detector plane/xy plane, view the system in cylinder coordinates. The charged particle starts at the source volume with the momentum magnitude p_{xy} in the xy plane and the angle ϕ. The magnetic field in z direction will force the particle on a cyclotron trajectory. The cyclotron frequency is given by

$$\omega_\mathrm{c} = \frac{2\pi}{T_\mathrm{c}} = \frac{q}{m} B_z \tag{2.7}$$

with q/m the charge-to-mass ratio and B_z the magnetic field in z direction. The cyclotron time T_c can be determined experimentally from the electron position vs.

time-of-flight plot. This is usually more accurate than external magnetic field measurements, but only possible if the electron does at least a half turn, so that two nodes are visible to determine T_c. The recoil ions are usually not doing a full revolution. The cyclotron radius R_c can be expressed by

$$R_c = \frac{T_c}{2\pi m} p_{xy} \tag{2.8}$$

in dependence of particle momentum magnitude p_{xy}. The angle between the particle origin and the hit position $\alpha = \omega_c t$ with t the absolute time-of-flight of the particle (basically a measure of the number of turn the particle does on the cyclotron trajectory). Then R_c can be determined by

$$R_c = \frac{r}{2|\sin(\alpha/2)|} \tag{2.9}$$

with r the hit position radius on the detector (in cylinder coordinates). The momentum in the xy plane can then be determined from the hit position r, θ (cylinder coordinates) and the cyclotron frequency ω_c (determined from electron position vs. tof plot) with the following expressions

$$p_{xy} = \frac{\omega_c m r}{2|\sin(\omega_c t/2)} \tag{2.10}$$

$$\phi = \theta \pm \frac{\omega_c t}{2} \mathrm{mod}(2\pi). \tag{2.11}$$

The sign of the second term for ϕ is dependent on rotation direction (magnetic field direction or charge sign of particle). Transformation to Cartesian coordinates can be done with normal coordinate transformation.

Without magnetic field (or if the magnetic field effect is negligible for high-mass ions): the momentum in the xy plane is then given by

$$p_{xy} = \sqrt{2}\frac{m}{t} r \tag{2.12}$$

$$\phi = \theta. \tag{2.13}$$

The Cartesian coordinates can then again retrieved with a normal coordinate transformation.

2.4.2 Momentum Resolution Limit

The momentum resolution depends on how well the external factors are known, like the extraction voltage or the acceleration distance. But, the time resolution and the source-volume uncertainty are usually dominant. The expected momentum

resolution σ_z in z direction can be calculated from Eq. (2.6) with Gaussian error propagation, yielding

$$\sigma_z = \sqrt{(qU\sigma_t/a)^2 + (q\Delta t\sigma_U/a)^2 + (\Delta t qU\sigma_a/a^2)^2}. \tag{2.14}$$

This expression is valid for ions and electrons, since Eq. (2.6) is independent of mass. With an extraction voltage of $U = 20\,\mathrm{V}$ with 2 % uncertainty over an acceleration region $a = 21\,\mathrm{cm}$ with an uncertainty $\sigma_a = 1\,\mathrm{mm}$ and a time-of-flight change of $\Delta t = 100\,\mathrm{ns}$ with a time resolution of $\sigma_t = 4\,\mathrm{ns}$ will lead to $p_z = 0.766\,\mathrm{a.u.}$ with $\sigma_{p_z} = 0.034\,\mathrm{a.u.}$ If only the time uncertainty is taken into account, the momentum uncertainty would still be 0.031 a.u.

For a certain electron time-of-flight the radial displacement r in the detector plane is proportional to the momentum in the xy plane p_{xy}, therefore $\Delta p_{xy,\mathrm{el}} = p_{xy}\Delta r/r$ with Δr the effective position uncertainty from detector resolution and target size (often the target size/source volume is dominating). Since $x = r\cos(\phi)$ and $y = r\sin(\phi)$ the error for p_x and p_y is $\leq \Delta p_{xy}$. Similarly for ions, the resolution would be $\Delta p_{xy,\mathrm{ion}} = \frac{\Delta r}{2a+d}\sqrt{qUm}$.

2.5 Supersonic Gas Jet

Supersonic gas jets are a well established technique and only the technical aspects relevant to the CSR-ReMi will be discussed here. A theoretical description of supersonic gas expansion can be found in [44]. For collision experiments between stored ions and neutral atoms or molecules the CSR-ReMi has a 11-fold (4 dump stages, 7 jet stages) differentially pumped supersonic expansion gas jet orthogonal to the ion beam. Fig. 2.13 shows a schematic overview of the production chamber, the differential pumping stages and the gas dump. The gas jet is produced by supersonic expansion from a 30 µm conical nozzle with typically 5-7 bar backing pressure. The particles with small transversal momentum are selected by placing a 0.2 mm skimmer in the so-called zone-of-silence (zone of supersonic flow). The transversal momentum is further reduced by a second skimmer (0.4 mm diameter) in the second stage. In total seven differential pumping stages separate the gas jet nozzle from the CSR experimental vacuum to avoid unnecessary gas load in the CSR. The differential pumping stages are connected with 2 mm apertures and the stages 5, 6 and 7 are equipped with movable slits (one horizontal and two vertical) to control the diameter of the gas jet.

After passing through the ReMi spectrometer and exiting the CSR experimental vacuum the gas jet is passed through three differential pumping stages and destroyed in a dump pump [24]. To avoid back-scattering into the experimental vacuum the differential pumping stages are separated by apertures with tubes (between stage 8 and 9 with 8 mm diameter and 60 mm length, between the other dump stages with 10 mm diameter and 100 mm length).

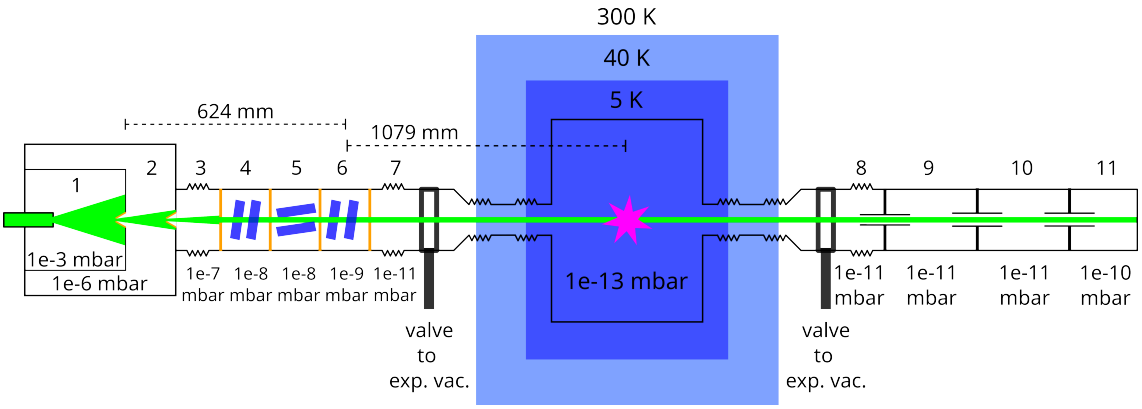

Figure 2.13: Jet scheme. The gas jet is produced in stage 1 and 2 by supersonic expansion from a 30 µm nozzle interacting with 0.2 mm and 0.4 mm skimmers. The differential pumping stages 4, 5 and 6 are equipped with movable slits to control the beam diameter. In stage 7 the gas jet transitions into the in-coupling chambers and is passed into the cryogenic environment. After passing through the CSR-ReMi the gas jet is then destroyed in a 4-fold differentially pumped dump, to avoid back-scattering into the experimental vacuum.

2.5.1 Gas Jet In-Coupling

To connect the gas jet production beam line and dump, described above, with the CSR experimental vacuum a specialized gas jet in-coupling is used. The first part of this in-coupling system are the differential pumping stage 7 on the jet production side and the stage 8 on the dump side, the in-coupling chambers. To avoid any unnecessary gas load on the experimental vacuum the in-coupling chambers are each pumped by a turbo molecular pump [24] and an ion getter pump [25]. The in-coupling chambers are connected to full-metal gate valve, which isolate the experimental vacuum, when the gas jet is not in use, since the in-coupling tubes behind the gate valve lead directly into the experimental vacuum. The gas jet in-coupling tubes have 16 mm diameter and allow passage of the gas jet from the 300 K stage to the 5 K part.The tubes are thermally decoupled by two membrane bellows at the 300K-to-40K and the 40K-to-5K transition. Additionally, the tube is thermally anchored at 40 K and connected to the 40 K Helium cooling circuit via a high purity (99.997%) copper band.To reduce the gas load on the experimental vacuum St 707 NEG strips are placed into the first section of the in-coupling tubes (see Fig. 2.14 left). The amount of 300 K radiation scattered into the CSR is minimized by lining the 40 K section of the in-coupling tube with Acktar metal velvet foil [45] (see Fig. 2.14 right), which will absorb most 300 K radiation hitting the 40 K tube wall. Also, a 10 mm aperture is placed at 40 K to further reduce the thermal radiation from room temperature reaching the 5 K environment.

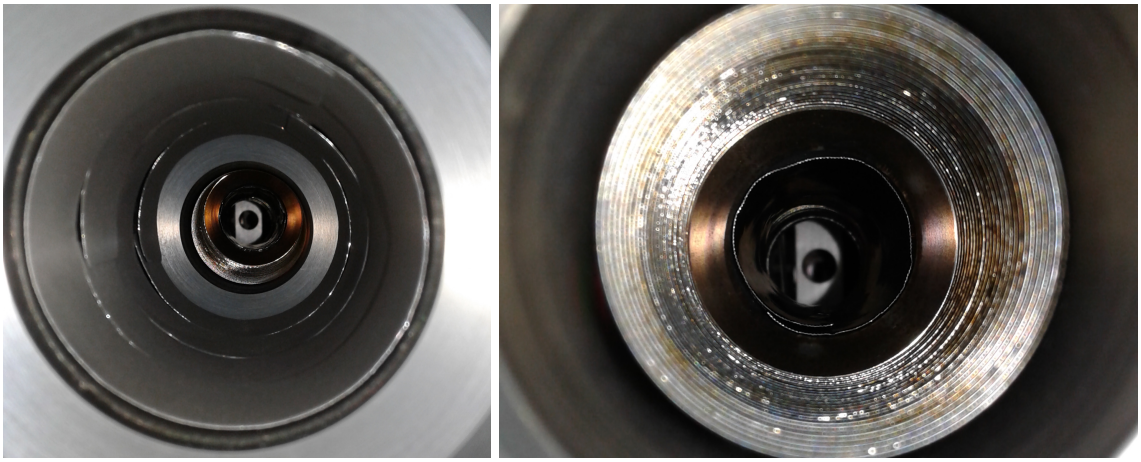

Figure 2.14: Left: NEG strips on the 300 K section inside one of the laser in-couplings (jet in-couplings are similar).
Right: Acktar metal velvet foil on the 40 K section inside one of the laser in-couplings (jet in-couplings are similar).

2.6 Laser

A LASER (Light Amplification by Stimulated Emission of Radiation) is a source for coherent light. A general introduction can be found e.g. in [1] ch. 8 and will be omitted here. A Coherent OBIS 637 nm CW laser with a nominal maximum beam power of 140 mW was used for the laser commissioning beam time and the photo-detachment experiment discussed in chapter 3. Fig. 2.15 shows a schematic overview of the laser setup. The lenses L1 with focus length -50 mm and L2 with focus length 300 mm form a telescope setup to focus the laser beam to a size of about 0.2 mm. A $\lambda/2$ plate was used to switch between horizontal and vertical polarization for the experiment. The laser beam is dumped on a black window cap after passing out of the exit laser window.

The laser line is tilted 25° relative to the gas jet, 65° relative to the ion beam. But, apart from the angle, the setup of the laser in-coupling is almost identical to the jet in-coupling (see section 2.5.1). The laser in-coupling chambers are mounted directly on the outside of the isolation vacuum chamber and equipped with 64 mm laser windows. Like the in-coupling tubes for the gas jet the laser in-coupling tubes are thermally decoupled with bellows and equipped with NEG strips in the 300 K section and Acktar metal velvet foil at 40 K. For a high-power laser system the laser beam needs to be passed de-focused through the laser windows to avoid damage to the windows. Since the distance between the airside and the interaction region is at least 70 cm, the laser needs to be focused down over a large focal length and the laser in-coupling tube diameter at the entrance needs to be large enough to accommodate the mostly de-focused laser beam. The laser in-coupling tube diameter is 50 mm at

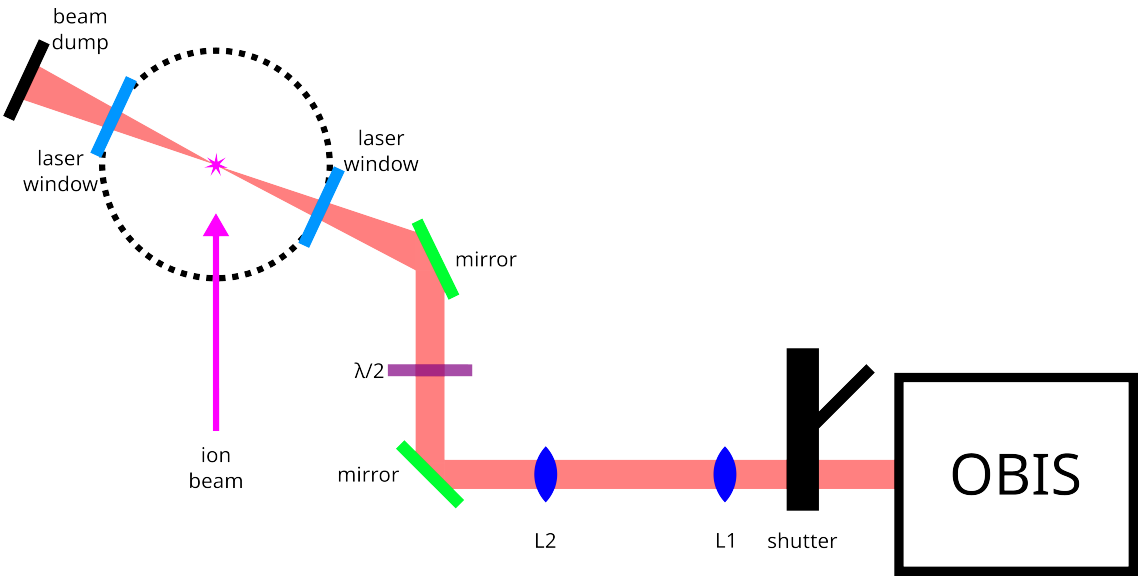

Figure 2.15: Overview of the laser setup. The laser line is tilted 65° relative to the ion beam. The dashed circle represents the CSR experimental vacuum, all other components are in air. The lenses L1 ($f = -50\,\text{mm}$) and L2 $f = 300\,\text{mm}$ form a telescope to control the beam size. The laser polarization is controlled with a $\lambda/2$ plate.

the 300 K side and then narrows down to 26 mm on the 5 K side, as the laser diameter is shrinking, to reduce thermal radiation into the CSR. Also, no aperture was placed at 40 K to not restrict the laser in-coupling.

2.7 Position Correction

Fig. 2.16 shows the ion detector position image, the neutral detector position image and the summed up counts along the x axis for the ion and neutral detector for Ar^+ ion beam interacting with the background gas (mostly hydrogen). The ion beam diameter in the CSR is $\approx 2\,\text{cm}$. The gas jet or laser have typically a diameter around or below 0.5 mm. The overlap of the ion beam with the jet/laser is not a small, well define interaction volume, but a long, thin cylinder. This would severely limit the resolution of the spectrometer, since the momentum resolution depends directly on the position resolution and therefore the source extension ([28] ch. 2.2.2).

For small ion beam divergence in x direction and small scattering angle of the projectile, the x position of the ion and the x position of the neutralized projectile of one event correlate, since the have the same origin position. The ion beam divergence in the x direction, in the CSR-ReMi section, is small, since the neutralized projectile beam is not spreading over a larger area, see Fig. 2.16 bottom. Since the

background gas is mostly hydrogen and the ion beam is Ar^+, no relevant deflection of the neutralized projectile is expected. And for many interactions the scattering angle will also be small, since e.g. for a 15.75 eV transversal energy transfer (argon ionization energy [39]), with an Ar^+ ion beam energy of 30 keV, a scattering angle of ≈ 0.53 mrad is expected (see section 5.1.1). This would correspond to a scattering cone opening spread of about 2.3 mm on the neutral detector or about 1/10 of the neutral spot diameter.

Fig. 2.17 shows a schematic overview of the extended ion beam interacting with the gas jet. The magenta cylinder is representing the ion beam and the magenta arrows represent the projectile ions which are neutralized and continue to the neutral

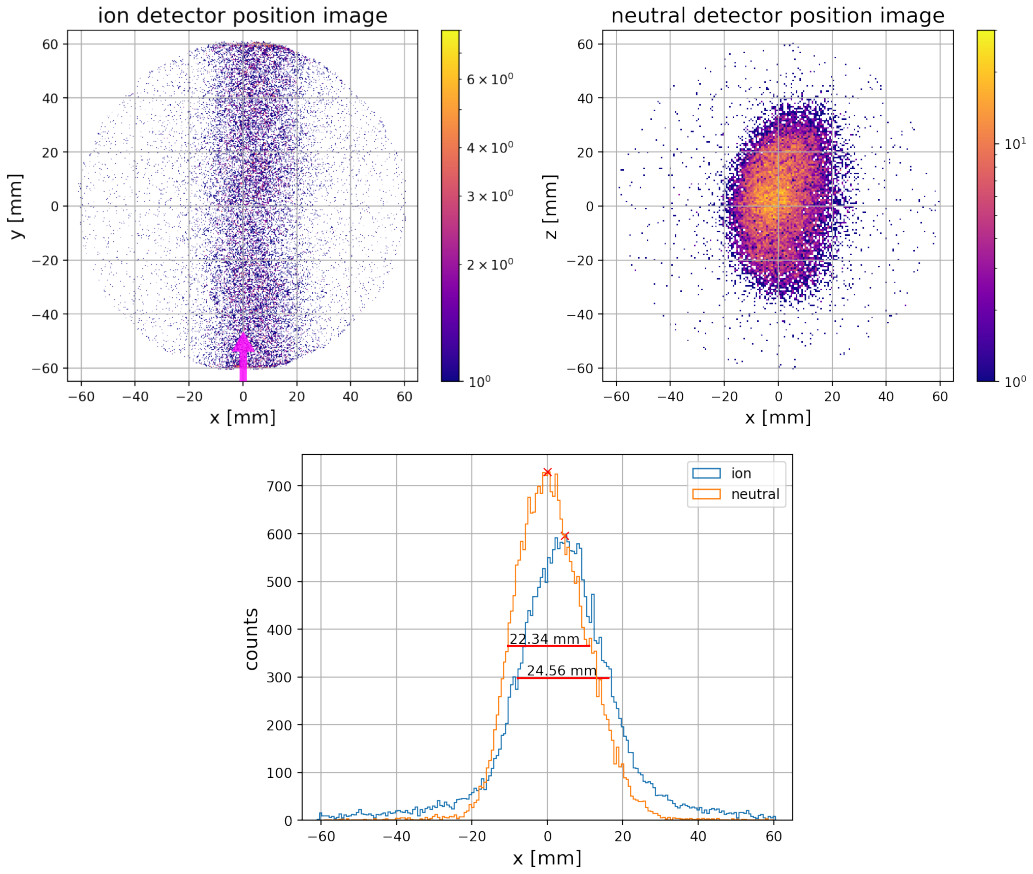

Figure 2.16: Ion beam diameter (ion-neutral detector coincidence condition), Ar^+ beam with 30 keV beam energy only interactions with background gas (mainly hydrogen), ≈ 3.9 V/cm extraction field, only earth magnetic field. Top: position image of the ion and neutral detector. The magenta arrow in the ion detector image marks the ion beam direction. Bottom: projection on x axis and FWHM.

detector. As one can see, the interaction volume is well defined in the z direction (TOF direction) and in the y direction (ion beam direction). For experiments with the gas jet, the events can then be shifted in x direction to achieve a smaller effective source volume. The correction for the x positions for the electron (x_{el}) and the ion (x_{ion}) is

$$x_{\mathrm{el/ion}} = x_{\mathrm{el/ion}} - x_{\mathrm{neut}} \tag{2.15}$$

with x_{neut} the x positions of the neutral detector (the detector x axis must point in the same direction).

For photo-detachment experiments the position correction for the electron detector x direction is

$$x_{\mathrm{el}} = x_{\mathrm{el}} - x_{\mathrm{neut}}. \tag{2.16}$$

But, since laser has 65° angle relative to the ion beam the y direction also needs to be shifted by

$$y_{\mathrm{el}} = y_{\mathrm{el}} - \tan\left(\frac{25°}{180°}\right) x_{\mathrm{neut}}. \tag{2.17}$$

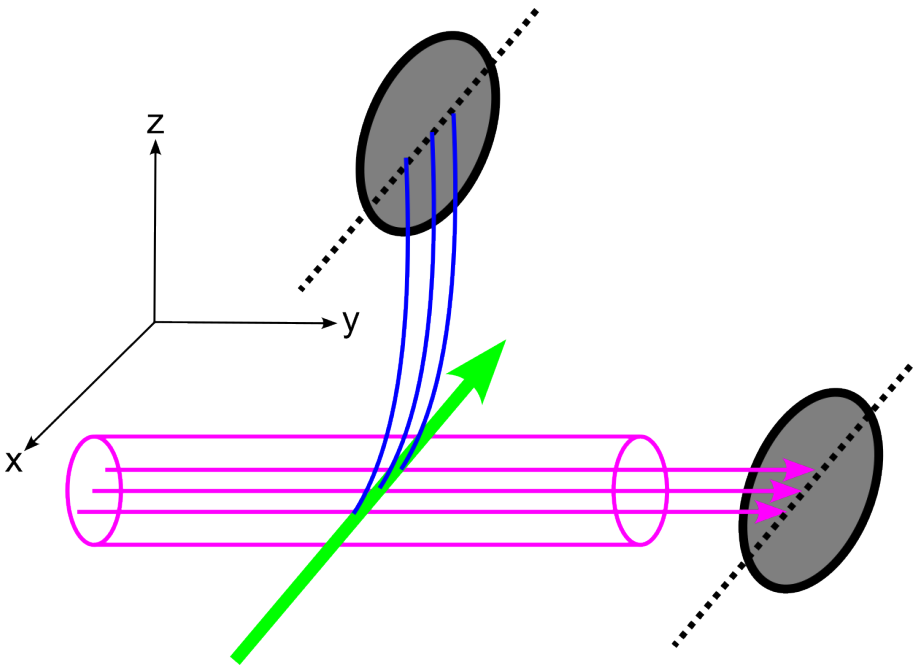

Figure 2.17: Position correction scheme for electrons ejected in an interaction between the ion beam and the gas jet. The ion beam is marked in magenta, the gas jet in green and the extracted electrons in blue. The magenta arrows represent the projectile ions which are neutralized and continue to the neutral detector.

Since the absolute time-of-flight (TOF) of the charged particles in the spectrometer is determined with the neutral hit time (see section 2.3.2), the different origin positions along the y axis will lead to changes in neutral flight time and therefore, to shifts in the time-of-flight. For 20 mm ion-beam diameter and 25° laser angle the displacement in y direction is around 9.3 mm. For a 15 keV beam of CH^- (13 amu mass) this would result in a neutral TOF difference of 13.9 ns, which corresponds to an electron momentum of about 0.03 a.u. for a 0.48 V/cm extraction field and 1.94 Gauss magnetic field. If higher precision along the TOF axis (z axis) is needed, this needs to be taken into account.

2.8 SIMION Simulation

To investigate the imaging properties expected from the CSR-ReMi, the spectrometer and redirection plates potentials are modeled in SIMION 8.1.1.32 [46]. A static magnetic gradient was also included in the simulation.

Fig. 2.18 shows one half of the xy detector plane (half circular area). The magenta arrows mark the ion beam incidence direction and the green arrow the gas jet direction. The electric extraction field is 0.98 V/cm. The trajectories of argon or helium ions, with different starting momenta and starting positions along the jet direction, are projected on the xy plane. The trajectories for each ion are shown once with and once without a magnetic field of 5 Gauss, which would be a typical field for ReMi operations. In the simulation without magnetic field, no strong distortions are visible. The helium ions are deflected by the magnetic field, but do not make a full cyclotron turn. This deflection can be compensated by rotating the detector image accordingly. The argon ions are mostly unaffected by the magnetic field. Therefore, the influence of the magnetic field on ions is mostly negligible or easily compensated.

In contrast, the magnetic field has a very defined effect on the electron trajectories. Fig. 2.19 shows electron trajectories, with a starting momentum of about 1 a.u. in a 5 Gauss magnetic field with 0.98 V/cm extraction field, emitted equidistant along the jet direction. The electrons perform about 2.8 cyclotron turns till they reach the detector. Because of this the numeric calculation of the electron momentum described in section 2.4.1 is necessary and still the electron momentum in z direction is ambiguous at the nodal point of the cyclotron rotation, since for all momenta the electron will pass through this nodal point. But all electrons of equal momentum follow a similar trajectory, apart from the two outermost electrons which hit an electrode and are lost. Therefore, the position correction (see section 2.7) can be used for the electrons and ions.

Fig. 2.20 shows the extension of a 1 mm × 1 mm source volume of argon ions propagated to the detector position by a 0.98 V/cm electric field with a 5 Gauss magnetic field. The linear extraction field used here images the source volume 1-to-

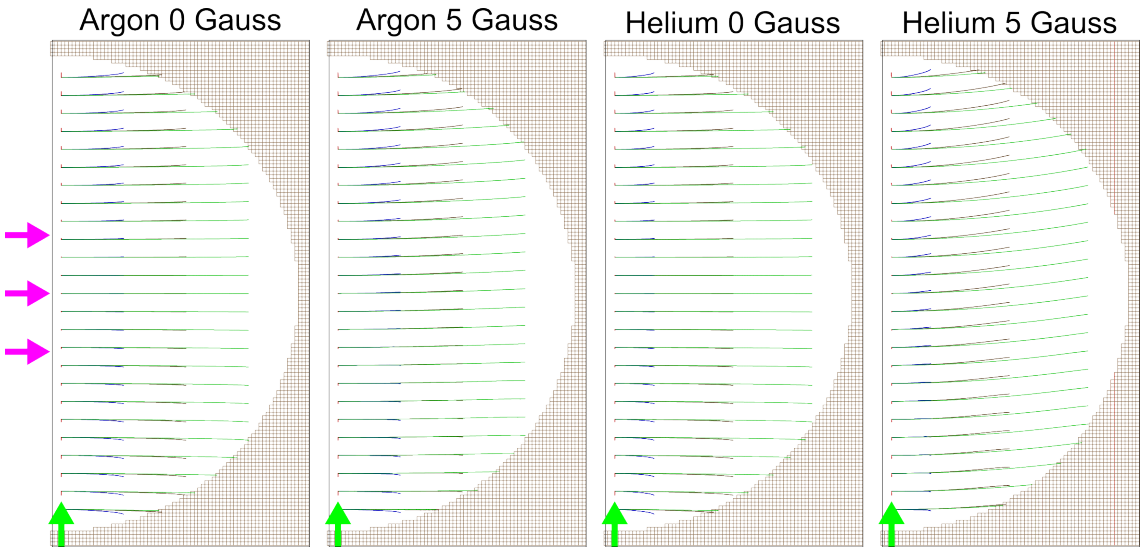

Figure 2.18: SIMION simulation of argon and helium ions projected on half of the xy plane (detector plane) with and without a magnetic field of 5 Gauss. The ions are emitted along the jet path with different initial momenta (25 ions equidistant per momenta). The initial momenta of the argon ions are 40 a.u. (green), 27 a.u. (black), 13 a.u. (blue) and 0 a.u. (red). For the helium the initial momenta are 13 a.u. (green), 13 a.u. (black), 3 a.u. (blue) and 0 a.u (red). The electric extraction field is 0.98 V/cm. The magenta arrows on the left mark the ion beam direction for all plots. The green arrows give the gas-jet position.

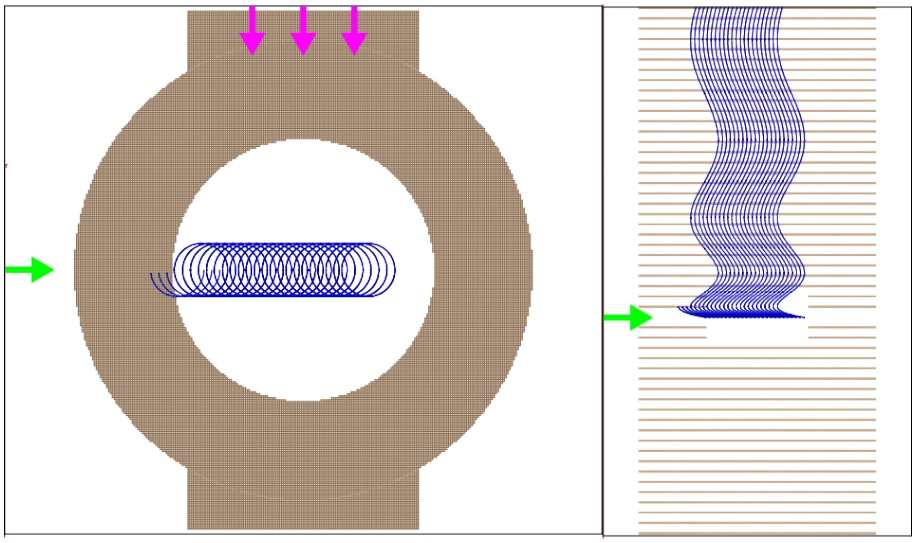

Figure 2.19: Left: Electron path (blue) with 5 Gauss magnetic field, 0.98 V/cm electric field and a starting momentum of about 1 a.u. Right: Same fields but viewed from ion-beam direction.

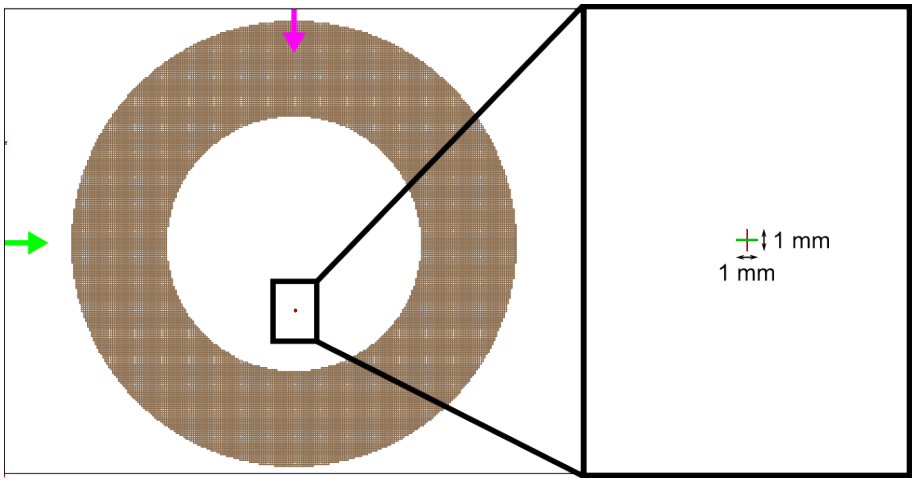

Figure 2.20: Detector image from a extended source with 1 mm × 1 mm extension. The ring represents a spectrometer electrode. Argon ions with 27 a.u. initial momentum in 0.98 V/cm electric field with a 5 Gauss magnetic field. The magenta arrow marks the ion beam direction, the green arrow the jet position.

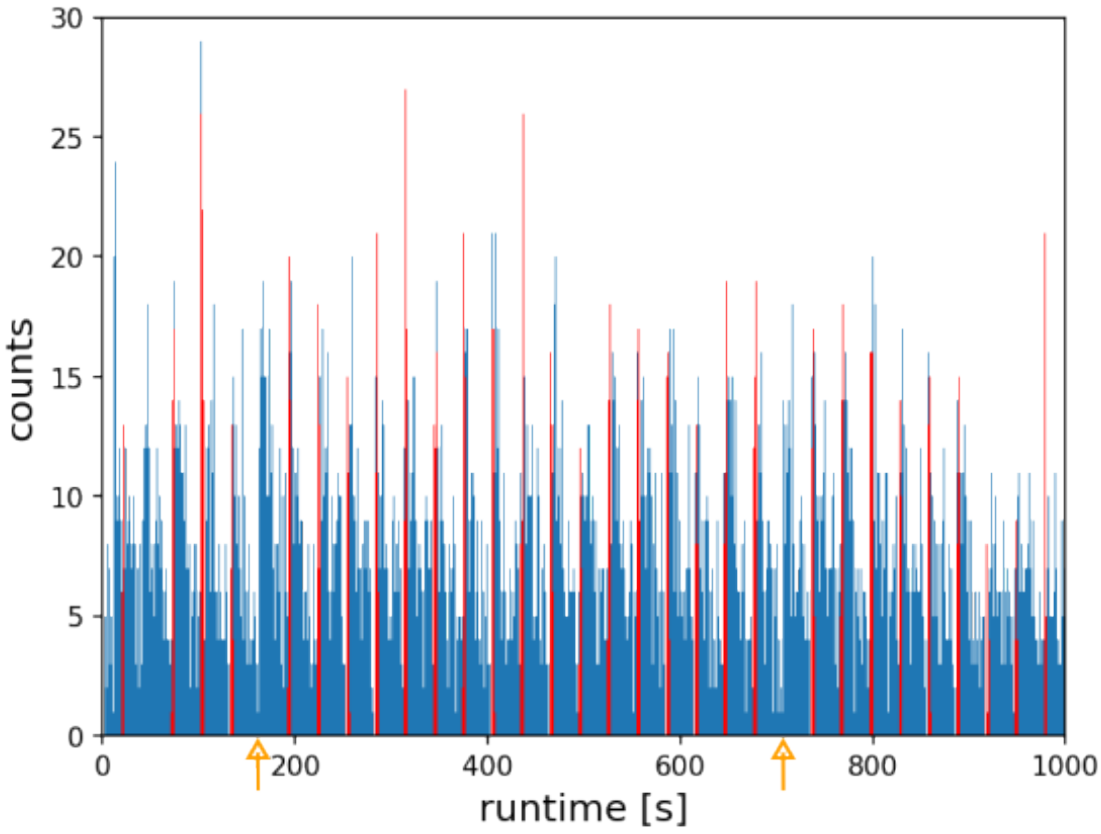

Figure 2.21: Example of injection time detection for the count rate of the neutralized projectiles in the first 1000 s of a Ar^+ (@30 keV) + He measurement with injection every 30 s. The detected injections are marked red. The orange arrows mark injections which were not detected.

1 on the detector plane without magnification or optical distortion.

2.9 Ion Beam Storage Time Determination

The storage time of the ions in the CSR is an interesting parameter for many experiments (e.g. [18, 19]). To track the storage time the CSR injection system provides a TTL injection signal. For the CSR-ReMi the injection signal was used in the DAQ setup (see section 2.4), but not directly logged. Some experiments presented in this thesis do require information on the storage time, therefore a temporary storage time determination method was developed.

Before a new injection the beam is dumped, since the injection deflector potential is switched to ground. Between this and the new injection the count rate on the neutral detector will be zero (neglecting dark counts), since no ion beam is present

to produce neutrals from interaction with the target or from recombination with residual gas. This period of near zero counts lasts for $\approx 0.5\,\mathrm{s}$ and is followed by a strong peak in count rate from the fresh beam. This can be used as a signature to detect the injection time. Fig. 2.21 shows the count rate of the neutralized projectile detector for the first 1000 s of a Ar^+ (@30 keV) + He measurement with injection every 30 s (this measurement will be discussed in chapter 5). The detected injections are marked in red. Most injections are detected with this method. The not detected injections (orange arrows) lead to longer storage time windows and are therefore removed if a storage-time condition is added.

2.10 Preliminary Characterization: Vacuum Quality in the CSR-ReMi

The residual gas density in the CSR-ReMi central chamber can be estimated from the count rate of projectile recombination with residual gas. The recombination rate is

$$R(t) = \frac{\sigma n l N(t) f_0}{\epsilon} \tag{2.18}$$

with $N(t)$ the ion number in the CSR, n the residual gas density, $l = 2r = 12\,\mathrm{cm}$ the interaction length/detector diameter, f_0 the revolution frequency and the detector efficiency $\epsilon \approx 0.3509$ (see section 2.3.2).

The rate from projectile recombination with residual gas for a 30 keV Ar^+ beam was 60 Hz (count rate on the ion detector). For this beam the revolution frequency was $f_0 = 10.2\,\mathrm{kHz}$ and $N(t) \approx 10^8$. The cross section σ for $Ar^+ + H_2$ at this collision energy is $\approx 0.86 \cdot 10^{-15}\,\mathrm{cm}^2$ [47]. The residual gas density is then $n = 2000/\mathrm{cm}^3$. Since the temperature of the CSR-ReMi linear section was higher (at 10-16 K, not 5 K) than expected, due to some thermal short circuits and a particle density of about 1000 particles/cm^3 was determined at the commissioning of the CSR [6], a particle density of $2000/\mathrm{cm}^3$ in the CSR-ReMi central chamber is a good value.

2.11 Interference Noise Signal and Mitigation Method

During the setup phase (when the first detector was tested inside the CSR) a very strong interference signal with a frequency peak around 100 MHz was noticed. It is speculated that the interference signal originates in a switching power supply, but the exact origin is unclear. Additionally, the interference changes with time and no pattern was yet found.

The interference has the strongest effect on the MCP signal. The interference is also seen on the delay lines, but the background subtraction with the reference wires reduces the interference signal significantly. A differential box to subtract the interference signal from the MCP signal with the ring anode as a reference was built. The neutral detector uses the otherwise unused grid ring as a reference, since for the neutral detector no grids were mounted and the grid ring diameter is closer to the MCP diameter. This does not completely solve the problem, but the detectors are usable. The investigation into the source of the interference signal is ongoing.

3 Electron-Photo-Detachment

This chapter discusses the electron-photo-detachment of CH^- as a proof-of-principle experiment for electron spectroscopy and the CSR-ReMi laser commissioning. Section 3.1 gives a short introduction to photoelectron imaging and subsection 3.1.1 an overview of the electronic properties of CH^-. The experimental parameters relevant for this chapter are summarized in section 3.2. In section 3.3 first the photo-electron binding energy is compared to literature and then the electron momentum plots investigated to identify the present transitions.

3.1 Introduction to Photoelectron Imaging

Several negative molecular ions, like CN^-, C_2H^- or C_4H^-, have been detected in space [48], but the nature of many large negative ions is unclear, especially at low temperatures. The CSR provides a unique environment for the investigation of cold molecular ions and this is one of the main purposes of the CSR. Photoelectron imaging can be used to investigate the electron binding energies and electronic structure of molecules (see [49, 50] for more details) by photo-detaching at least one electron from the parent-ion and projecting it on a position-sensitive detector. The incident electrons form a pattern, a two-dimensional projection of the three-dimensional electron momentum distribution. With a reaction microscope, in many cases, all three momentum components can be reconstructed by taking the electron time-of-flight into account (see section 2.4.1). The electric field vector defines a unique axis in space. From the anisotropic characteristics of the photoelectron distribution produced with a polarized laser, the symmetry properties of the parent-ion electron orbitals and the dynamics of the detachment process can be deduced. For molecular ions, the molecular axis can introduce an additional relevant direction in addition to the laser polarization in the laboratory frame.

3.1.1 Properties of CH^-

The negative molecular ion CH^- was chosen as a proof-of-principle projectile for the laser commissioning. It is easy to produce with a Cs sputter source available at the CSR. The photo-electron energy was already measured by [51] and there are velocity-map imaging (VMI) measurements available by e.g. [52]. Also, this ion was already used in lifetime measurements of the metastable $a^1\Delta$ state in DESIREE [53]. The electron affinity of CH^- is 1.24 eV [51], easily reachable with a commercial

off-the-shelf laser (see section 2.6 for laser setup). The CH^- ion beam in the CSR is expected to be vibrationally cold, since the vibrational excitations are expected to cool in the CSR within $\approx 0.5\,s$ (see [19]).

The electronic structure of CH^- is $(1\sigma)^2(2\sigma)^2(3\sigma)^2(1\pi)^2$ (see [52]). The ground state ($X^3\Sigma^-$) has two unpaired π electrons with parallel spins, following Hund's first rule. The excited state ($a^1\Delta$) state has antiparallel spins, making it a singlet state. The $a^1\Delta$ state is metastable with a lifetime of $14.9 \pm 0.5\,s$ [53]. The ground state of the neutral CH is $(1\sigma)^2(2\sigma)^2(3\sigma)^2(1\pi)^1$ ($X^2\Pi$) and can be reached by detachment of one of the 1π electrons of CH^- [52]. The excited neutral state $(1\sigma)^2(2\sigma)^2(3\sigma)^1(1\pi)^2$ ($a^4\Sigma^-$) is produced by detachment of one of the 3σ electrons.

The electron binding energy determined by photo-detachment with a 355 nm (blue line) and a 532 nm (orange line) laser measured by Goebbert et al. [52] are plotted as a reference in Fig. 3.1. The $a^1\Delta$ state is expected to have an electron binding energy of 0.39 eV, but in the data from Goebbert et al. it is not observed. They speculated that the excited state is not produced in sufficient quantity in the used discharge ion source they used or it is deactivated before photo-detachment. Eklund et al. [53] produced CH^- in a cesium-sputter ion source – using ethanol vapor – for a lifetime measurement of the $a^1\Delta$ state in DESIREE. They used a laser photon energy of 1.16 eV to selectively photo-detach the $a^1\Delta$ state. Since a similar source is used here (cesium-sputter ion source with methanol), at least some of the CH^- is expected to be in the $a^1\Delta$ state. But it is possible that the $a^1\Delta$ state can not be distinguished from background, since Eklund et al. assume the relative population of the $a^1\Delta$ state is only about 10^{-3}.

3.2 Experimental Parameters

The full setup is described in detail in chapter 2 and only a summary of the important parameters will be provided here. The CH^- is produced in a Cs sputter ion source and accelerated to 15 keV, by the gradient between the platform potential and ground, into the CSR. The ion beam is mass selected with a dipole magnet. The natural abundance of $\approx 1.1\%$ [54] of ^{13}C will lead to a small contamination of the ion beam with $^{13}C^-$ ions, but this will not be relevant for the discussion here. The beam current decreases over the storage time, because of collisions with background gas. For the initial measurement a short storage time of 5 s was chosen to have a comparatively high beam current at all times. The ion beam was crossed at a 65° angle with a Coherent OBIS 637 CW laser with a nominal maximum beam power of 140 mW, see 2.6. The laser wavelength corresponds to a photon energy of 1.946 eV.

The detached photoelectron is extracted by an electric field of 0.46 V/cm towards the electron detector. A magnetic field of 1.34 Gauss is used to contain the electron on a cyclotron path. As described in section 2.7 the electron-hit position on the electron detector was corrected by the neutral-hit position along the x axis to reduce

Table 3.1: Overview of the CH^- photo-detachment experimental parameters.

ion	CH^-
electron affinity $X^3\Sigma^-$	1.24 eV [51]
electron affinity $a^1\Delta$	0.39 eV [51]
ion beam energy	15 keV
storage time Fig. 3.1, 3.2, 3.4	5 s
storage time Fig. 3.5	30 s
long. momentum spread	$\Delta p/p \approx 4.2 \times 10^{-4}$
particles in the ring	$\approx 10^7$
laser	637 nm (1.946 eV)
focus size	$\approx 200\,\mu$m
electric field Fig. 3.1, 3.2, 3.4	0.46 V/cm
electric field Fig. 3.5, A.2	4.9 V/cm
magnetic field	1.34 Gauss
resolution	$\Delta p \approx 0.03$ a.u. (expected)
	energy resolution @ zero mom ≈ 0.1 eV
	energy resolution @ 0.3 a.u. ≈ 0.3 eV
	(increases since $E \propto p^2$)
max electron mom. acceptance	about 0.7 a.u.

the effective source volume. A second dataset with a storage time of 30 s and a higher extraction field of 4.9 V/cm was acquired to try to resolve the $a^1\Delta$ state. For all measurements coincidence between electron and neutral hits is required. The experimental parameters are summarised in Tab. 3.1.

From the vector magnitude of the measured electron momentum the electron energy can be calculated. The best energy resolution is achieved for electrons with a binding energy just below the laser energy, since they are emitted with almost zero momentum. Since a fixed wavelength laser was used this limits the energy resolution at low binding energies.

3.3 Results of Electron Photo-Detachment from CH^-

Fig. 3.1 shows the electron binding energy of the photo-detached electron (blue and orange from [52], green and red from this measurements). For the electron binding energy marked by the red line the condition $p_z = 0 \pm 0.01$ a.u. was chosen, since the electron momentum in z direction is partially ill defined (see below and Fig. 3.3), leading to a broadening of the peak and introducing an artefact (shoulder at about 1.7 eV in the green line). The reference spectra (blue and orange lines), measured by Goebbert et al. [52], show two distinct peaks. The left peak corresponds to the transition from the CH^- ground state $X^3\Sigma^-$ (with electron configuration $\sigma^2\pi^2$) to

the CH ground state $X^2\Pi$ transition (with electron configuration $\sigma^2\pi$ in the target state). The right peak in the reference spectrum is attributed to the transition into the excited neutral state $a^4\Sigma^-$ by detachment of one 3σ electron. The binding energy for the 3σ electrons is given by Goebbert et al. with 1.98 eV to 1.99 eV, just barely above the laser photon energy. Only the shoulder of the 3σ peak can, therefore, be seen in the energy spectrum of the photo-detached electron (red line) directly at the laser photon energy (dashed red line). The red and green lines peak both at 1.2 eV, in good agreement with the reference spectra the electron binding energy of 1.24 eV for the ground state of CH^-. At around 1 eV binding energy, the energy resolution is expected to be at around $\Delta E \approx 0.3$ eV and therefore, this state can not be sharply resolved. The energy resolution is much better directly at the laser

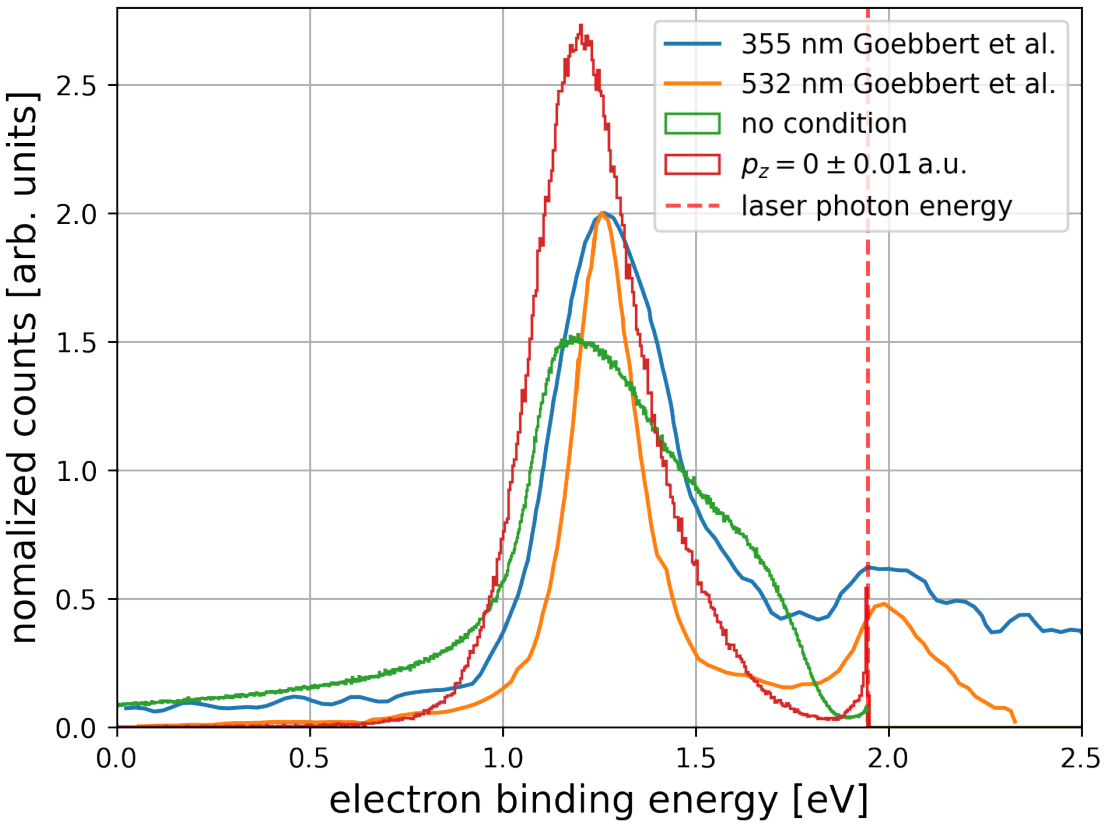

Figure 3.1: Electron binding energy of the photo-detached electron from CH^-. The green and red lines were measured in this work. The red dashed line marks the laser photon energy of 1.946 eV with 60 mW laser power. The blue and orange lines are from [52]. The peak at 1.24 eV corresponds to the transition to the CH ground state $X^2\Pi$ and the peak at 2 eV to the transition to the excited neutral state $a^4\Sigma^-$.

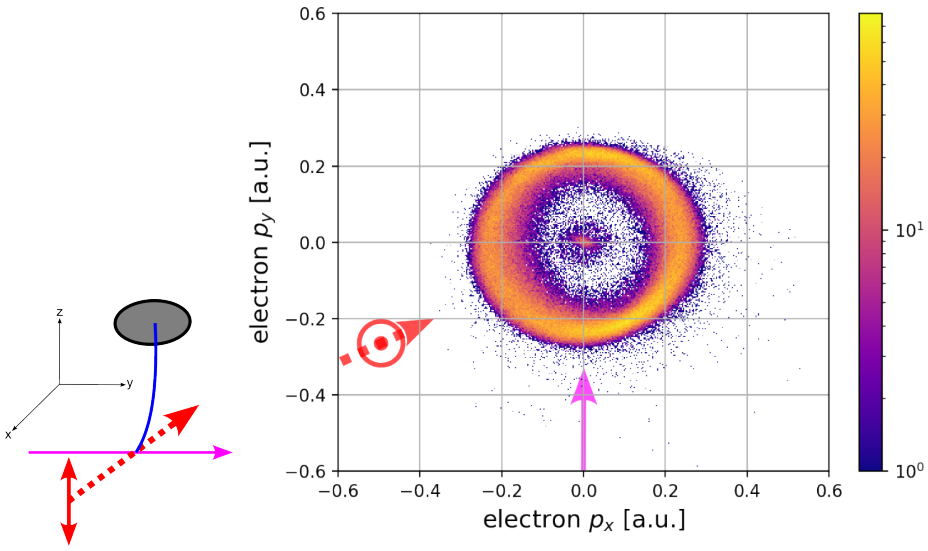

Figure 3.2: Electron momentum distribution of electron photo-detached from CH^- in the xy plane (detector plane) with vertical laser polarization, with condition $p_z = 0 \pm 0.01$ a.u. The magenta arrow indicates the ion beam direction.

photon energy (about $\Delta E = 0.1$ eV), where the electrons are emitted with almost zero momentum. The $a^1\Delta$ state would be expected at around 0.39 eV. In the energy spectrum no trace of the $a^1\Delta$ state can be seen.

Fig. 3.2 shows the momentum of the photoelectron in the detector plane ($p_z = 0 \pm 0.01$ a.u.) with the laser polarization orthogonal to the detector plane. The 3σ electrons emitted with almost zero momentum can be seen as a spot in the centre. At around 0.25 a.u. momentum a broad ring can be seen. This ring would correspond to the broad peak in the energy spectrum of Fig. 3.1 attributed to the transition to the CH ground state. The ring has no visible sub-structure and there is no second ring visible which could be attributed to the $a^1\Delta$ state. With an electron affinity of 0.39 eV [51] the signature of the $a^1\Delta$ state is expected at around 0.34 a.u. or just outside the broad ring. The varying thickness of the ring is a detector artefact due to ambiguity in the electron momentum reconstruction, since a cyclotron nodal point lies on the edge of the momentum sphere in z direction. Fig. 3.3 shows the electron momentum distribution in the xz and yz plane. The cyclotron path of the electrons has nodal points, marked by the orange arrows, were the momentum of the electron is ambiguous, see section 2.4.1 and 2.8. In theory the position of the nodal points can be chosen by selecting appropriate electric and magnetic fields, but the detector size and wanted resolution limits the available choices.

If the polarization is rotated 90°, as in Fig. 3.4, a two-lobe structure orthogonal to the polarization direction is visible in the detector plane. This two-lobe structure

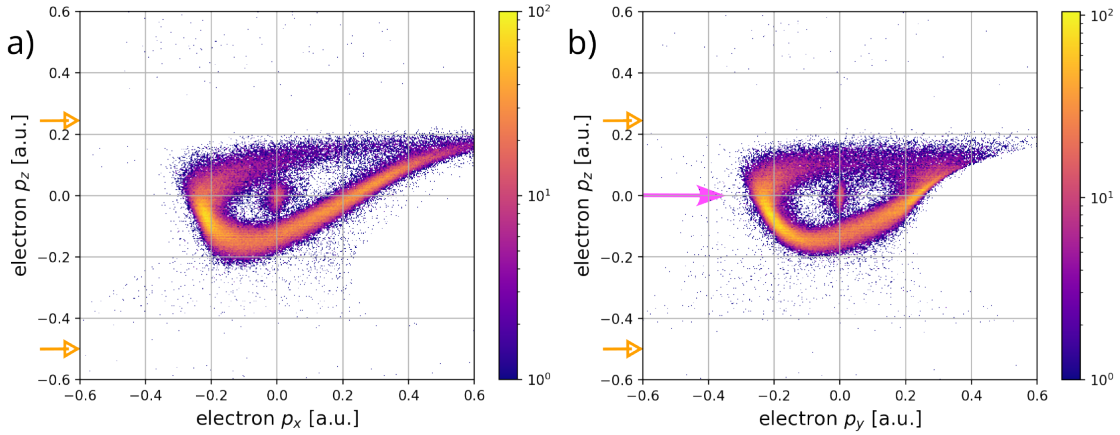

Figure 3.3: Electron momentum distribution of the photo-detached electron from CH^- with vertical laser polarization.
a) xz plane with condition $p_y = 0 \pm 0.01$ a.u., ion beam orthogonal to image plane.
b) yz plane with condition $p_x = 0 \pm 0.01$ a.u., the magenta arrow indicates the ion beam direction.
The orange arrows mark nodal points of the electron cyclotron path.

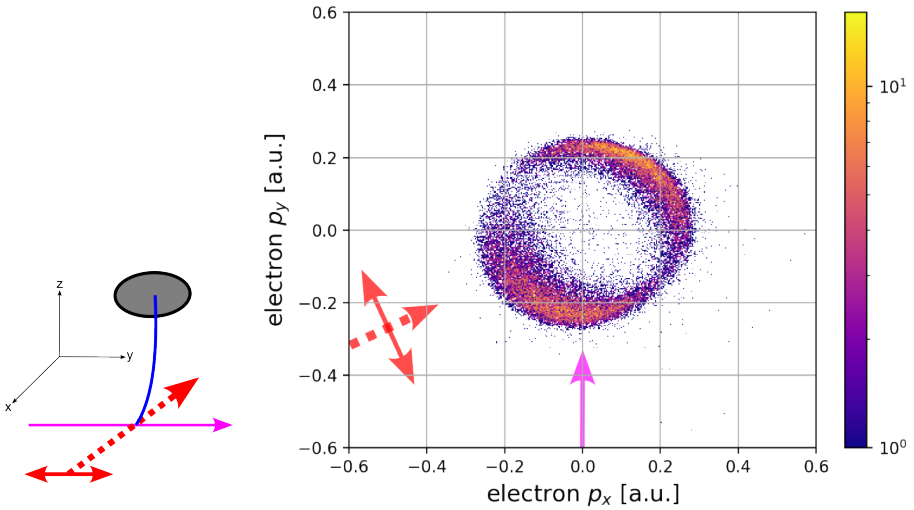

Figure 3.4: Electron momentum distribution of electron photo-detached from CH^- in the xy plane (detector plane) with horizontal laser polarization and 154 mW laser power, with condition $p_z = 0 \pm 0.01$ a.u. The magenta arrow indicates the ion beam direction.

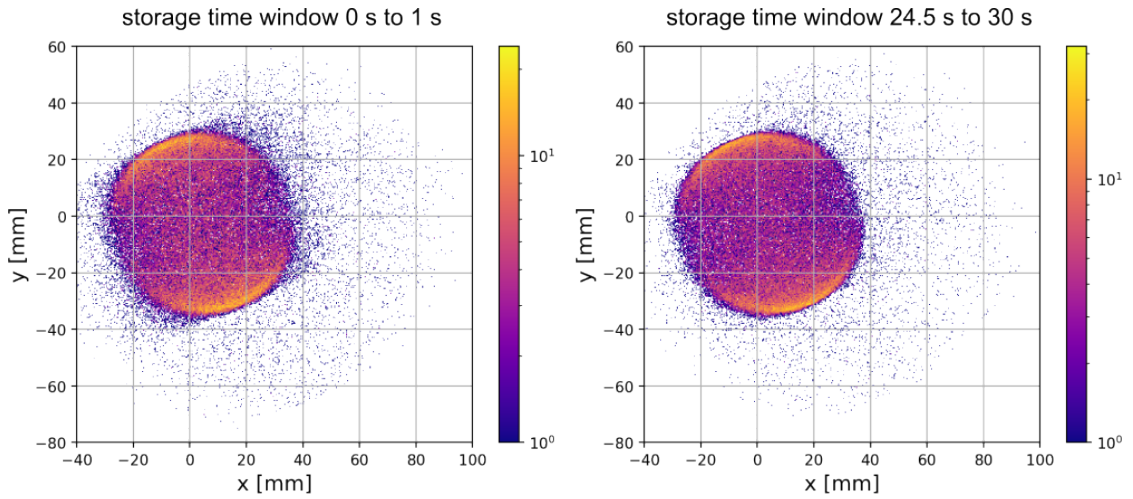

Figure 3.5: The electron hit position for 4.9 V/cm extraction field with the electron photo-detached from CH^- with 60 mW laser power in the xy plane (detector plane) with horizontal laser polarization for the storage time windows 0 s to 1 s and 24.5 s to 30 s. The different storage time windows are chosen to get a roughly equal number of counts in both windows (125646 counts for 0-1 s and 126835 counts for 24.5-30 s). The image rotation by the electron cyclotron motion is not corrected here.

matches the detector image from Goebbert et al. [52] and indicates that the photoelectron comes from a π state. Confirming that these photoelectrons come from the transition $X^3\Sigma^-(\sigma^2\pi^2) \rightarrow X^3\Pi$, $\nu = 0$ $(\sigma^2\pi)$ from the CH^- ground state to the ground state of neutral CH by detaching a 1π electron. The spot at zero momentum is not visible, probably because the total statistics in this sample is too low. Like for vertical polarization, no second ring as a signature of the transition from the $a^1\Delta$ state can be seen.

To see if the $a^1\Delta$ state is unresolved due to low statistics, more counts were collected. The extraction field is increased to 4.9 V/cm to ensure that all electrons are collected and to remove the cyclotron nodal points. Also, the storage time was increased to 30 s to look for changes as the $a^1\Delta$ state decays. Fig. 3.5 shows the electron hit position on the electron detector with the higher extraction field for two storage-time windows. For this extraction field the electrons have only time to make about 2/3 of a turn in their cyclotron motion and the image will be rotated. The rotation was left uncorrected. The unmodified (except for position correction) position images are shown here, since the $a^1\Delta$ state feature is best visible in them. The injection times were indirectly determined from the neutral detector count rate as explained in section 2.9. In the storage-time window 0s̀ to 1 s most of the $a^1\Delta$ state is still present and in the 24.5 s to 30 s window most is decayed. The edges of the storage-time window 0 s to 1 s seem a bit more 'fuzzy' than the edges fo 24.5 s to

30 s. Since only a small fraction of the CH^- ions are in the excited state and the $a^1\Delta$ state is expected directly outside the broad ground-state ring, this is interpreted as a signature of the $a^1\Delta$ state

To prove without doubt if the small contribution for 0 s to 1 s storage time is really the $a^1\Delta$ state or just part of the background, the $a^1\Delta$ state could be selectively detached with a laser of fitting wavelength in a follow up measurement. But, as a proof-of-concept experiment it is satisfactory that all features could be clearly identified. This shows that the laser in-coupling works well and can be used for experiments.

For measurements with high extraction field, like the one above, often no good TOF information is available or the magnetic field is even undesirable, since it rotates the detector image (as in Fig. 3.5) and can make the interpretation harder. The reconstruction of all three momentum components is then not possible. But, since the photoelectron distribution has cylindrical symmetry relative to the z axis the 3D momentum distribution can be mathematically reconstructed with the inverse Abel transformation. This is demonstrated with a CH^- photoelectron image in supplemental A.4.

4 Electron Loss and Target Ionization

This chapter discusses the interaction between stored negative ions and a neutral target as an example of a few-body process. Section 4.1 introduces the quasi-free electron model, a simple theory to describe the interaction of a loosely bond electron with a target. For electron loss with simultaneous target ionization a correlated and an uncorrelated interaction process are put forward. Section 4.2 gives, the basic experimental parameters relevant to this chapter. The measurement results for electron loss without target ionization are discussed in section 4.3. Section 4.4 identifies the correlated process as the dominant mechanism for electron loss with simultaneous target ionization. Since the fraction of simultaneous target ionization is surprisingly large, the cross-section ratio between electron loss with and without simultaneous target ionization is discussed in subsection 4.4.1.

4.1 Introduction of the Correlated and Uncorrelated Mechanisms

Most atoms can form negative ions by binding an extra electron to the neutral atom in a short-range potential [55]
A collision of a negative ion with a neutral atomic or molecular target can lead to a variety of inelastic transitions of one or more electrons. The focus here is on electron ejection from one or both collision partners. Electron ejection from the projectile is usually referred to as electron loss or, in the case of negative ions, electron detachment.

4.1.1 The Quasi-Free Electron Model

The additional electron of negative ions has usually a small binding energy, also called electron affinity [55]. For intermediate to high collisions energies (projectile velocity $v_P \gtrsim 0.5\,\text{a.u.}$) the bond of this electron is often neglected in the description of the collision. This is known as the quasi-free electron model [56, 57]. Here, the detachment is viewed as elastic scattering off the target and the core of the projectile as passive, since the negative ion is modelled as a single electron (corresponding to the outermost electron of the ion) and a neutral core. The single electron is attached to the core as a quasi-free electron orbiting around it with the velocity distribution of its electronic state. The total velocity of quasi-free electron is therefore the vector

sum of the projectile velocity plus the velocity of the electron in the bound state. No correlation between the single electron and the other electrons of the ion are considered in this model. Within the quasi-free electron model, the main task of theory is to calculate the elastic scattering cross section.

In the quasi-free electron model the electron loss interaction is comparable to the elastic scattering of a free electron. Fedus et al. [58] did Markov Chain Monte Carlo-Modified Effective Range Theory to calculate the differential elastic scattering cross sections for free electrons on noble gases. Their model shows good agreement with free-electron scattering experiments and can be used as a comparison to the measured quasi-free electron scattering (see Fig. 4.4 in section 4.3).

Macek et al. [59] present a zero-range potential model to calculate electron energy and angular distributions for atom-negative ion collisions. For a fast projectile with 10 a.u. velocity (the collision system is not given), Macek et al. predict a peak in forward direction[1] at $v_y/v_\mathrm{p} = 1$ corresponding to slow electrons in the projectile frame and a second peak at $v_y/v_\mathrm{p} = 0$ corresponding to slow electrons in the target frame and a ring attributed to binary encounter. For a slow projectile with 0.1 a.u. velocity, the binary encounter ring disappears and the projectile and target peak merged into a single peak. The projectile velocity for the fast collision is considerable larger than for the experiment presented below, but it seems reasonable to expect a ring-like structure due to the binary collision between target atom and a projectile electron.

4.1.2 Electron Loss with Simultaneous Target Ionization

For a bare positive ion the primary interaction in target ionization is necessarily the interaction between the projectile core (in this case the bare core) and the active target electron (the one which is removed). For a structured positively charged projectile (positive ion with some electrons) the core - target electron interaction still tends to be the dominant interaction for target ionization, since the effective nuclear charge is generally larger than the charge of the electrons.

In contrast, for negative ions the role of the projectile core - target electron interaction for electron loss with simultaneous target ionization is not clear. Target Ionization without electron loss could still proceed through the projectile core - target electron interaction. However, on its own, it can not lead to simultaneous target ionization, since this interaction would only remove an electron from the target, but not from the projectile. Therefore, a second interaction, e.g. between the target core and the projectile electron would be required (see Fig. 4.1 b). Since this represents two independent reaction steps (higher-order process) one would generally expect this to be weaker than a first-order process (single-step process). Additionally the core of a negative ion is effectively neutral, since from a larger distance the positive

[1] in this work the projectile beam direction is along the y axis

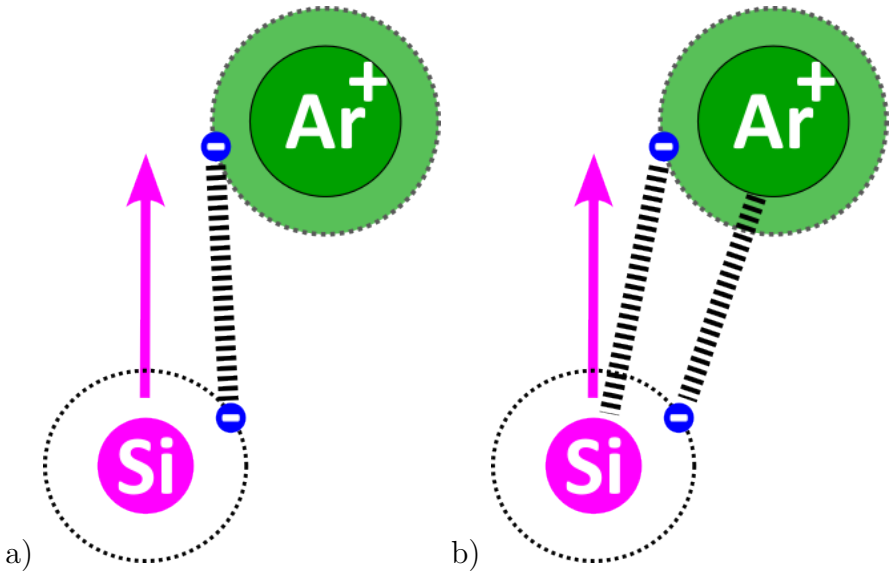

Figure 4.1: Schematic of correlated (a) and uncorrelated (b) process.

nuclear potential is shielded by the electrons. The neutral core should be relatively inefficient in ionizing the target.

A second possible scenario (the correlated process) would be that the active electron (the electron which is removed) of the projectile and the active electron of the target interact directly with each other (electron-electron interaction V_{ee}), which then removes both electrons, see Fig. 4.1 a). For large projectile energies and other processes with simultaneous transition of a projectile and a target electron the first-order processes are often important or dominant, see e.g. [60].

For smaller projectile energy (for argon target $v_P \lesssim 1$ a.u.) the electron-electron interaction is expected to be less important, since the electron kinetic energy is below ionization threshold. Once again, because of the small electron affinity (1.39 eV for Si^- [61]) the process can be described in the quasi-free electron model (see section 4.1.1). Electron loss with simultaneous target ionization is then viewed as target ionization by a free electron.

The ionization energy for argon (the target) is 15.76 eV [39]. A truly free electron would need at least this kinetic energy to kinematically allow target ionization. This means that, the threshold for a free electron to ionize the Argon target corresponds to a velocity of 1.07 a.u., which is considerably higher than the beam velocity of 0.66 a.u. (for 300 keV Si^- beam). But since the electron is actually in a (weakly) bound state, the available electron kinetic energy is determined by the vector sum of the projectile velocity and electron velocity in the initial bound state.

Fig. 4.2 shows a projection of the outer electron momentum distribution (Compton profile) on the y axis (beam direction) for Si^- (blue dots extracted from [56]). The projectile electron needs to have at least the threshold velocity v_t in the bound

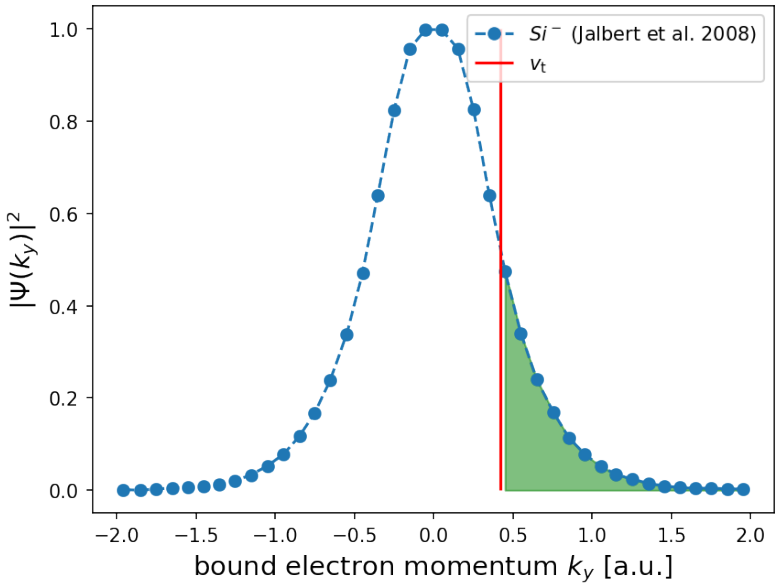

Figure 4.2: Compton profile for Si^- (blue dots, the dashed line was added as a guide to the eye) extracted from [56] with k_y the momentum of the electron in beam direction integrated over the perpendicular directions. The threshold velocity $v_t = 0.42\,\text{a.u.}$ needed to reach the Argon ionization level for a projectile velocity of $v_0 = 0.66\,\text{a.u.}$ is marked by the red line. The green shaded area above v_t corresponds to 15.8% of the profile.

state to have a kinetic energy above the ionization potential. This threshold velocity can be calculated by

$$v_t = \sqrt{\frac{2I_{Ar}}{m_e}} - v_0 = 0.42\,\text{a.u.} \tag{4.1}$$

with I_{Ar} the argon ionization potential of 15.76 eV [39] and $v_0 = 0.66\,\text{a.u.}$ (300 keV Si^- beam) the initial projectile velocity. The fraction of electrons above v_t is $\approx$ 15.8% (green shaded area). The weighted average velocity of the electrons above the threshold velocity (the electron in the green shaded area) is at 0.67 a.u. electon bound-state momentum. The (quasi-free) electrons from the green shaded area have therefore a total average kinetic energy of 23.9 eV.

It was initially expected, that the electron loss with simultaneous target ionization rate is considerably smaller than the electron loss rate without target ionization for two reasons:

- the independent channel should be weak because it involves two active electrons, not just one. Also the active target electron (only involved in target ionization) has a larger binding energy (15.76 eV [39]) than the active projectile electron (1.39 eV [61])

- the correlated first-order process could be weak as well because only a small fraction of the projectile electron momentum distribution (Compton profile, see above) have sufficient energy to contribute to the correlated first-order process

Since both processes are expected to be weak, the highest projectile beam energy of 300 keV available at the CSR was chosen. The experimental parameters are summarized in the following section.

Theoretical models to describe $Si^- + Ar$ collisions are practically not available due to the complexity of the system. However calculations were performed for the $H^- + He$ collisions with a projectile velocity of 2.83 a.u. by Ferger et al. [62]. They determine the longitudinal electron momentum for mutual ionization using the fist Born approximation (FBA) with a Yukawa potential for H^-. Since the FBA is a first-order approximation the mutual ionization can only happen by electron-electron interaction. They find the emitted target electron at $v = 0$ a.u. with a forward/backwards asymmetry caused by a relatively large longitudinal momentum transfer. The longitudinal projectile electron momentum peaks below the initial projectile velocity, since (in the target rest frame) the energy to overcome the binding energy of both electrons must be provided by the projectile electron. The comparison to experimental data suggests that the electron-electron interaction is dominant over higher-order processes for mutual ionization.

Transferring this model to $Si^- + Ar$, a slight forward/backwards asymmetry from longitudinal momentum transfer is expected for the correlated process. Since the mutual ionization needs all available kinetic energy (see above) the projectile and target-electron momentum peak will merge and both electrons are emitted with almost zero momentum.

4.2 Experimental Parameters

Tab. 4.1 shows an overview of the experimental parameters relevant in this section and the experimental setup is described in detail in chapter 2. The Si^- ions are produced with a Cs sputter source and accelerated to 300 keV beam energy, resulting in an ion-beam velocity of 0.66 a.u. The ion beam energy corresponds to a quasi-free electron beam energy of 5.9 eV. The ion beam is stored for 30 s after each injection and crossed with a neutral beam of argon atoms from a supersonic gas jet with 0.68 mm diameter. The recoil ions and electrons are extracted by a uniform 1.96 V/cm electric field. The electrons are restricted to a cyclotron path by a 4.2 Gauss magnetic field, resulting in a maximal electron momentum acceptance of about 1.5 a.u. To select electron-loss events, coincident hits of the electron and the neutral detector are required. To avoid artifacts from the detector efficiency only the first detected electron of each event is considered. In section 4.3, an additional anti-coincidence for recoil ion hits is set to suppress random coincidences with target

Table 4.1: Overview of the parameters for $Si^- + Ar$.

ion	Si^- from Cs sputter source
electron affinity of Si^-	1.39 eV [61]
ion beam energy	300 keV (0.66 a.u. velocity)
average quasi-free electron energy	5.9 eV
storage time	30 s
long. momentum spread	$\approx 1 \times 10^{-4}$ (estimated)
particles in the ring	unknown, prob. $\approx 10^8$
target	Ar from supersonic gas jet
jet diameter	≈ 0.68 mm
Argon ionization potential	15.76 eV [39]
resolution	about 0.1 a.u. (from zero peak)
	about 0.06 a.u. (calc from jet width)
electric extraction field	1.96 V/cm
magnetic field	4.2 Gauss (from cyclotron freq.)
max electron mom. acceptance	about 1.5 a.u.

ionization. For section 4.4, a triple coincidence of electron, recoil ion and neutral is required to select electron loss with simultaneous target ionization.

As described in section 2.7, the x axis position of the electron-hit position on the electron detector and the x axis position of the recoil ion hit position on the ion detector was corrected with the neutral detector x position to reduce the effective source volume in x direction.

4.3 Electron Loss Results

The results of this section were already published by Schulz el al. [63]. In Schulz et al. triple differential momentum distributions for electron detachment from the collisions of 30 and 300 keV beams of Si^- and C^- interacting with He, Ar and N_2 targets are described. Only the $Si^- + Ar$ collision is presented here, the additional collision systems discussed in [63] were omitted for brevity.

The ion-beam energy corresponds to a quasi-free electron beam energy of 5.9 eV. Since in the quasi-free electron model the projectile electron scatters elastically off the neutral Ar target a peak at 5.9 eV electron energy for the detached electron is expected.

Fig. 4.5 shows the energy spectrum of the ejected electron (blue line for electron loss), apart from the peak at zero there is a peak at about 7.5 eV (and not 5.9 eV). It is unlikely that this difference is a systematic error, since for the collision system $Si^- + He$ the same experiment peaks at about 5 eV [63].

Fig. 4.3 shows the triple differential electron momentum distribution ($d^3\sigma/d\mathbf{p^3}$)

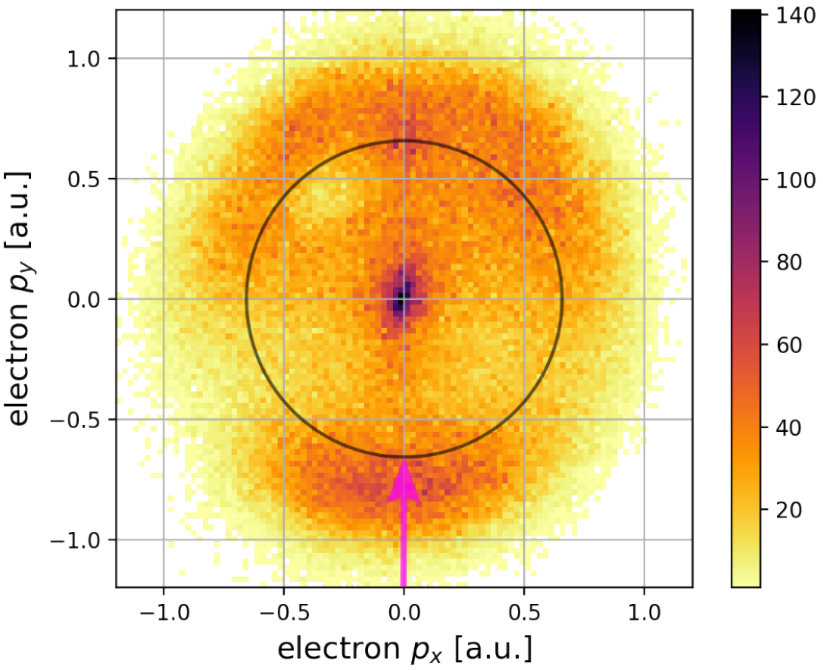

Figure 4.3: Si^- beam with 300 keV beam energy on Ar target. The black circle marks the expected quasi free electron momentum of 0.66 a.u., with anti-coincidence on recoil ion. $p_z = 0 \pm 0.05$ a.u. The spot in the upper left side at $p_x = 0.3$ a.u., $p_y = 0.5$ a.u. is due to a detector inefficiency. The magenta arrow indicates the ion beam direction.

in the detector plane ($p_z = 0 \pm 0.05$ a.u.) with respect to p_x and p_y with a coincidence condition on neutral projectile, electron and a anti-condition on recoil ion hits. The anti-condition on recoil ion hits suppress the contribution by target ionization (target ionization will be discussed in section 4.4), but since the ion detector efficiency is only around 50% (cf. section 2.3.2) there will still be some electrons from target ionization present in the data. The black circle in Fig. 4.3 indicates the velocity of the quasi-free electron of 0.66 a.u. As expected, at the circle a ring with clear lobes of backwards and forward scattering scattering can be seen. The lobe in forward direction is broader and seems to have two side lobes at around $\pm 40°$ relative to beam direction. The zero momentum electron in the center of Fig. 4.3 are attributed to come from target ionization and will be discussed in the next section. The region of reduced intensity at $p_x = 0.3$ a.u., $p_y = 0.5$ a.u. is due to detector imperfections.

In Fig. 4.4 the angular distribution of the differential cross section for electron emission from electron loss is compared with a theoretical calculation of the scattering angle of a free electron with 6 eV on an Argon target from [58] (described in section 4.1.1). To avoid a bias by the detector inefficiency at $p_{x/y} = (-0.3, 0.5)$ a.u. only points with $p_x \geq 0$ a.u. are accepted for the comparison plot. To further reduce the influence of simultaneous target ionization events the condition $0.56 \text{ a.u.} < \sqrt{p_x^2 + p_y^2} < 0.9 \text{ a.u.}$ is applied (in addition to the anti-coincidence condition on recoil-ion hits) to only select electrons scattered around 0.66 a.u. As will be discussed in the next section, electron loss with simultaneous target ionization leads to a momentum distribution sharply centered around zero. The comparison suggest a similar shape as for free electron scattering in Fedus et al. [58], but the angular position of the side lobe is farther into forward direction (around 40° instead of 75°).

This shows that the simple quasi-free electron model is not sufficient to describe the collision process fully. This gets more apparent when looking at electron loss with simultaneous target ionization.

4.4 Electron Loss and Simultaneous Target Ionization Results

The results in this section are soon to be published in [64] (submitted). In the paper the focus is slightly different leading to minor discrepancies between the presented values.

To select only electron loss with simultaneous target ionization a triple coincidence of neutral projectile, electron **and** recoil ion hit is demanded.

Fig. 4.5 shows the energy spectrum of the ejected electron in blue for electron loss without target ionization and in orange with target ionization. The beam energy of a quasi-free electron beam with 0.66 a.u. velocity is marked by the red line. Since in the uncorrelated process electron loss and target ionization are independent, the

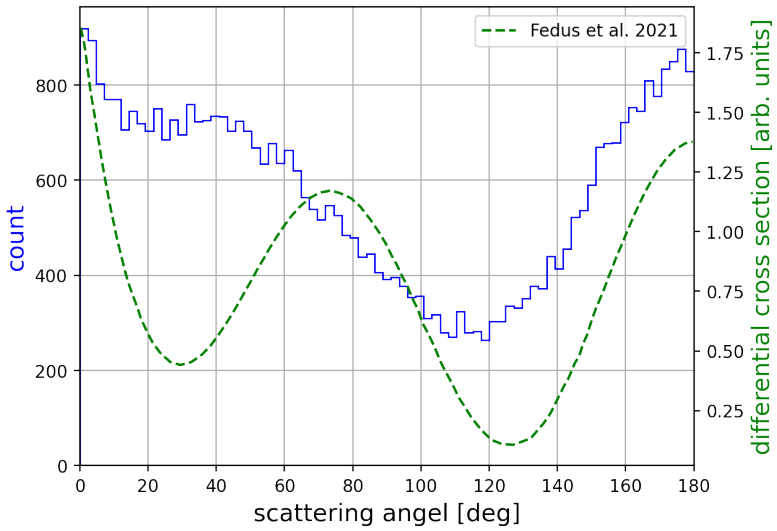

Figure 4.4: Comparison of electron scattering angle (blue line) with theory from Fedus et al. [58] (green dashed line) with condition $p_z = 0 \pm 0.05\,\text{a.u.}$ and $p_x \geq 0\,\text{a.u.}$ (to avoid bias from detector inefficiency spot on negative p_x side) and $0.56\,\text{a.u.} < \sqrt{p_x^2 + p_y^2} < 0.9\,\text{a.u.}$ to only select electrons scattered around $0.66\,\text{a.u.}$

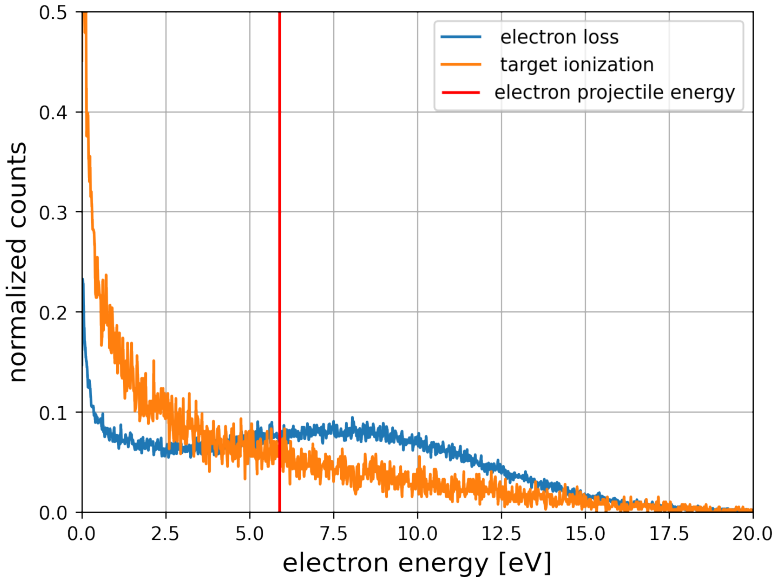

Figure 4.5: Energy of the detached electron for Si^- + Ar. The blue line selects electron loss from the projectile, the orange line selects electron loss with simultaneous target ionization. Both lines are normalized individually to make comparison of features easier.

signatures of both processes should be present, if this process is significant. Therefore one would expect that the energy of the electron has one peak centered at zero (for the electron ejected from the target) and one peak centered at the energy the projectile electrons, which are moving at relative to the detector (5.9 eV here). For the correlated process the electrons would emerge with almost zero energy, since all kinetic energy is needed to reach the ionization threshold. In Fig. 4.5 no peak around 5.9 eV is visible with target ionization (in clear contrast to electron loss where a peak is visible). The strong peak at zero could hide the peak at 5.9 eV, but for the uncorrelated process the binary encounter ring is expected in the differential image.

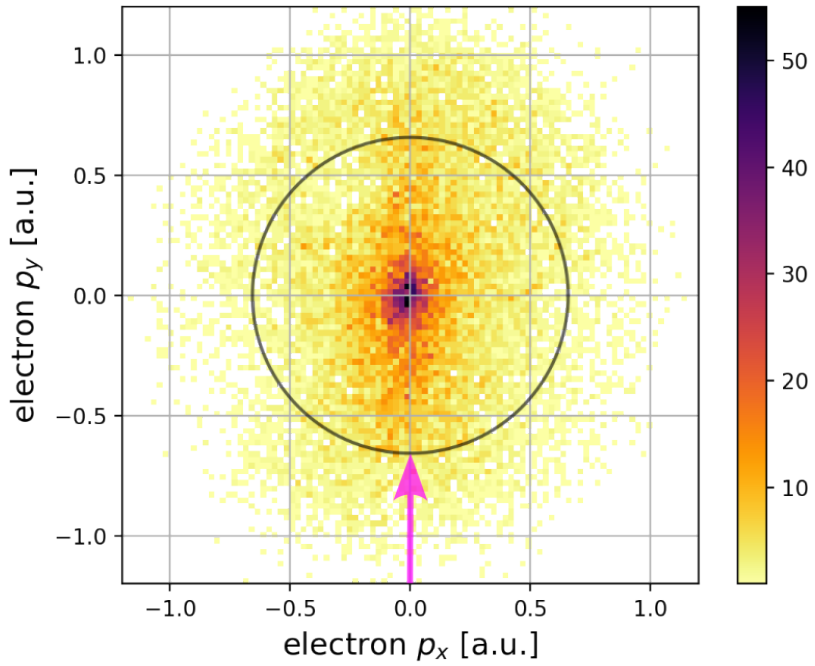

Figure 4.6: Si^- beam with 300 keV beam energy on Ar target. The black circle marks the expected quasi free electron momentum of 0.66 a.u., with coincidence on recoil ion. $p_z = 0 \pm 0.05$ a.u. The magenta arrow indicates the ion beam direction.

Fig. 4.6 shows the triple differential electron momentum distribution $\mathrm{d}^3\sigma/\mathrm{d}\mathbf{p}^3$ in the detector plane ($p_z = 0 \pm 0.05$ a.u.) with respect to p_x and p_y. There is only one spot in the center at zero electron momentum visible. Apart from a small forward/backwards asymmetry, no ring or forward/backwards scattering structure is visible at or near the black ring indicating the 0.66 a.u. momentum of the quasi-free electron. Therefore the uncorrelated process is negligible here and the interaction is dominated by the first-order projectile electron - target electron interaction.

Fig. 4.7 shows the ion - neutral projectile coincidence time. Since the neutral

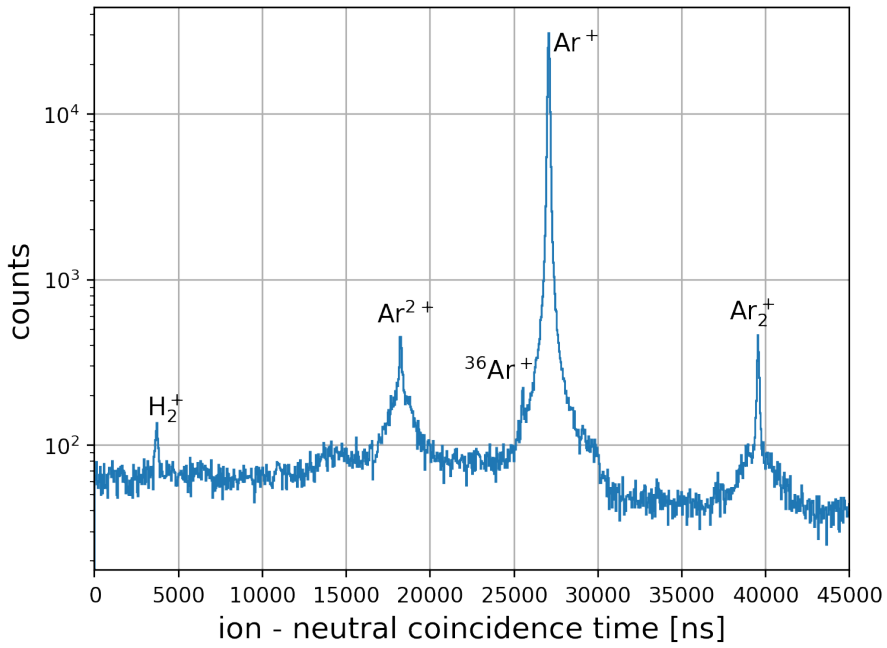

Figure 4.7: Ion - neutral coincidence time for Si^- beam with 300 keV beam energy on Ar target. Identified ion species are marked. Note: Since this is the coincidence time difference, the zero point is arbitrary.

flight time is nearly constants, the time-of-flight of the recoil ion is directly reflected by the coincidence time, see section 2.3.2). The small peak on the left at about 4 us is due to ionization of hydrogen (from the residual gas in the CSR). There is a large peak attributed to Ar^+ and two smaller peaks to the left and right of the Ar^+ peak attributed to Ar^{2+} and $Ar_2{}^+$. The small peak at 25.5 us, which is overlapping the edge of the Ar^+ peak is due to $^{36}Ar^+$ (natural abundance 0.33 % [54]). Tab. 4.2 shows a summary of peak heights and their strengths relative to background.

4.4.1 Electron Loss - Target Ionization Cross-Section Ratio

With the additional condition on the recoil ion time-of-flight the relative cross sections of electron loss with and without target ionization can be estimated, if the recoil ion detector efficiency ϵ_{rec} is known, by the peak height of the electron - neutral projectile coincidence time spectra. Tab. 4.3 summarizes the different peak heights and compares them to each other.

With the electron loss as the base level, simultaneous target ionization has around 10.4 % of the loss counts, which is surprisingly large. Even the double target ionization has 0.53 % of the loss counts or about 5.2 % of the single target ionization counts. Also target ionization with argon dimers $Ar_2{}^+$ has around 0.5 % of the

Table 4.2: Overview of the peak heights and their relative strengths in ion TOF spectrum.

	counts	rel. to background
background level	85	1
H_2^+ (residual gas)	139	1.6
Ar^+	17555	206
Ar^{2+}	469	5.5
Ar_2^+	453	5.3
$^{36}Ar^+$	220	2.5

Table 4.3: Overview of the electron branching rations for target ionization.

	counts	rel. to loss	rel. to Ar^+
only electron loss	48421	-	-
Ar^+	5014	10.4 %	-
Ar^{2+}	259	0.53 %	5.2 %
Ar_2^+	242	0.5 %	4.8 %

counts of electron loss.

The ratio between the cross sections for electron loss and electron loss with simultaneous target ionization can be obtained by

$$N_{\text{loss}} = \sigma_{\text{loss}}\epsilon_{\text{el}}\epsilon_{\text{p}} \tag{4.2}$$

$$N_{\text{ti}} = \sigma_{\text{ti}}2\epsilon_{\text{el}}(1-\epsilon_{\text{el}})\epsilon_{\text{p}}\epsilon_{\text{rec}} \tag{4.3}$$

$$\Rightarrow \frac{\sigma_{\text{ti}}}{\sigma_{\text{loss}}} = \frac{\frac{N_{\text{ti}}}{N_{\text{loss}}}}{\epsilon_{\text{rec}}2(1-\epsilon_{\text{el}})} \tag{4.4}$$

with σ_{loss} the cross section for electron loss/detachment, σ_{ti} electron loss with simultaneous target ionization, $N_{\text{loss}}, N_{\text{ti}}$ the corresponding count rates and $\epsilon_{\text{rec}}, \epsilon_{\text{el}}, \epsilon_{\text{p}}$ the detector efficiencies of the recoil ion, electron and neutral projectile detector, respectively. The factor $2\epsilon_{\text{el}}$ is the probability to detect exactly one out of the two ejected electrons.

Since the electron and ion detector are identical in construction, their efficiencies are expected to be the same. The detector efficiency $\epsilon_{\text{rec}} = \epsilon_{\text{el}} \approx 0.3509$ is assumed from the transmission of the grids and the MCP open-area-ratio, see section 2.3.2. The influence of the detector efficiency on the discussion is small, since the factor $(\epsilon_{\text{rec}}2(1-\epsilon_{\text{el}}))^{-1}$ is almost constant between 0.3 and 0.7, see Fig. 4.8.
From Eq. (4.4) and the values from Tab. 4.3 a cross section ratio of $\sigma_{\text{ti}}/\sigma_{\text{loss}} = 22.7\,\%$ is calculated.

For comparison, in the following, the cross section ratio in the quasi-free electron model is estimated. According to [56] the total detachment cross section for Si^- +

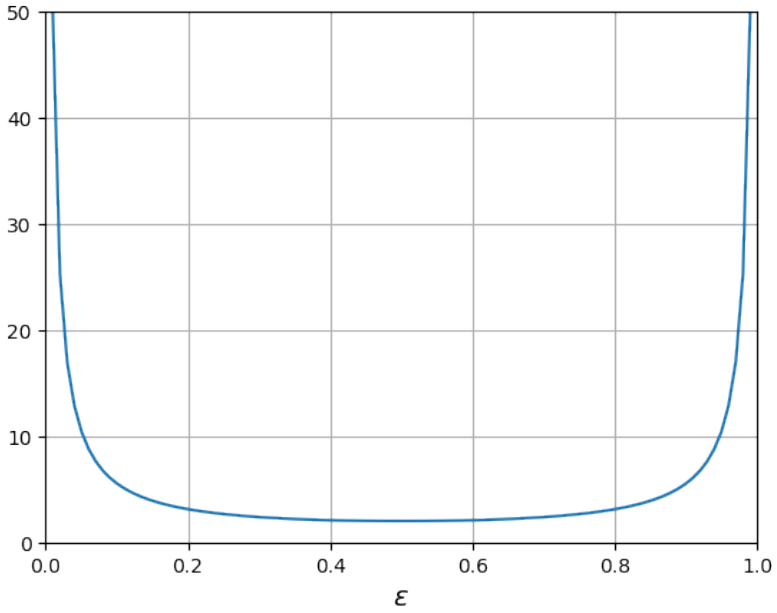

Figure 4.8: The factor $(\epsilon_{\text{rec}} 2(1-\epsilon_{\text{el}}))^{-1}$ as a function of ϵ. The factor is almost constant between 0.3 and 0.7.

Ar with a velocity $v \approx 0.66$ a.u. is about $2 \times 10^{-15}\,\text{cm}^2$. According to [65] Fig. 111 the target ionization cross section for free electron impact on Ar is zero at threshold and rises to a maximum of about $4 \times 10^{-16}\,\text{cm}^2$ around 100 eV. Only about 16 % of the quasi-free electrons from a 300 keV Si^- beam have a high enough momentum in the bound state to reach the kinetic energy threshold (see section 4.1.2); of these electrons the weighted average kinetic energy is about 23.9 eV. The ionization cross section for free electron impact on argon with ≈ 20 eV electrons is about $5 \times 10^{-17}\,\text{cm}^2$ according to [65] Fig. 111. Since only ≈ 16 % of the electron reach the threshold the cross section for the quasi-free electrons is then $0.16 \cdot 5 \times 10^{-17}\,\text{cm}^2 = 8 \times 10^{-18}\,\text{cm}^2$. All 5 outer electrons of Si^- can act as quasi-free electrons interacting with the target, therefore the cross section $8 \times 10^{-18}\,\text{cm}^2$ needs to be multiplied by 5. The expected cross section for the correlated target ionization is therefore $4 \times 10^{-17}\,\text{cm}^2$ or about 2 % of the detachment cross section.

The expected correlated cross section for electron loss with simultaneous target ionization is therefore about a factor of 10 smaller than the measured value (measured cross section ratio of $\sigma_{\text{DI}}/\sigma_{\text{DE}} = 22.7\,\%$).

Electron Loss - Double Target Ionization Cross Section Ratio

It was surprising that the ion - neutral coincidence time shows a strong peak for double target ionization (see Fig. 4.7). Staying in the quasi-free electron picture,

the incident electron needs even more kinetic energy, since it needs to overcome the second ionization energy of argon (27.63 eV [39]). Only $\approx 1.05\,\%$ of the electrons reach the threshold velocity of $v_{\mathrm{t,dti}} = 1.13$ a.u. in the bound state to have a high enough kinetic energy. The weighted average kinetic energy of these electrons is 54.48 eV, with the threshold for electron impact double ionization of argon at just about 50 eV [65]. As above the cross section ratio between pure electron loss and electron loss with simultaneous double target ionization can be obtained by

$$N_{\mathrm{dti}} = \sigma_{\mathrm{dti}} 3 \epsilon_{\mathrm{el}} (1 - \epsilon_{\mathrm{el}})^2 \epsilon_{\mathrm{p}} \epsilon_{\mathtt{rec}} \tag{4.5}$$

$$\frac{\sigma_{\mathrm{dti}}}{\sigma_{\mathrm{loss}}} = \frac{\frac{N_{\mathrm{dti}}}{N_{\mathrm{loss}}}}{3 \epsilon_{\mathrm{rec}} (1 - \epsilon_{\mathrm{el}})^2} \tag{4.6}$$

with the index 'dti' denoting the double target ionization parameters and the detector efficiency $\epsilon_{\mathrm{rec}} = \epsilon_{\mathrm{el}} \approx 0.3509$, as above. With the values from Tab. 4.2, the ratio $\sigma_{\mathrm{dti}}/\sigma_{\mathrm{loss}} = 1.21\,\%$ is determined.

For comparison, the cross section for $\mathrm{Ar} + \mathrm{e}^- \longrightarrow \mathrm{Ar}^{2+} + 3\,\mathrm{e}^-$, electron impact double ionization of argon, is $\sigma_{\mathrm{impact}} = 1.9 \times 10^{-17}\,\mathrm{cm}^2$. Multiplying by the ratio of bound electrons reaching the energy threshold and the 5 available (quasi-free) outer electrons of Si^-, one obtains $\sigma_{\mathrm{impact}} \cdot 0.0104 \cdot 5 = 9.88 \times 10^{-19}\,\mathrm{cm}^2$ or $0.0494\,\%$ of the electron loss cross section, almost 1.5 orders of magnitude difference lower than the measured ratio.

In summary, for the collision Si^- + Ar the electron loss with simultaneous target ionization process was identified as a direct projectile electron - target electron interaction. The cross section ratio of electron loss to electron loss with target ionization is a factor of 10 higher than the ratio expected from literature cross sections, for double target ionization even about 1.5 orders of magnitude higher. The quasi-free electron model is insufficient to describe this process and a more detailed theoretical model is needed.

5 Electron Transfer

The collision of a singly charged ion with a neutral atom is a very basic interaction. This chapter looks into the electron transfer from a noble gas target to a singly charged projectile. Section 5.1 will introduce the kinematics of an electron transfer and the classical-over-the-barrier model. The experimental parameters relevant for this chapter are summarized in section 4.2. In Section 5.3 first the ion - neutral coincidence is looked at to determine the present ion species. Subsection 5.3.2 is comparing energy released by the ground state to ground state transition with the expected values. In subsection 5.3.3 the transfer into excited projectile states is compared to known lines from NIST [39], for argon target also target transfer excitation is seen. Subsection 5.3.4 identifies the electron transfer into metastable projectile states by a lifetime measurement and subsection 5.3.5 looks into the scattering angle of the different lines.

5.1 Electron Transfer Theory

For slow collisions ($v < 1\,\text{a.u.}$) of positive ions with a neutral atom, the dominant process is electron transfer [66], when one or more electrons of the neutral collision partner (target) are captured by the ion (projectile). This is already investigated for ions of several species and in various charge states [67, 68]. Fig. 5.1 shows electron capture for the collision systems $Ar^+ + Ar$ (a) and $Ar^+ + He$ (b) schematically. One of the outer electrons of the target can be captured into the ground state or excited states in the projectile.

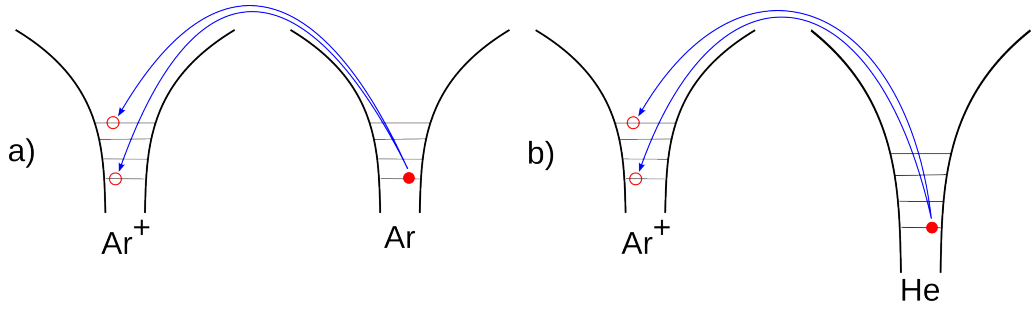

Figure 5.1: Schematic overview of the electron transfer between Ar (a) and He (b) and Ar^+ with either capture into the ground ground or in an excited state of the projectile.

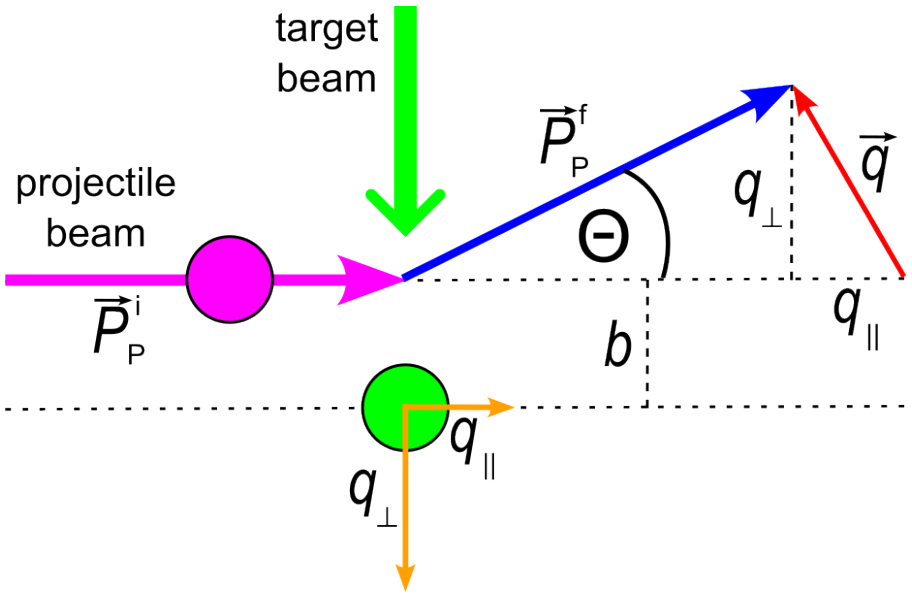

Figure 5.2: Schematic overview of a projectile with initial momentum $\vec{P}_P^i$ interacting with a target and transferring the momentum $\vec{q} = (q_\parallel, q_\perp)$. The projectile is deflected by the the angle Θ to the final momentum vector $\vec{P}_P^f$. b is the impact parameter.

5.1.1 Kinematics

This section is based on [28] page 6 to 8 with the slight deviation that the sign convention for the Q value definition is changed to $Q = E_{\text{bind}}^i - E_{\text{bind}}^f$. The equations are expressed in terms of atomic units by setting $\hbar = m_e = e = 4\pi\epsilon_0 = 1$, unless stated otherwise. Fig. 5.2 shows an overview of the momentum vectors for a projectile colliding with a target and transferring the momentum $\vec{q}$. The projectile has the initial momentum $\vec{P}_P^i$ and is scattered with the the angle Θ to the final momentum vector $\vec{P}_P^f$.

In general the kinetic energy of a particle is given by

$$E_{\text{kin}} = \frac{p^2}{2m} = \frac{mv^2}{2} \tag{5.1}$$

with p the momentum, m the mass and v the velocity of the particle. The momentum sum of the collision of projectile and target before and after collisions is given by

$$\vec{P}_P^i + \vec{P}_R^i = \vec{P}_P^f + \vec{P}_R^f + \sum_j \vec{P}_{ej}^f + \sum_l \vec{P}_{\gamma l}^f \tag{5.2}$$

with $\vec{P}_R^i, \vec{P}_R^f$ the initial and final momentum vectors of the target (the target is often called the 'recoil ion', since the momentum transfer leads to a recoil of the ion), $\vec{P}_e^f$

is the momentum of electrons ejected by the interaction and $\vec{P}_{\gamma}^{\,\mathrm{f}}$ is the momentum of emitted photons. For the discussion here the emission of photons is not relevant, since the relaxation of the electronic states by photo-emission happens typically on time scales of ns (see e.g. [69] for radiative lifetimes of excited ArII states, which are generally $\geq 3\,\mathrm{ns}$) and is therefore much slower than the interaction time in the collision, therefore $\vec{P}_{\gamma}^{\,\mathrm{f}} = 0$. Since the ion beam (projectile) is aligned with the y axis it follows that $\vec{y} \parallel \vec{P}_{\mathrm{P}}^{\,\mathrm{i}}$. For a target from a supersonic gas jet $\vec{P}_{\mathrm{R}}^{\,\mathrm{i}} \approx 0$ since $v_{\mathrm{gasjet}} \ll v_{\mathrm{projectile}}$ (Ar^+ beam with 30 keV has $v = 0.174\,\mathrm{a.u.}$ velocity, gas jet has thermal velocity $\approx 25\,\mathrm{meV}$ or $v = 0.00016\,\mathrm{a.u.}$ velocity), in addition the detector image can be shifted such that $\vec{P}_{\mathrm{R}}^{\,\mathrm{i}} = 0$ ($E_{\mathrm{R}}^{\mathrm{i}} = 0$). For electron transfer reaction no free electrons are expected, therefore $\vec{P}_{ej}^{\,\mathrm{f}} = 0 (\Rightarrow E_{ej}^{\mathrm{f}} = 0)$ and Eq. (5.2) simplifies to

$$\vec{P}_{\mathrm{P}}^{\,\mathrm{i}} = \vec{P}_{\mathrm{P}}^{\,\mathrm{f}} + \vec{P}_{\mathrm{R}}^{\,\mathrm{f}}. \tag{5.3}$$

The momentum transfer vector is defined as

$$\vec{q} = (q_{\perp}, q_{\parallel}) = \vec{P}_{\mathrm{R}}^{\,\mathrm{f}} = \vec{P}_{\mathrm{P}}^{\,\mathrm{i}} - \vec{P}_{\mathrm{P}}^{\,\mathrm{f}} \tag{5.4}$$

with the longitudinal component $q_{\parallel}$ along the ion beam/projectile direction and the transversal component $q_{\perp}$ orthogonal to the ion beam/projectile direction.

Before calculating the energy sum of the collision, consider that, in the general case for a collision between a projectile A^+ and a neutral target B, one or both collision partners can end up in an excited state. The reaction equation for energy transfer is therefore $\mathrm{A}^+ + \mathrm{B}^0 \longrightarrow \mathrm{A}^0/\mathrm{A}^{*0} + \mathrm{B}^+/\mathrm{B}^{*+}$. The energy contribution of each collision partner is separated into an internal energy E and an external/kinetic energy K. The index P denotes the projectile energies and the index R the energies of the target/recoil ion. The superscript i marks for before and f after the collision. The energy sum can then be written as

$$E_{\mathrm{P}}^{\mathrm{i}} + E_{\mathrm{R}}^{\mathrm{i}} + K_{\mathrm{P}}^{\mathrm{i}} = E_{\mathrm{P}}^{\mathrm{f}} + E_{\mathrm{P}}^{\mathrm{f}} + K_{\mathrm{P}}^{\mathrm{f}} + K_{\mathrm{R}}^{\mathrm{f}}. \tag{5.5}$$

For the final kinetic energy of the projectile, $K_{\mathrm{P}}^{\mathrm{f}} \approx K_{\mathrm{P}}^{\mathrm{i}}$ can be assumed, since $K_{\mathrm{P}} \gg K_{\mathrm{R}}$. E.g. for an ion beam energy of 30 keV, the measured transfer to the target is normally $\leq 30\,\mathrm{eV}$. Less than 1 % of the ion beam energy.

The so-called Q value is defined as $Q = E_{\mathrm{bind}}^{\mathrm{i}} - E_{\mathrm{bind}}^{\mathrm{f}}$ ([28] uses the opposite sign convention here) with E_{bind} the total binding energy/total internal energy of projectile and target. For $Q < 0$ the reaction is endothermic and absorbs kinetic energy from the projectile-target system and for $Q > 0$ the reaction is exothermic and releases kinetic energy.

If $K_\mathrm{P} \gg K_\mathrm{R}$

$$Q = E_\mathrm{P}^\mathrm{i} + E_\mathrm{R}^\mathrm{i} - (E_\mathrm{P}^\mathrm{f} + E_\mathrm{R}^\mathrm{f}) \tag{5.6}$$

$$= K_\mathrm{P}^\mathrm{i} - (\underbrace{K_\mathrm{P}^\mathrm{f}}_{\approx K_\mathrm{P}^\mathrm{i}} + K_\mathrm{R}^\mathrm{f}) \approx -K_\mathrm{R}^\mathrm{f} \tag{5.7}$$

follows and therefore only negative Q values are expected.

To calculate the Q value for electron transfer from an experimentally accessible parameter consider the total energy parallel to the projectile beam direction

$$\mathcal{E}_\parallel = -Q + K_\mathrm{el} \tag{5.8}$$

with the kinetic energy K_el of the electron transferred from the target to the projectile. By adding $\mathcal{E}_\parallel = E_\mathrm{P}^\mathrm{i} - E_\mathrm{P}^\mathrm{f}$ and the kinetic energy definition, and then using $(a-b)(a+b) = a^2 - b^2$ follows[1]

$$\frac{(P_{\mathrm{P}\parallel}^\mathrm{i})^2 - (P_{\mathrm{P}\parallel}^\mathrm{f})^2}{2m} = \frac{(P_{\mathrm{P}\parallel}^\mathrm{i} - P_{\mathrm{P}\parallel}^\mathrm{f})(P_{\mathrm{P}\parallel}^\mathrm{i} + P_{\mathrm{P}\parallel}^\mathrm{f})}{2m} = -Q + \frac{1}{2} v_\mathrm{P}^2 m_\mathrm{e}. \tag{5.9}$$

Apply the transverse momentum $q_\parallel = P_{\mathrm{P}\parallel}^\mathrm{i} - P_{\mathrm{P}\parallel}^\mathrm{f}$ and, for $K_\mathrm{P} \gg Q$, the approximation $P_{\mathrm{P}\parallel}^\mathrm{i} \approx P_{\mathrm{P}\parallel}^\mathrm{f}$ to simplify the above equation to

$$q_\parallel v_\mathrm{P} = -Q + \frac{1}{2} v_\mathrm{P}^2 m_\mathrm{e} \tag{5.10}$$

with v_P the initial velocity of the projectile. And with $q_\parallel = P_{\mathrm{P}\parallel}^\mathrm{i} - P_{\mathrm{P}\parallel}^\mathrm{f} = P_{\mathrm{R}\parallel}^\mathrm{f} + v_\mathrm{P}$ follows

$$P_{\mathrm{R}\parallel}^\mathrm{f} + v_\mathrm{P} = \frac{-Q}{v_\mathrm{P}} + \frac{1}{2} v_\mathrm{P} m_\mathrm{e} \tag{5.11}$$

$$\Rightarrow \quad -Q = P_{\mathrm{R}\parallel}^\mathrm{f} v_\mathrm{P} + \frac{1}{2} v_\mathrm{P}^2 m_\mathrm{e}. \tag{5.12}$$

For an Ar^+ beam with 30 keV the kinetic energy of the transferred electron is $\frac{1}{2} v_\mathrm{P}^2 m_\mathrm{e} = 0.41\,\mathrm{eV}$. In many cases this is negligible, since the Q value is dominated by the binding energy difference between initial and final state.

Scattering Angle

The scattering angle Θ is determined by the transversal momentum $q_\perp$ transferred in the collision. It follows

$$\Theta = \arctan\left(\frac{q_\perp}{P_\mathrm{P}^\mathrm{i}}\right) \tag{5.13}$$

with $P_\mathrm{P}^\mathrm{i} \approx P_\mathrm{P}^\mathrm{f}$.

[1] In atomic units the electron mass $m_\mathrm{e} = 1$, but it was added here for clarity.

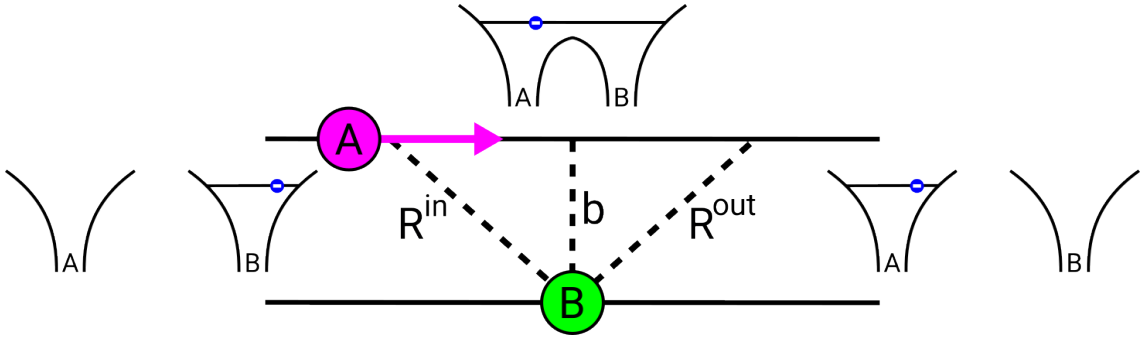

Figure 5.3: Schematic overview of a interaction in the CoB model with only one active electron. The projectile A moves in and the core potentials of projectile A and target B merge and the weakly bound electron can move in the combined quasi-molecular potential. As the inter-particle distance increases, the potential barrier increases again and the electron is captured by the projectile.

5.1.2 Classical-over-the-Barrier Model

The classical over-the-barrier (CoB) model describes the electron transfer of a n-fold charged projectile A^{n+} capturing r electrons from a target B in a collision $\mathrm{A}^{n+} + \mathrm{B} \longrightarrow \mathrm{A}^{(n-r)+} + \mathrm{B}^{r+}$. The argumentation follows Niehaus [70] in a simplified way to focus on single electron transfer, see also the thesis of S. Knoop [71] or Ina Blank [72] for an in-depth summary.

The collision is separated in two parts, a way-in and a way-out. Fig. 5.3 shows a schematic overview of the interaction between projectile A and target B. On the way-in the inter-particle distance R is decreasing. The core potentials of the projectile A and target B overlap leading to a lowering of the barrier between the two cores. For a low-enough barrier, weakly bound electrons will start to move in the combined potential, becoming quasi-molecular. For higher collisions energies, the minimal inter-particle distance becomes smaller and the barrier will be lower, leading stronger bound electrons becoming quasi-molecular. On the way-out the inter-particle distance R is increasing and the electrons are (re)captured by either the target B or the projectile A.

The capture radius on the way-in for the tth electron is given by

$$R_t^{\mathrm{in}} = \left(n \left(\frac{1}{\alpha_t} - 1 \right) + \frac{t}{1-\alpha_t} \right) \frac{1}{I_t} \tag{5.14}$$

$$\alpha_t = \frac{1}{1+\sqrt{\frac{t}{n}}} \tag{5.15}$$

with I_t the ionization energy for the tth electron. The (re)capture radius on the

way-out is given by

$$R^{\text{out}} = \left(\frac{n - r_t}{\beta_t} + \frac{t + r_t}{1 - \beta_t} \right) \frac{1}{I_t + \frac{n}{R_t^{\text{in}}}} \tag{5.16}$$

$$\beta_t = \frac{1}{1 + \sqrt{\frac{t+r_t}{n-r_t}}} \tag{5.17}$$

with r_t the number of electrons with index larger than t already captured by A at smaller inter-particle separation. Since single electron transfer is investigated here, usually $r_t = 0$. The binding energy of the tth electron for capture by A (projectile) is then

$$E_{\text{A}} = I_t + \frac{n}{R_t^{\text{in}}} - \frac{t + r_t}{R_t^{\text{out}}} \tag{5.18}$$

and for capture by B (target)

$$E_{\text{B}} = I_t + \frac{n}{R_t^{\text{in}}} - \frac{n - r_t}{R_t^{\text{out}}}. \tag{5.19}$$

The Q value for one electron capture of the projectile A is

$$Q_1^{\text{CoB}} = I_1 - E_{\text{B}}. \tag{5.20}$$

Since for only one active electron $R^{\text{in}} = R^{\text{out}} \Rightarrow Q_1^{\text{CoB}} = 0$.

To estimate the accessible Q values the so-called reaction window

$$W(Q) = \frac{1}{\sqrt{\pi}\Delta Q} \exp\left(- \left(\frac{Q - Q^{\text{CBM}}}{\Delta Q} \right)^2 \right) \tag{5.21}$$

can be calculated. The reaction window is defined as a Gaussian distribution around the predicted Q^{CBM}. The width ΔQ of the reaction window is given by the quadratic sum of the energy uncertainty

$$\mathrm{d}E = \sqrt{\left(\frac{\sqrt{n} + \sqrt{t}}{R_{\text{in}}} \right)^2 v_{\text{rad},t}^{\text{in}} + \left(\sqrt{n - c} + \frac{\sqrt{i + c}}{R_{\text{out}}} \right)^2 v_{\text{rad},t}^{\text{out}}} \tag{5.22}$$

with $v_{\text{rad},t}^{\text{in}}, v_{\text{rad},t}^{\text{out}}$ the radial velocities on the way-in and way-out. If the active electron t is the last one to become quasi-molecular the radial velocity on the way-in is

$$v_{\text{rad},t}^{\text{in}} = \frac{2}{3} v_{\text{p}} \sqrt{1 - \frac{R_{\text{in},t+1}}{R_{\text{in},t}}} \tag{5.23}$$

and on the way-out

$$v_{\text{rad},t}^{\text{out}} = \frac{2}{3} v_{\text{p}} \sqrt{1 - \frac{R_{\text{in},t+1}}{R_{\text{out},t}}}. \tag{5.24}$$

Fig. 5.4 shows the calculated reaction window from the CoB model and the corresponding states for the single electron capture into the Ar^+ projectile with $v_P = 0.17$ a.u. and He, Ne and Ar targets. The vertical energy levels mark the expected differences in binding energy for the electron capture by the projectile (values from [39]). For all targets, the ground state transition is in the reaction window, but the transition probability for the exited projectile states is much lower. The transition from the ground state to the ground state is therefore expected to have the highest intensity.

Transversal Momentum with the CoB Model

The transversal momentum can be estimated by the component of the Coulomb force acting perpendicular to the projectile direction of flight integrated over time for a constant projectile velocity v_P. It follows that in general smaller impact parameters b lead to larger scattering angles, since the traversal Coulomb force between the collision partners is larger. In the CoB model the transversal momentum can be

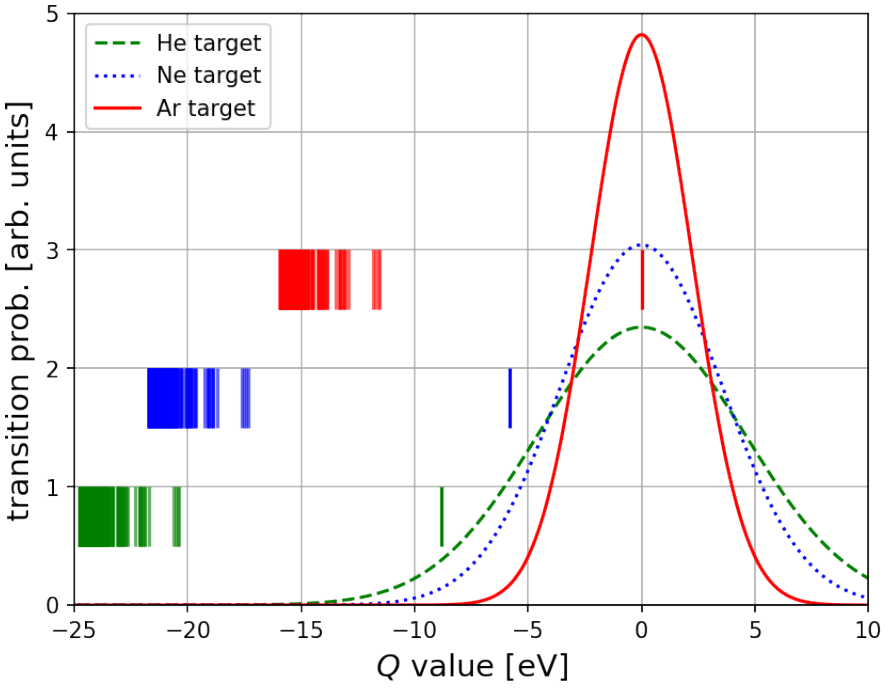

Figure 5.4: Reaction window from the CoB model for He, Ne and Ar targets with the corresponding states for the single electron capture into the Ar^+ projectile marked by the vertical lines. Energy levels from [39].

calculated by

$$p_\perp(b) = \frac{1}{v_\mathrm{p} b}\left(\sum_t \left[q\sqrt{1-(b/R_t^\mathrm{in})^2} + t\sqrt{1-(b/R_t^\mathrm{in})^2}\right] + (q-r)r\right) \tag{5.25}$$

$$= \frac{1}{v_\mathrm{p} b}\left((q-1)\sqrt{1-(b/R_1)^2} + (q-1)\right) \tag{5.26}$$

with the second line simplified for the one-electron capture of the least bound target electron with $t = 1$ and $R_1^\mathrm{out} = R_1^\mathrm{in} = R_1$. The momentum differential

$$\frac{\mathrm{d}\sigma}{\mathrm{d}p_\perp} = \frac{\mathrm{d}\sigma}{\mathrm{d}b}\left|\frac{\mathrm{d}b}{\mathrm{d}p_\perp}\right| = 2\pi b\left|\frac{\mathrm{d}b}{\mathrm{d}p_\perp}\right| \tag{5.27}$$

with $\sigma = \pi b^2$ gives the transverse momentum intensity distribution. One gets $\mathrm{d}p_\perp/\mathrm{d}b$ from Eq. (5.26) and can then calculate the transverse momentum distribution. Fig. 5.5 shows the transverse momentum distribution and the corresponding scattering angle distribution from the CoB model for a $v_\mathrm{P} = 0.17\,\mathrm{a.u.}$ beam for He, Ne and Ar targets. The lighter targets, with a higher electron binding energy, have a higher mean scattering angle.

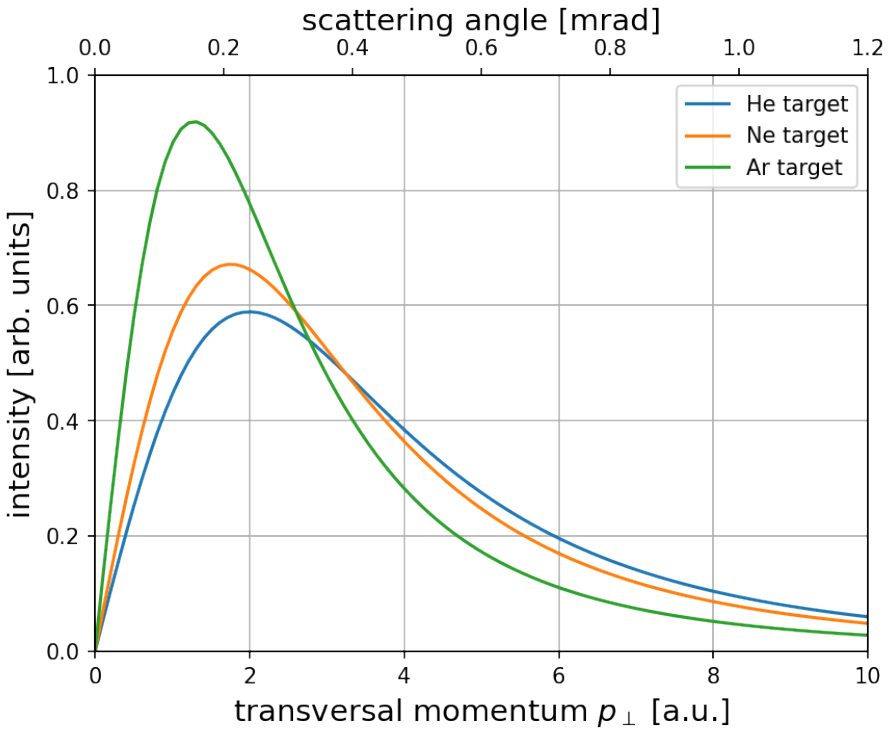

Figure 5.5: Scattering angle/transversal momentum from CoB model for He, Ne and Ar target with $v_\mathrm{P} = 0.17\,\mathrm{a.u.}$ projectile velocity.

Table 5.1: Metastable states and lifetimes of Ar^+ according to [81]. Energy level relative to ArII ground state.

state	energy level	expected lifetime
$3s^2 3p^4(3P)3d^4F_{9/2}$	17.63 eV	4.35 s, measured 4.9 ± 0.7 s
$3s^2 3p^4(3P)3d^4F_{7/2}$	17.69 eV	4.45 s
$3s^2 3p^4(3P)3d^2F_{9/2}$	18.50 eV	1.25 s
$3s^2 3p^4(1D)3d^2G_{7/2}$	19.12 eV	6.10 s
$3s^2 3p^4(1D)3d^2G_{9/2}$	19.12 eV	4.90 s

5.1.3 Potential-Energy Curve

Another way to describe the collision would be in terms of the adiabatic potential energy curves (PEC) of the quasi-molecule. The PEC of a molecule gives the electronic states in dependence on the inter-atomic distance. A quantum mechanical or semi-classical treatment of the electron transfer, like in [73] for the $Ne^+ + Rb$ charge-exchange collision, would need to determine the PEC for the relevant states in the interaction. Miteva et al. [74] did calculate PES for selected states of ionic argon dimers to study inter-atomic Columbic decay, with the Ar^+ in excited states. But, the determination of the PES for the Ar^+ collision with He, Ne and Ar is beyond the scope of this thesis.

5.1.4 Metastable States in Ar^+

Since, in this experiment, the Ar^+ beam is produced by a Penning source, initially many excited states will be populated and quickly de-excite to the ground state again. Only long-lived metastable states will reach the CSR.

The metastable states of argon are subject of many experiments. There were e.g. studies with metastable Ar^-, which found a lifetime in the 260 to 350 ns range [75, 76]. Yang et al. [77] investigated the lifetimes of selected metastable levels for $Ar^{q+}$with $q = 2, 3, 9, 10$ in an electrostatic trap and found lifetimes in the 10's to 100's of ms range, but did not look into Ar^+. Lepère et al. [68] discussed the production of metastable $Ar_2{}^+$ ions in a linear ion trap. And neutral metastable Ar ($1s_5$ and $1s_3$) was investigated by laser absorption spectroscopy [78, 79]. Müller et al. [80] studied charge-changing interactions with Ar^{3+}, Ar^{2+} and Ar^+, and also look into metastable Ar^+, since the presence of metastable states can change the cross section for a second charge-changing interaction.

Schef et al. [81] calculated that there are five metastable states in positive Argon ions (see Tab. 5.1). They measured the lifetime of the metastable 3d $^4F_{9/2}$ state in positive Argon ions at the ion storage ring CRYRING and found the lifetime in agreement with their calculation. For metastable Ar^+, no literature could be found, investigating the charge transfer/electron capture process angularly resolved.

For the electron transfer process studied here, the direct electron capture into the lowest unoccupied state of the metastable Ar^+ seems most likely, since this is a first-order process. For argon target and the $^4F_{9/2}$ metastable state the reaction would be $Ar^{*+}(3s^2\,3p^4\,3d) + He^0(1s^2) \longrightarrow Ar^*(3s^2\,3p^5\,3d) + He^+(1s)$ with

$$Q = (\underbrace{15.74\,\text{eV} + 17.63\,\text{eV}}_{Ar^{*+}} + \underbrace{0\,\text{eV}}_{He^0}) - (\underbrace{13.85\,\text{eV}}_{Ar^*} + \underbrace{24.6\,\text{eV}}_{He^+}) = -5.07\,\text{eV}. \tag{5.28}$$

The Q value for the other metastable states and the neon target are calculated the same way.

5.2 Experimental Parameters: The Collision of Ar^+ with Ar, He and Ne Target

Table 5.2: Overview of the Ar^+ beam time parameters.

ion	Ar^+
ion beam energy	30 keV ($v = 0.174$ a.u. velocity)
long. momentum spread	$\approx 3 \times 10^{-4}$
particles in the ring	$\approx 10^8$
storage time	30 s
targets	Ar ($I_{Ar} = 15.76$ eV) [39]
	He ($I_{He} = 24.59$ eV) [39]
	Ne ($I_{Ne} = 21.56$ eV) [39]
jet diameter	≈ 0.5 mm
extraction field	0.78 V/cm
magnetic field	off (only earth magnetic field)
expected resolution	He: 0.11 a.u. (0.52 eV)
	Ne: 0.25 a.u. (1.18 eV)
	Ar: 0.35 a.u. (1.67 eV)

Tab. 5.2 shows an overview of the experimental parameters relevant in this section. The experimental setup is described in detail in chapter 2. The Ar^+ ions are produced by a small Penning ion source and accelerated to 30 eV beam energy, resulting in an ion-beam velocity of 0.174 a.u. The ion beam is crossed with a neutral noble gas target from the supersonic gas jet with ≈ 0.5 mm diameter. Argon, neon and helium are used as a target gases. The recoil ions are extracted by a 0.78 V/cm electric field and detected in coincidence with the neutralized projectile. No external magnetic field was applied, since no electron detection was necessary. For all events coincident recoil ions and neutral hits were required.

5.3 Electron Transfer Results

Fig. 5.6 shows the recoil ion momentum sphere projected on the ion detector plane for the argon target. Three distinct lines are visible. The maximum of the first line is centered on the coordinate-system origin in both x and y direction. This is done, since for $Ar^+ + Ar \longrightarrow Ar^0 + Ar^+$ the most intense line is expected to be the ground-state to ground-state electron transfer, since the transition probability is for the ground state highest according to the reaction window calculated in section 5.1.2. The offset in x direction between the ion beam incident position and the maximum of the lines is caused by the non-zero gas-jet velocity in forward direction and the initial target kinetic energy is shifted to zero momentum. The lines with higher p_y are then electron transfers into different (excited) states of argon, since $p_y \propto Q$ with kinetic energy of the ion being converted to internal energy of the active electron.

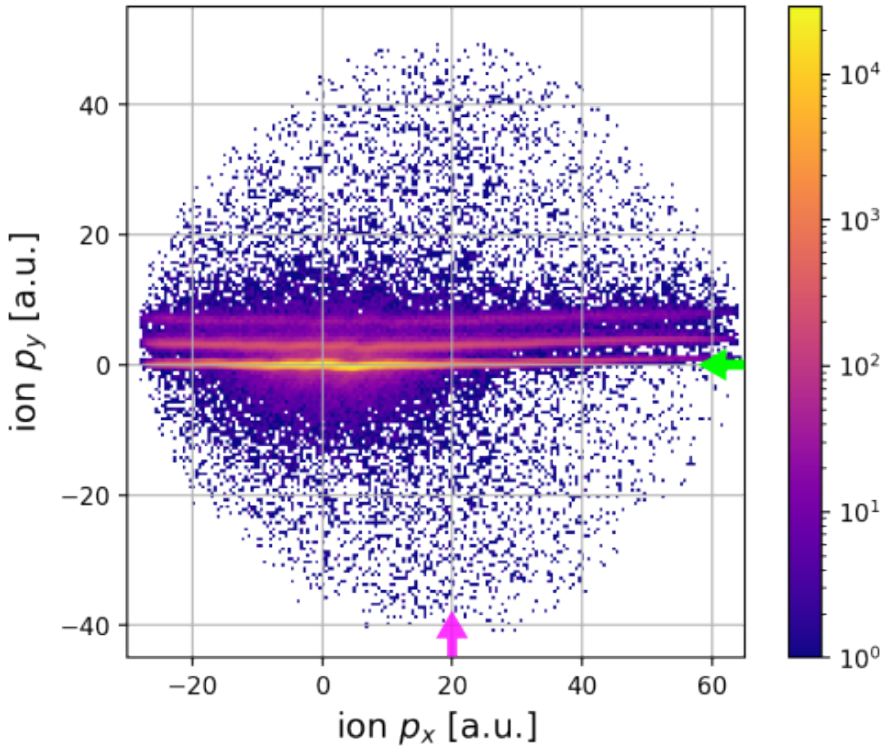

Figure 5.6: Recoil ion momentum sphere projected on ion detector plane for Ar^+ beam with 30 keV beam energy on Ar target. The magenta arrow marks the ion beam direction and the green arrow the gas jet direction. Note: The slight wobble in the lines (visible especially around the origin) is believed to be a detector artifact caused by cross talk in the delay line anode.

5.3.1 Ion - Neutral Coincidence Time

Fig. 5.7 shows the ion - neutral coincidence time for Ar^+ colliding with the different targets. Since the CSR is at cryogenic temperature, the main residual gas component is $H_2{}^+$. For all three targets a peak with the expected time-of-flight is well visible. For the helium target there are three other peaks in the spectrum. The peak at about 4 µs is from the helium ions with a sharp central peak and two shoulders, caused by the target ions acquiring transversal momentum in the collision. It is about one order of magnitude lower than the $H_2{}^+$ residual gas peak, but the separation is well enough to suppress the residual gas counts with a suitable time-of-flight condition. The two other peaks at about 18 µs and 28 µs are about two orders of magnitude lower than the $H_2{}^+$ peak. The peak at 18 µs could be either N^+ or O^+, since it is fairly broad. The peak at 28 µs fits best to $N_2{}^+$. Since the gas jet is produced from a high-purity helium gas bottle, these ions originate in the residual gas. For neon target the peak of the target gas is at least a factor of 2 higher than the $H_2{}^+$ background and both peaks are well separated. The target gas peak also has shoulders from the transversal momentum transfer. At about 23 µs, slightly to the right of the main Neon peak, also the ^{22}Ne isotope is visible (natural abundance $\approx 9.25\%$ [54]).
The target gas peak for argon has about two orders of magnitude more counts as the $H_2{}^+$ peak. Additionally, a second peak corresponding to argon dimers is visible at around 5.5 µs.

5.3.2 Check Energy Scaling

From the momentum parallel to the ion beam direction the Q value can be calculated as described in section 5.1.1. Since the ground state to ground state transition has the highest overlap in the reaction window (see Fig. 5.4), the most intense peak in the Q value spectrum is expected to be the ground state transition. This assumption can be used to check the energy scaling in y direction. Fig. 5.8 shows the Q value for all three targets. The difference between argon ionization energy and the targets ionization energy are marked with red lines. The most intense peak for $Ar^+ + Ar$ was used to establish the origin (peak was shifted to origin). The scaling is identical for the helium and neon target. The highest peaks for neon and helium target align with the respective ionization energy difference line. This confirms that the strongest peaks are the ground state to ground state transitions.

5.3.3 Electron Transfer to Excited States

Since the neutral target is produced in a supersonic gas jet and the first exited levels for argon, neon and helium are well above the thermal energy at room temperature of 25 meV, the neutral target will be in the electronic ground state before the collision.

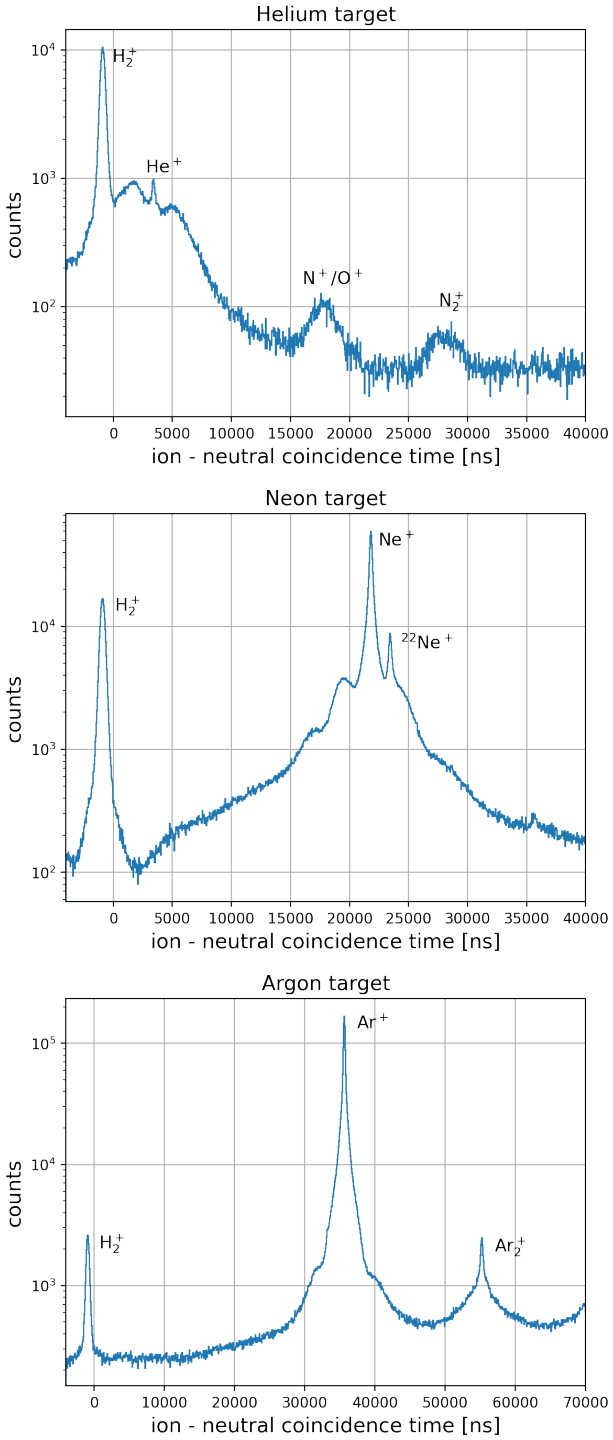

Figure 5.7: Ion - neutral coincidence time (ion tof with offset t_0) for 30 keV Ar^+ beam on He, Ne and Ar target. The peaks are marked with the ion species expected at this time-of-flight.

The ion beam will also be mostly in the ground state, since most exited states of the positive Argon ion are short-lived [69]. The transition involving the metastable states of Ar^+ mentioned in section 5.1.4 will be discussed in section 5.3.4. In the section above the strongest peak in the Q value spectrum was identified as the ground state to ground state transition. The other peaks are transitions into excited projectile states. The expected Q values can be calculated by the difference of initial and final state with the excited levels energies from the NIST database [39].

Fig. 5.9 shows the Q value spectrum (blue line) for argon target. There are three distinct peaks at 0 eV, about -12 eV and about -33 eV, respectively. The first peak at 0 eV with a FWHM[2] of 2.36 eV was already attributed to the ground state to ground state transition and used to calibrate the origin point of the energy scale (see section 5.3.2). The peaks at about -12 and -33 eV correspond to excited state transitions. For the peak at 12 eV the electron is captured into excited states in the projectile (red lines). It is unclear into which exact state the electron is captured, since the individual states overlap at this energy resolution.
To explain the peak at -33 eV an even higher energy difference between initial and final state is needed. This can only be explained by a process $Ar^+ + Ar \longrightarrow$

[2]Full Width Half Maximum

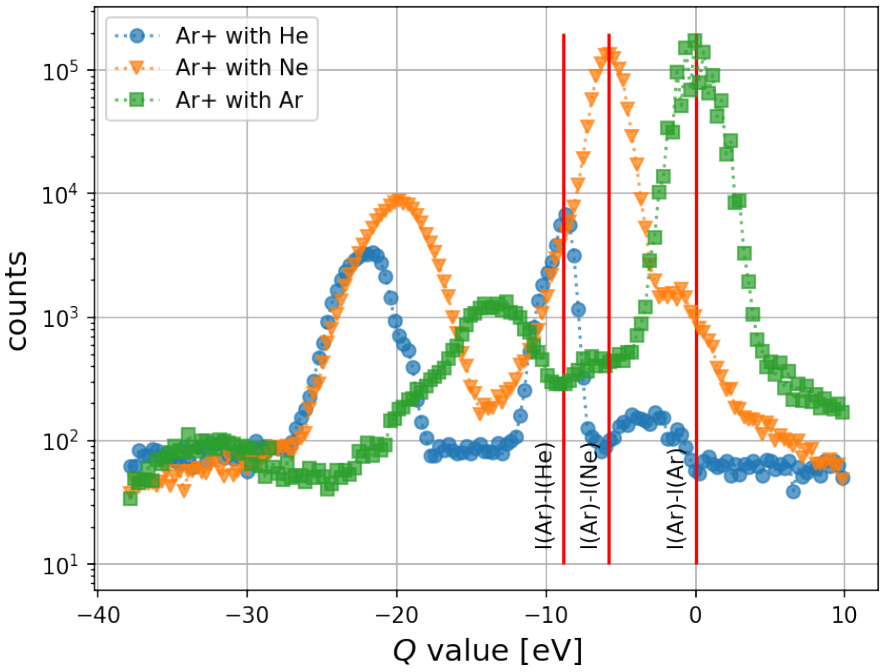

Figure 5.8: Q value for Ar^+ beam with 30 keV beam energy on Ar, He and Ne target. The red lines mark the ionization energy differences between the respective target and the argon ionization energy.

$Ar^* + Ar^{*+}$ were the target is also excited. The orange lines mark electron transfer with target transfer excitation to $s^2 3p^4(^3P)4s$ and the green lines for excitation to $s^2 3p^4(^1D)5s$.
Target excitation with transition into the projectile ground state seems to cause the long decline to the left of the peak at -12 eV (single orange and green lines at about -17 eV and -25 eV). The target excitation with transition into projectile excited states causes the third peak at -33 eV. Since the orange lines lie at the right edge of the -33 eV peak and the green lines at the left edge of the peak, the peak is probably caused by many different states of overlapping target excitations.

Fig. 5.10 shows the Q value spectrum with Helium and Neon target, respectively. For the helium target there are also three peaks visible. The highest peak, attributed to be the ground state to ground state transition, is at around -9 eV with a FWHM of 1.3 eV and matches the ionization energy difference between argon (projectile) and helium (target) well. The second highest peak is at around -23 eV and corresponds to electron transfer into excited projectile states. No target transfer excitation is visible (also no additional line in the 2D detector image). This is not surprising, since the first excited level of the helium ion is more than 40 eV above the ground state [39] and would therefore require a large conversion of kinetic to internal energy. The third visible peak is at around -3 eV and has the lowest intensity, more than

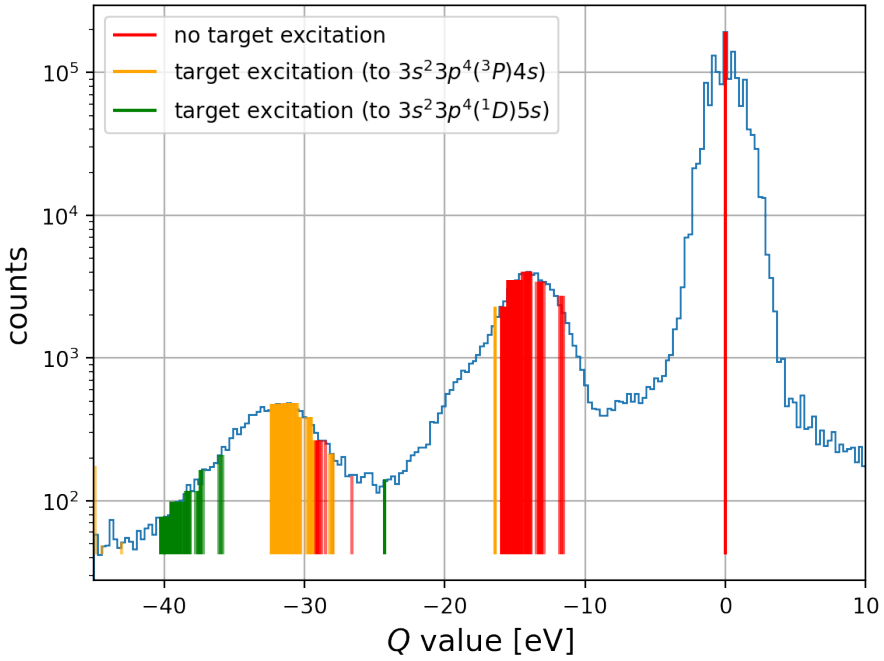

Figure 5.9: Q value for Ar^+ with 30 keV beam energy on Ar target. The vertical lines are Argon excited levels from NIST [39] with and without target excitation.

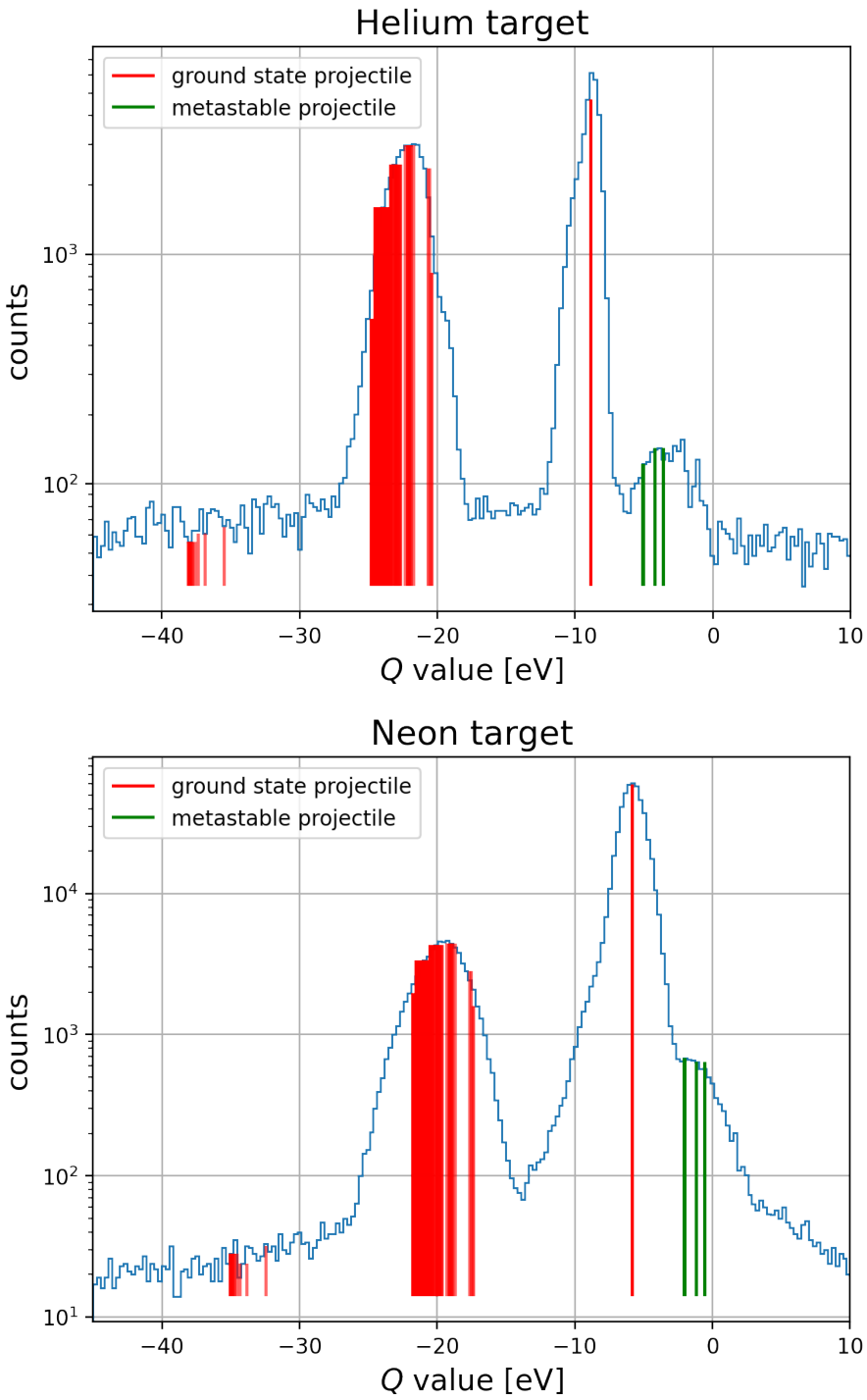

Figure 5.10: Q value for Ar^+ beam with 30 keV beam energy on He and Ne target. The red vertical lines are Argon excited levels from NIST [39] with and without target excitation. The vertical green lines correspond to electron transfer to the $3p$ orbital in the metastable projectile.

an order of magnitude lower than the ground state peak (peak height of about 6100 counts for main peak, 150 counts for small peak). This peak is attributed to electron transfer into a metastable state in the Argon projectile and will be discussed in section 5.3.4.

The neon plot in Fig. 5.10 looks similar to the Helium Q value spectrum with two very distinct peaks corresponding to electron transfer into ground and excited states of the projectile. The ground state peak has a FWHM of 2.0 eV. There is no small peak visible, but the main peak has a shoulder on the right (at about -1.5 eV). It seems like the separation between the small peak to the right of the ground state transition is not as clear and therefore more like a shoulder. This shoulder is again connected to electron transfer into the metastable positive argon ion state and will be discussed in section 5.3.4. As in Helium, there is no sign of a target excitation line for neon target (also not in the 2D detector image).

From the simple CoB model it is surprising to see electron transfer into excited states at all, since these Q values lie outside the expected reaction window calculated in section 5.1.2. Probably, a classical model is not sufficient to describe the system and a full quantum mechanical model is needed.

5.3.4 Electron Transfer into Metastable Ar^+ State

In Fig. 5.14 for both helium and neon target the electron transfer into the $3p$ level of the metastable states (green lines) are marked, see section 5.1.4. The green lines fit to the left edge of the peak for helium target and the shoulder position for the neon target. The $3p$ level is the lowest unoccupied electronic level in the metastable states, capture in higher states would lead to negative Q values with a higher absolute value.

To control if the small peaks with helium and neon target are from electron transfer into the metastable state of the projectile ion, the summed up counts in the respective peaks are plotted relative to storage time in Fig. 5.11. The counts are normalized with the ground state to ground state peak height to take the declining beam intensity into account. The storage time was indirectly determined via the neutralized projectile count rate as described in section 2.9. The dashed and dotted lines correspond to an exponential decay fit

$$y = n_0 \exp(-x/\tau) + c \tag{5.29}$$

with n_0 the start count rate, τ the decay constant and c a background offset. For neon target, the parameters $n_{0,\mathrm{Ne}} = 0.76 \pm 0.04, \tau_{\mathrm{Ne}} = 4.62 \pm 0.36\,\mathrm{s}$ and $c_{\mathrm{Ne}} = 0.11 \pm 0.01$ and for helium target the parameters $n_{0,\mathrm{He}} = 1.21 \pm 0.15, \tau_{\mathrm{He}} = 4.86 \pm 1.05\,\mathrm{s}$ and $c_{\mathrm{He}} = 0.50 \pm 0.04$ are determined. The fit errors are higher for the Helium target data probably because of lower overall statistics for helium target. The averaged lifetime of the five metastable Ar^+ states calculated by Schef et al. [81] is 4.21 s,

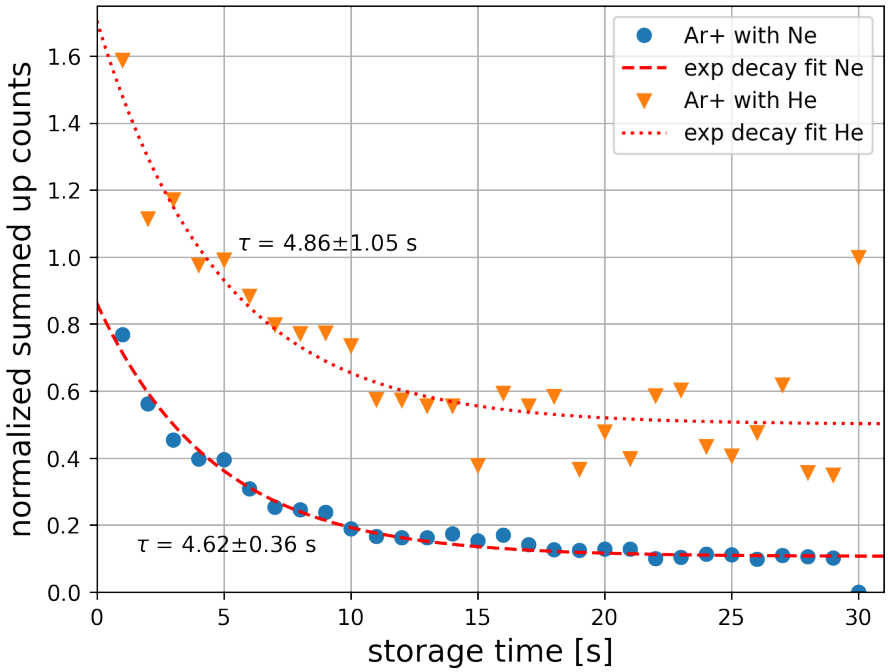

Figure 5.11: Lifetime of metastable peak for He and Ne target. The summed-up counts of the peak attributed to the electron transfer the metastable projectile are normalized with the maximum of the ground-state transition.

but the $^2F_{9/2}$ state has an expected lifetime of 1.25 s (see Tab. 5.1). The averaged lifetime of the four remaining states is 4.95 s. The measured lifetimes from helium and neon target fit both well to the expected averaged lifetime without the $^2F_{9/2}$ state.

5.3.5 Electron Transfer Scattering Angle

Position Correction for Electron Transfer

For the measurements in chapter 3 and 4 the position correction method described in section 2.7 was used to reduce the effective source volume. The transversal momentum transfer in these experiments is fairly small. For collisions with a slow ion beam this is not necessarily the case. For a scattering angle of e.g. 5 mrad, the expected cone diameter on the neutral detector would be about 22 mm or about the same diameter as the ion beam diameter, see Fig. 2.16.

Fig. 5.12 shows the transversal momentum $p_\perp = \sqrt{p_x^2 + p_z^2}$ vs. x_{neut} the neutral detector hit position along the x axis for the different targets. For helium target no correlation between $p_\perp$ and x_{neut} is visible. The argon and neon target plots show a

clear diagonal lines originating from $x_{\text{neut}} = 0\,\text{mm}$ indicating that the x_{neut} position is determined by the transversal momentum. Probably the scattering angle for these heavy targets is too large to be ignored and therefore, the position correction can not be used. The Q value discussion above is not affected by the correlation of the transversal momentum with the x_{neut} position, since the transversal components are projected on the y axis. But for the discussion of the scattering angle, this will lead to a large source volume in x direction, because of the large ion beam diameter, see section 2.7. The source volume will limit the limit the resolution in the transversal direction. The expected scattering-angle resolution is then about 0.55 mrad for argon and neon target and 0.28 mrad for helium target (substantially worse than the 0.16 mrad if $\Delta p_\perp = 2\,\text{a.u.}$ or 0.04 mrad for $\Delta p_\perp = 0.5\,\text{a.u.}$).

To improve the resolution for the transversal momentum components the electron cooler of the CSR could be used in future experiments to cool the transversal momentum components of the ion beam, leading to a smaller ion beam diameter and therefore a smaller source volume. A second possibility would be to use an Abel transform to retrieve the transversal momentum from the projection on the yz plane, since the y and z direction offer small source dimensions. In the following analysis this is not yet implemented.

Scattering Angle vs. Q Value

Fig. 5.13 shows the Q value plotted against the scattering angle for the $\text{Ar}^+ + \text{Ar}$ (a) and the line-outs for the ground state, excited state and target-transfer excitation in (b). The green dashed line marks the edge of the ion detector, for scattering angles above this line no 4π information is available. The scattering angle of the counts detected above the green dashed line is primarily determined by the momentum in z direction. The three lines for electron capture into projectile ground state (1), exited projectile states (2) and exited projectile states with target transfer excitation (3) are marked. (4) marks a diffuse, additional background around the ground state with low scattering angle. The ground state line starts at 0 mrad, has the highest intensity up to around 0.4 mrad and reaches with diminishing intensity up to high scattering angles. The CoB model predicts that the scattering-angle peak intensity is around 0.2 mrad. Considering the expected resolution of 0.55 mrad the position matches well. The slight 'wobble' around 0.5 mrad is a detector artefact, caused by crosstalk in the delay line (cf. Fig. 5.6). The line for transfer into excited projectile states starts at a higher angle of about 1.7 mrad. The target excitation line starts at an even higher scattering angle of 2.9 mrad. It starts to weaken and blend into background at around 6 mrad. The origin of the feature marked with (4) below 1.5 mrad scattering angles around the ground state is not clear, but since it is more spread out than the other features, present for other TOF slices and more intense if the argon dimer TOF peak is selected, it could to come from fragmentation of $\text{Ar}_2{}^+ \longrightarrow \text{Ar}^0 + \text{Ar}^+$ during the flight through the spectrometer. Feature (4) is

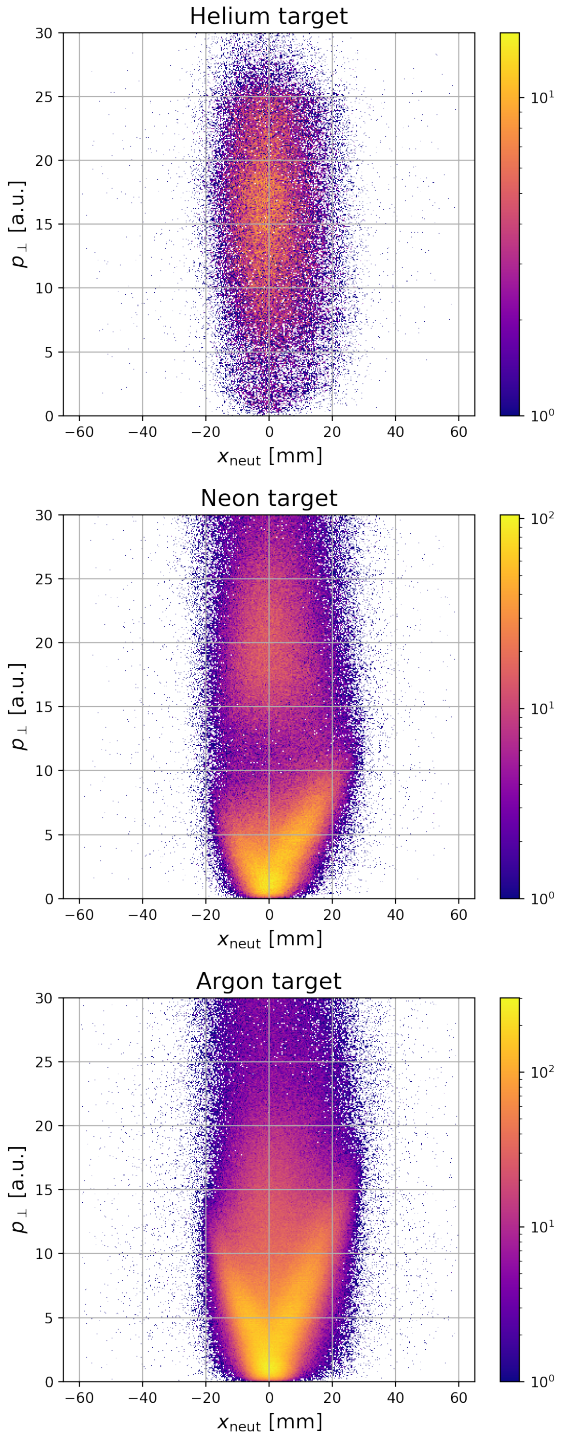

Figure 5.12: Transversal momentum of the recoil ion $p_\perp$ vs. the neutral detector hit position along x axis for Ar^+ beam with 30 keV beam energy on He, Ne and Ar target.

not correlated with the metastable projectile states, since it is not vanishing as the metastable states decay.

Fig. 5.14 shows in (a) the Q value vs. scattering angle and in (b) the line-outs of the different lines for $Ar^+ + He$. In (a) the ground state transition is marked by (1) and excited state capture by (2). (3) marks capture into the projectile in a metastable state and it is only present for small scattering angles. The metastable line blends into the background for scattering angles above around 0.3 mrad. The excited state line starts at around 0.25 mrad and then taper to around 1.25 mrad where it reaches full width with maximum intensity at around 1.4 mrad. It seems like the higher lying states (with higher Q value) only contribute for higher scattering angle. In the CoB model the states with higher Q value are only available for smaller inter-particle distance and at smaller inter-particle distance the transversal momentum is larger leading to larger scattering angle. The ground state line peaks at around 1.1 mrad, but it seems to have a shoulder or a local maximum at around 0.2 mrad, close to the CoB model scattering angle prediction. The peak at 1.1 mrad can not be explained in the CoB model. For values above about 1 mrad, the ground state line also increases its Q value width slightly. There are no other available states close to the ground state and the origin of this is so far unclear. For scattering angles

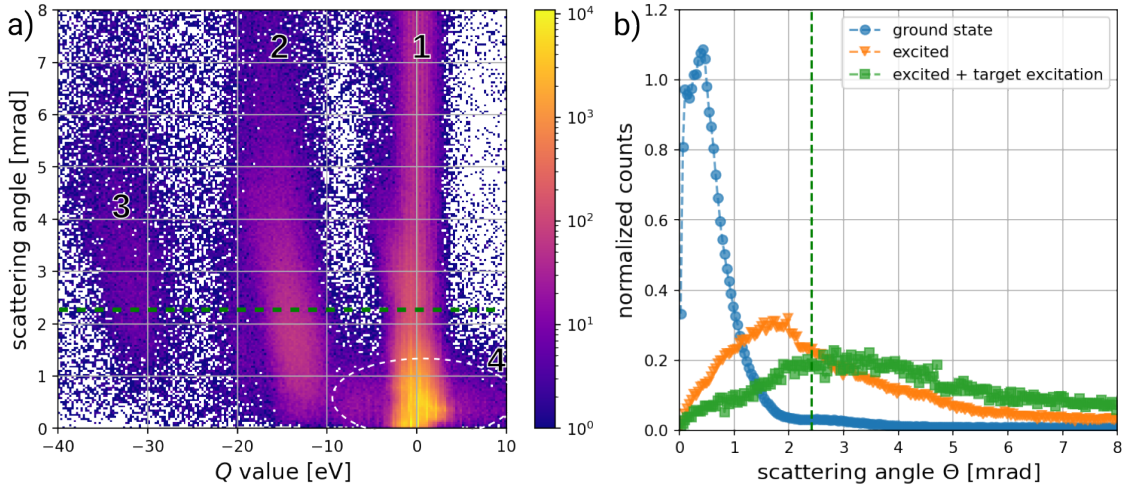

Figure 5.13: a) $Ar^+ + Ar$ Q value vs. scattering angle. (1) marks the ground state transition, (2) the transition to exited projectile states and (3) the target transfer excitation. (4) marks an area of diffuse background around the ground state.
b) Scattering angle line-out for the ground state, excited state and target transfer excitation.
For values with a scattering angle above the green dashed line no 4π detection was possible.

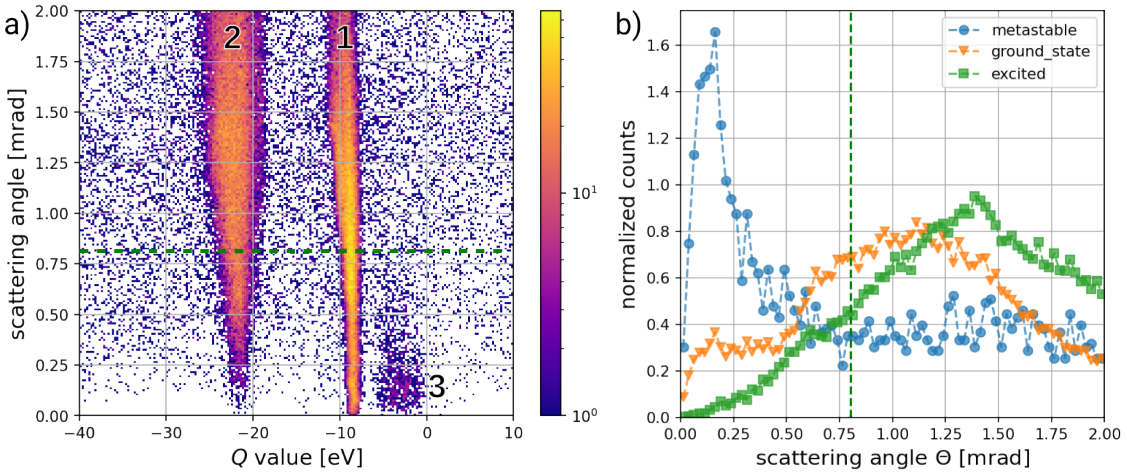

Figure 5.14: a) $Ar^+ + He$ Q value vs. scattering angle. (1) marks the ground state transition, (2) the transition to exited projectile states and (3) transitions into the metastable projectile.
b) Scattering angle line-out of the three lines.
For values with a scattering angle above the green dashed line no 4π detection was possible.

below 0.5 mrad the width of the ground state line is below 1 eV.

For the $Ar^+ + Ne$ collision Fig. 5.15 shows the Q value vs. scattering angle (a) and the line-outs of the different lines (b). For the neon target only events with $p_z < 0$ a.u. are plotted to remove the contribution of the ^{22}Ne isotope. The ground-state (1) and excited-state transitions (2) can be identified in (a). The line seems to be tilted to higher Q values for higher scattering angles. The excited-state line is also slightly tapered like in the helium target case and for scattering angle below 0.5 mrad only a few counts are detected. As for argon target the delay line crosstalk is causing the sharp wobble in the ground-state line below 0.5 mrad. The ground-state line has three distinct oscillations. A classical interpretation of the oscillation, within the CoB model, would be the electrons performing multiple swaps between target and projectile during the collision, a larger impact parameter b (and therefore smaller scattering angle) would lead to a lower number of possible swaps [82, 83, 84]. To identify the process conclusively, probably a dedicated measurement campaign, scanning over the collision energy dependence, and a specific description of the collision system would be needed (like in [73]).

The metastable (3) and the excited states transitions (2) show no oscillation. The transition with the metastable projectile (3) vanish for scattering angles above 1 mrad into background. The Q value of the weak spot, left of the ground state line marked with (4), would fit to target transfer excitation with the metastable argon projectile. No decay over the lifetime of the metastable states is seen, but any decay

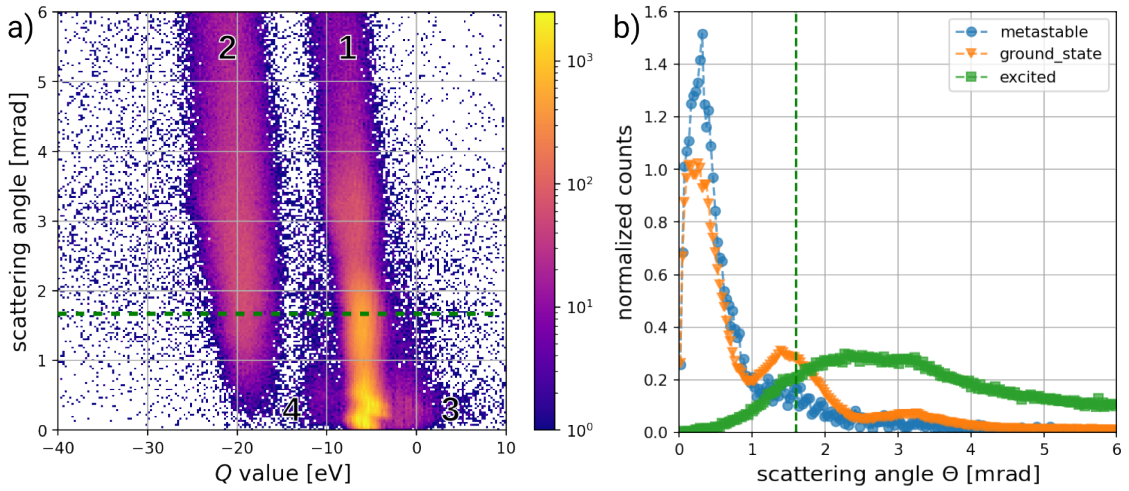

Figure 5.15: a) $Ar^+ + Ne$ Q value vs. scattering angle. (1) marks the ground state transition, (2) the transition to exited projectile states and (3) transitions into the metastable projectile. (4) is not absolutely clear, but would fit to target transfer excitation with the metastable projectile.
b) Scattering angle line out of the three lines.
For values with a scattering angle above the green dashed line no 4π detection was possible. With the condition $p_z < 0$ a.u. to suppress the contribution by ^{22}Ne on the positive side.

could be masked by the low number of counts in the spot.

In conclusion, all major transition lines could be identified. The lifetime of the metastable states of the Ar^+ projectile is within expectation. The scattering angles for the argon and neon ground-state transitions lines agree resaonably well with the CoB model. For the helium target the ground state line peaks at much higher scattering angle than expected, but interestingly the metastable line for helium follows the CoB model expectation. For the neon target ground-state transition line, a clear oscillation with scattering angle was observed. For a clearer understanding, an improved theoretical description would be necessary. Additional measurements with different collision energies and extraction conditions could also be helpful.

6 Summary and Outlook

This thesis describes the reaction microscope for the electrostatic Cryogenic Storage Ring CSR, its setup, function and the first measurements. The CSR-ReMi is a powerful addition to the CSR, allowing for in-ring spectroscopy of electron and recoil ions produced by the interaction of the cold ions stored in the CSR with a neutral gas target or a laser beam. This broadens the scope of experiments possible in the CSR to include, e.g. photo-electron and recoil-ion momentum spectroscopy.

The inner chambers of the nested vacuum system of the CSR can be cooled to cryogenic temperatures of about 5 K. A residual gas density of about 2000 particles/cm^3 in the CSR-ReMi central chamber was estimated from ion-beam recombination with background gas, allowing for almost background free measurements. The CSR-ReMi is build into one of the linear sections of the CSR, the detectors and the spectrometer are completely inside the cryogenic environment, making this the first cryogenic reaction microscope. But the technical realization was facing severe challenges, to comply with the material requirements for a cryogenic, ultra-high vacuum environment and the spatial limitation in the linear section. Additionally, a homogeneous magnetic field is needed for simultaneous detection of electrons and recoil ions and the effect of this field on the ion beam must be fully compensated to not lose the stored ions, since the CSR is electrostatic. In the experiments, the charged particles are created by the interaction of ions stored inside the CSR with a neutral gas target or a laser. By coincidence detection of the charged particles and the neutralized projectiles with position- and time-sensitive particle detectors, a kinematically complete picture of the interaction can be retrieved. The expected trajectories of the recoil ions and electrons to the detectors and the imaging properties of the CSR-ReMi were investigated by a SIMION simulation.

As a proof-of-concept experiment for the investigation of the electronic structure of negative molecules in the cold environment of the CSR, the electron photodetachment capabilities of the CSR-ReMi using CH^- were studied. CH^- was chosen because of the low electron affinity of 1.24 eV and because there are already measurements by e.g. Goebbert et al. [52] available for comparison. The transitions from the ground state of the ion to the ground and excited state of the neutral molecule are identified and match previous experiments by Goebbert et al. Only hints of the metastable anionic $a^1\Delta$ state were seen, probably because its population was to small. Nonetheless, the laser in-coupling and the electron detector work well and different transitions can be identified by the photoelectron momentum spectrum. This proves that the CSR-ReMi can be used for the investigation

of the electronic structure of molecular negative ions. In the future, experiments on the effect of internal de-excitation on the electronic structure of molecular negative ions are possible. To improve the electron energy resolution the setup of a tunable laser system is planned. This allows – for example – interesting contributions to (astro-)chemistry by investigating the behaviour of negatively charged molecules in interstellar clouds.
Another application of photoelectron spectroscopy is the velocity-map imaging (VMI) mode of the CSR-ReMi suggested in [29]. The first experiments testing this idea were prepared and are tested at the end of February 2025 (just as this thesis is submitted). The preliminary results show that the VMI mode is working, further increasing the electron imaging capability of the CSR-ReMi.

Reactions between the stored (negative) ions and a neutral gas target from supersonic gas expansion were studied. By detecting the double or triple coincidence between the neutralized projectile, the ejected electron and/or the recoil ion different reaction channels, like electron loss or target ionization can be distinguished. Here, the electron loss in the $Si^- + Ar$ collision is investigated as an example of this few-body process. The electron loss qualitatively follows the quasi-free electron model, but this model is not sufficient for a full description of the interaction. The process for electron loss with simultaneous target ionization was identified as a correlated interaction between the projectile electron and the target electron. Additionally, the ratio of pure electron loss to electron loss with target ionization exceeds the ratio expected from known cross sections by almost an order of magnitude. This is an exciting discovery, and so far not theoretically explained. Further experiments on this topic with a system more accessible for theoretical calculations like $D^- + He$ are planned for the upcoming beam time in March 2025, together with measurements investigating the collision energy dependence of this process.

The interaction of a positive ion beam with a neutral target was investigated by the electron transfer reactions to an Ar^+ projectile from a He, Ne or Ar target. The final-state energy transfer and the state-dependent scattering angle of the projectile, were retrieved by the coincidence detection of the neutralized projectile and the recoil ion. Electron transfer reactions from the target ground state to the projectile ground state generally have the highest intensity. But also transitions into excited projectile states can be identified for all targets, and for $Ar^+ + Ar$ even target transfer excitation is present. Additional, weak lines for helium and neon targets are identified as capture into the metastable states of Ar^+, since the metastable states de-excite to the ground state over storage time. This shows that already with the current setup the investigation of de-excitation is possible, but it is planned to improve handling and storage-time resolution by an upgrade to the data acquisition system.
Future experiments looking into different collision systems and the energy dependence of transitions are planned.

Many of the 'technical teething troubles' noticed in the first beam time are al-

ready fixed, like several thermal short circuits noticed during cool down to cryogenic temperatures. And for the upcoming beam time, the voltage divider for the spectrometer was replaced with a custom-build 64-channel power supply to be able to freely choose the potential of all spectrometer electrodes. This allows to configure the spectrometer with electrostatic lenses and is essential for the VMI-mode operation.

There are several future upgrades planed, like replacing the current data acquisition system with a more streamlined and flexible system based on the the in-house build FLASH-Cam ADC [85]. This will make it easier to add more online analysis code to reduce the amount of stored data and simplify further data analysis. The addition of a movable charged fragments detector, similar to the COMPACT detectors [36], is also considered, as a step towards the investigation of the complex fragmentation reactions of heavy molecular or cluster ion beams. Also, an expansion of the laser system is planned by first adding more experiment specific fixed wavelength lasers and a tunable laser for more flexibility. Later, a high-power pump-probe setup with HHG for the production of VUV light will be build up, e.g. for the investigation of the electron affinity of cold poly-aromatic carbohydrates which may play an important role in the heating of interstellar clouds.

List of publications

Parts of this thesis have been published or prepared in the following articles

- M. Schulz, F. Herrmann, W. Zhang, D. V. Chicharro, A. Dorn, M. Grieser, F. Grussie, H. Kreckel, O. Novotny, F. Trost, A. Wolf, T. Pfeifer, C. D. Schröter and R. Moshammer, "Multiple differential electron spectra from detachment in collisions of 30-300-keV anions with atoms and molecules", *Phys. Rev. A*, vol. 110, p. 022818, Aug 2024
- F. Herrmann, W. Zhang, M. Schulz, D. V. Chicharro, A. Dorn, M. Grieser, F. Grussie, H. Kreckel, O. Novotny, F. Trost, A. Wolf, T. Pfeifer, C. D. Schröter, and R. Moshammer, "Momentum Imaging of Electron and Recoil Ions from Anion–Neutral Interactions at a Cryogenic Ion Storage Ring", *Phy. Rev. R*, 2025. Accepted.

Bibliography

[1] W. Demtröder, *Atoms, Molecules and Photons*. Berlin: Springer, 2005.

[2] F. Grussie, A. P. O'Connor, M. Grieser, D. Müll, A. Znotins, X. Urbain, and H. Kreckel, "An ion-atom merged beams setup at the cryogenic storage ring," *Review of Scientific Instruments*, vol. 93, p. 053305, 05 2022.

[3] F. M. Pont, A. Bande, E. Fasshauer, A. Molle, D. Peláez, and N. Sisourat, "Impact of the nuclear motion on the interparticle coulombic electron capture," *Phys. Rev. A*, vol. 110, p. 042804, Oct 2024.

[4] K. Lin, S. Eckart, H. Liang, A. Hartung, S. Jacob, Q. Ji, L. P. H. Schmidt, M. S. Schöffler, T. Jahnke, M. Kunitski, and R. Dörner, "Ultrafast kapitza-dirac effect," *Science*, vol. 383, no. 6690, pp. 1467–1470, 2024.

[5] M. Steck and Y. A. Litvinov, "Heavy-ion storage rings and their use in precision experiments with highly charged ions," *Progress in Particle and Nuclear Physics*, vol. 115, p. 103811, 2020.

[6] R. von Hahn, A. Becker, F. Berg, K. Blaum, C. Breitenfeldt, H. Fadil, F. Fellenberger, M. Froese, S. George, J. Göck, M. Grieser, F. Grussie, E. A. Guerin, O. Heber, P. Herwig, J. Karthein, C. Krantz, H. Kreckel, M. Lange, F. Laux, S. Lohmann, S. Menk, C. Meyer, P. M. Mishra, O. Novotný, A. P. O'Connor, D. A. Orlov, M. L. Rappaport, R. Repnow, S. Saurabh, S. Schippers, C. D. Schröter, D. Schwalm, L. Schweikhard, T. Sieber, A. Shornikov, K. Spruck, S. Sunil Kumar, J. Ullrich, X. Urbain, S. Vogel, P. Wilhelm, A. Wolf, and D. Zajfman, "The cryogenic storage ring CSR," *Review of Scientific Instruments*, vol. 87, no. 6, p. 063115, 2016.

[7] O. Novotný, P. Wilhelm, D. Paul, A. Kálosi, S. Saurabh, A. Becker, K. Blaum, S. George, J. Göck, M. Grieser, F. Grussie, R. Hahn, C. Krantz, H. Kreckel, C. Meyer, P. M. Mishra, D. Muell, F. Nuesslein, D. Orlov, and A. Wolf, "Quantum-state–selective electron recombination studies suggest enhanced abundance of primordial HeH +," *Science*, vol. 365, pp. 676–679, 07 2019.

[8] F. Grussie, L. Berger, M. Grieser, A. Kálosi, D. Müll, O. c. v. Novotný, A. Znotins, F. Dayou, X. Urbain, and H. Kreckel, "Merged-beams study of the reaction of cold hd^+ with c atoms reveals a pronounced intramolecular kinetic isotope effect," *Phys. Rev. Lett.*, vol. 132, p. 243001, Jun 2024.

[9] V. C. Schmidt, R. Čurík, M. Ončák, K. Blaum, S. George, J. Göck, M. Grieser, F. Grussie, R. von Hahn, C. Krantz, H. Kreckel, O. c. v. Novotný, K. Spruck, and A. Wolf, "Autodetachment of diatomic carbon anions from long-lived high-rotation quartet states," *Phys. Rev. Lett.*, vol. 133, p. 183001, Oct 2024.

[10] F. Schotsch, I. Zebergs, S. Augustin, H. Lindenblatt, L. Hoibl, D. Djendjur, C. D. Schroeter, T. Pfeifer, and R. Moshammer, "Trapremi: A reaction microscope inside an electrostatic ion beam trap," *Review of Scientific Instruments*, vol. 92, p. 123201, 12 2021.

[11] R. Moshammer, J. Ullrich, M. Unverzagt, W. Schmidt, P. Jardin, R. E. Olson, R. Mann, R. Dörner, V. Mergel, U. Buck, and H. Schmidt-Böcking, "Low-energy electrons and their dynamical correlation with recoil ions for single ionization of helium by fast, heavy-ion impact," *Phys. Rev. Lett.*, vol. 73, pp. 3371–3374, Dec 1994.

[12] G. Schmid, K. Schnorr, S. Augustin, S. Meister, H. Lindenblatt, F. Trost, Y. Liu, M. Braune, R. Treusch, C. D. Schröter, T. Pfeifer, and R. Moshammer, "Reaction microscope endstation at FLASH2," *Journal of Synchrotron Radiation*, vol. 26, pp. 854–867, May 2019.

[13] R. von Hahn, V. Andrianarijaona, J. R. Crespo López-Urrutia, H. Fadil, M. Grieser, C. Haberstroh, V. Mallinger, D. A. Orlov, H. Quack, M. Rappaport, C. D. Schröter, D. Schwalm, J. Ullrich, T. Weber, A. Wolf, and D. Zajfman, "Cryogenic concept for the low-energy electrostatic cryogenic storage ring (csr) at mpi-k in heidelberg," *AIP Conference Proceedings*, vol. 823, pp. 1187–1193, 04 2006.

[14] S. Schippers, "Electron–ion merged-beam experiments at heavy-ion storage rings," *Nuclear Instruments and Methods in Physics Research Section B: Beam Interactions with Materials and Atoms*, vol. 350, pp. 61–65, 2015.

[15] M. Larsson, "Dissociative recombination with ion storage rings," *Annual Review of Physical Chemistry*, vol. 48, no. Volume 48, 1997, pp. 151–179, 1997.

[16] L. H. Andersen, O. Heber, and D. Zajfman, "Physics with electrostatic rings and traps," *Journal of Physics B: Atomic, Molecular and Optical Physics*, vol. 37, p. R57, may 2004.

[17] J. U. Andersen, C. Brink, P. Hvelplund, M. O. Larsson, B. B. Nielsen, and H. Shen, "Radiative cooling of C_{60}," *Phys. Rev. Lett.*, vol. 77, pp. 3991–3994, Nov 1996.

[18] A. P. O'Connor, A. Becker, K. Blaum, C. Breitenfeldt, S. George, J. Göck, M. Grieser, F. Grussie, E. A. Guerin, R. von Hahn, U. Hechtfischer, P. Herwig,

J. Karthein, C. Krantz, H. Kreckel, S. Lohmann, C. Meyer, P. M. Mishra, O. Novotný, R. Repnow, S. Saurabh, D. Schwalm, K. Spruck, S. Sunil Kumar, S. Vogel, and A. Wolf, "Photodissociation of an internally cold beam of ch^+ ions in a cryogenic storage ring," *Phys. Rev. Lett.*, vol. 116, p. 113002, Mar 2016.

[19] C. Meyer, A. Becker, K. Blaum, C. Breitenfeldt, S. George, J. Göck, M. Grieser, F. Grussie, E. A. Guerin, R. von Hahn, P. Herwig, C. Krantz, H. Kreckel, J. Lion, S. Lohmann, P. M. Mishra, O. Novotný, A. P. O'Connor, R. Repnow, S. Saurabh, D. Schwalm, L. Schweikhard, K. Spruck, S. Sunil Kumar, S. Vogel, and A. Wolf, "Radiative rotational lifetimes and state-resolved relative detachment cross sections from photodetachment thermometry of molecular anions in a cryogenic storage ring," *Phys. Rev. Lett.*, vol. 119, p. 023202, Jul 2017.

[20] Technetics Group, "Helicoflex spring-energized metal seals." https://technetics.com/wp-content/uploads/2020/11/TECH_HELICOFLEX-Brochure_v1r3_fnl_low-res.pdf. [Online, Last Accessed: 17.01.2025, 12:20 CET].

[21] S. Mukherjee, P. Panchal, J. S. Mishra, R. Gangradey, P. Nayak, and V. Gupta, "Hydrogen outgassing and permeation in stainless steel and its reduction for uhv applications," *Materials Today: Proceedings*, vol. 44, pp. 968–974, 2021. International Conference on Materials, Processing & Characterization.

[22] P. Chiggiato and P. Costa Pinto, "Ti–zr–v non-evaporable getter films: From development to large scale production for the large hadron collider," *Thin Solid Films*, vol. 515, no. 2, pp. 382–388, 2006. Proceedings of the Eighth International Conference on Atomically Controlled Surfaces, Interfaces and Nanostructures and the Thirteenth International Congress on Thin Films.

[23] Beyond Gravity Austria GmbH, "Cryogenic insulation products." https://www.beyondgravity.com/sites/default/files/media_document/2024-02/Beyond-Gravity-Cryogenic-Insulation-Products_Coolcat_Superinsulation_cryo_ruag%20space.pdf, 01 2023. [Online, Last Accessed: 14.01.2025, 16:10 CET].

[24] Pfeiffer Vacuum GmbH, "Hipace® 300 with tc400, dn 100 cf-f." https://www.pfeiffer-vacuum.com/api/empolis/resource/environment/project1_p/documents/pfeifferSharepointProd/54072-Datasheet_PM%20P03%20904%20C_en.pdf. turbopump, [Online, Last Accessed: 17.01.2025, 15:10 CET].

[25] Agilent Technologies Italia SpA, "Agilent vacion plus 150 pump." https://www.agilent.com/cs/library/datasheets/public/

datasheet-vacion-plus-150-5994-2467en-agilent.pdf, February 2023. Ion Pump, regular version, [Online, Last Accessed: 17.01.2025, 15:00 CET].

[26] J. Ullrich, R. Moshammer, A. Dorn, R. Döner, L. P. H. Schmidt, and H. Schmidt-Böcking, "Recoil-ion and electron momentum spectroscopy: reaction-microscopes," *Reports on Progress in Physics*, vol. 66, pp. 1463–1545, 2003.

[27] H. Schmidt-Böcking, J. Ullrich, R. Dörner, and C. L. Cocke, "The coltrims reaction microscope—the spyhole into the ultrafast entangled dynamics of atomic and molecular systems," *Annalen der Physik*, vol. 533, no. 9, p. 2100134, 2021.

[28] J. Ullrich and V. Shevelko, eds., *Many-Particle Quantum Dynamics in Atomic and Molecular Fragmentation*. Berlin: Springer-Verlag, 2003.

[29] Y. Ben-Shabo, A. Kurbanov, C. D. Schröter, R. Moshammer, H. Kreckel, and Y. Toker, "Velocity map imaging with no spherical aberrations," *Phys. Chem. Chem. Phys.*, vol. 25, pp. 25122–25129, 2023.

[30] allectra GmbH, "Manganin® wire for low temperature applications." https://shop.allectra.com/documents/aKU3xg50h0HOmG8L4YqOLeCFcpik2c5Lsr5KaxNh.pdf/download. [Online, Last Accessed: 17.01.2025, 12:30 CET].

[31] iseg Spezialelektronik GmbH, "Nhs series." https://iseg-hv.com/download/SYSTEMS/NIM/NHS/iseg_manual_NHS_en.pdf, 2022. [Online, Last Accessed: 22.01.2025, 13:20 CET].

[32] sigma3D GmbH. https://www.sigma3d.de/. [Online, Last Accessed: 20.02.2025, 14:20 CET].

[33] J. Ladislas Wiza, "Microchannel plate detectors," *Nuclear Instruments and Methods*, vol. 162, no. 1, pp. 587–601, 1979.

[34] S. Sobottka and M. Williams, "Delay line readout of microchannel plates," *IEEE Transactions on Nuclear Science*, vol. 35, no. 1, pp. 348–351, 1988.

[35] P. Roth and G. Fraser, "Microchannel plate resistance at cryogenic temperatures," *Nuclear Instruments and Methods in Physics Research Section A: Accelerators, Spectrometers, Detectors and Associated Equipment*, vol. 439, pp. 134–137, 01 2000.

[36] K. Spruck, A. Becker, F. Fellenberger, M. Grieser, R. von Hahn, V. Klinkhamer, O. Novotný, S. Schippers, S. Vogel, A. Wolf, and C. Krantz, "An efficient, movable single-particle detector for use in cryogenic ultra-high vacuum environments," *Review of Scientific Instruments*, vol. 86, p. 023303, 02 2015.

[37] iseg Spezialelektronik GmbH, "Nhq high voltage power supplies." https://iseg-hv.com/download/SYSTEMS/NIM/NHQ/iseg_manual_NHQ_en.pdf, 2022. [Online, Last Accessed: 22.01.2025, 13:20 CET].

[38] L. Endres, "Cryogenic characterization of a microchannel plate detector," Master's thesis, Max Planck Institute for Nuclear Physics in Heidelberg, 2020.

[39] A. Kramida, Yu. Ralchenko, J. Reader, and and NIST ASD Team. NIST Atomic Spectra Database (ver. 5.12), [Online]. Available: https://physics.nist.gov/asd [2025, January 18]. National Institute of Standards and Technology, Gaithersburg, MD., 2024.

[40] R. Merritt, C. Purcell, and G. Stroink, "Uniform magnetic field produced by three, four, and five square coils," *Review of Scientific Instruments*, vol. 54, pp. 879–882, 07 1983.

[41] J. T. Bono and J. W. Purpura, "Theoryy behind coil-geometry parameters for fanselau/braunbeck magneti coils," *Naval Surface Warfare Center Panama City Division*, vol. NSWC PCD TR-2017-009, August 2017.

[42] Advanced Measurement Technology, Inc., "Model fta820a octal fast timing amplifier and model fta420c quad fast timing amplifier operating manual." https://www.ortec-online.com/-/media/ametekortec/manuals/f/fta820a-mnl.pdf?la=en&revision=62d8f81c-7bb0-4714-924b-c42eb4733ab1, 2022. [Online, Last Accessed: 23.01.2025, 10:00 CET].

[43] RoentDek Handels GmbH, "Coboldpc software." https://www.roentdek.com/software/CoboldPC/. [Online, Last Accessed: 06.02.2025, 13:55 CET].

[44] G. Scoles, ed., *Atomic and Molecular Beam Methods*, vol. 1, ch. 2 Free Jet Sources. Oxford University Press, 1988.

[45] ACKTAR Ltd., "Coated black foils & films." https://acktar.com/coated-black-foil/?xdomain_data=tb4te0PuMjX5nOsufjufP93jt0egWt47RcxwSZMdFT2gggAQdFlv6tHCHpwiavUN. [Online, Last Accessed: 17.01.2025, 14:35 CET].

[46] Adaptas Solutions, LLC., "Simion software." https://simion.com/. [Online, Last Accessed: 07.02.2025, 11:55 CET].

[47] H. Tawara, T. Kato, and Y. Nakai, "Cross sections for electron capture and loss by positive ions in collisions with atomic and molecular hydrogen," *Atomic Data and Nuclear Data Tables*, vol. 32, no. 2, pp. 235–303, 1985.

[48] T. J. Millar, C. Walsh, and T. A. Field, "Negative ions in space," *Chemical Reviews*, vol. 117, no. 3, pp. 1765–1795, 2017. PMID: 28112897.

[49] A. Sanov and R. Mabbs, "Photoelectron imaging of negative ions," *International Reviews in Physical Chemistry*, vol. 27, no. 1, pp. 53–85, 2008.

[50] R. Mabbs, E. R. Grumbling, K. Pichugin, and A. Sanov, "Photoelectron imaging: an experimental window into electronic structure," *Chem. Soc. Rev.*, vol. 38, pp. 2169–2177, 2009.

[51] A. Kasdan, E. Herbst, and W. Lineberger, "Laser photoelectron spectrometry of ch-," *Chemical Physics Letters*, vol. 31, no. 1, pp. 78–82, 1975.

[52] D. J. Goebbert, "Photoelectron imaging of ch-," *Chemical Physics Letters*, vol. 551, pp. 19–25, 2012.

[53] G. Eklund, M. K. Kristiansson, K. C. Chartkunchand, E. K. Anderson, M. Simpson, R. Wester, H. T. Schmidt, H. Zettergren, H. Cederquist, and W. D. Geppert, "Experimental lifetime of the $a^1\Delta$ electronically excited state of ch^-," *Phys. Rev. Res.*, vol. 4, p. L012016, Feb 2022.

[54] J. S. Coursey, D. J. Schwab, J. J. Tsai, and R. A. Dragoset. Atomic Weights and Isotopic Compositions (version 4.1). [Online] Available: http://physics.nist.gov/Comp [28.01.2025, 15:30 CET].

[55] T. Andersen, "Atomic negative ions: structure, dynamics and collisions," *Physics Reports*, vol. 394, no. 4, pp. 157–313, 2004.

[56] G. Jalbert, W. Wolff, S. D. Magalhães, and N. V. de Castro Faria, "Electron detachment of negative ions: The influence of the outermost electron and its neutral core atom in collision with he, ne, and ar," *Phys. Rev. A*, vol. 77, p. 012722, Jan 2008.

[57] G. M. Sigaud, "Free-collision model calculations for the electron detachment of anions by noble gases," *Journal of Physics B: Atomic, Molecular and Optical Physics*, vol. 41, p. 015205, dec 2007.

[58] K. Fedus, "Elastic scattering of slow electrons by noble gases – the effective range theory and the rigid sphere model," *Atoms*, vol. 9, no. 91, 2021.

[59] J. H. Macek, S. Y. Ovchinnikov, and E. A. Solov'ev, "Energy and angular distributions of detached electrons in a solvable model of ion-atom collisions," *Phys. Rev. A*, vol. 60, pp. 1140–1152, Aug 1999.

[60] J. A. Tanis, E. M. Bernstein, W. G. Graham, M. P. Stockli, M. Clark, R. H. McFarland, T. J. Morgan, K. H. Berkner, A. S. Schlachter, and J. W. Stearns, "Resonant electron transfer and excitation in two-, three-, and four- electron $_{20}Ca^{q+}$ and $_{23}V^{q+}$ ions colliding with helium," *Phys. Rev. Lett.*, vol. 53, pp. 2551–2554, Dec 1984.

[61] M. Scheer, R. C. Bilodeau, C. A. Brodie, and H. K. Haugen, "Systematic study of the stable states of c^-, si^-, ge^-, and sn^- via infrared laser spectroscopy," *Phys. Rev. A*, vol. 58, pp. 2844–2856, Oct 1998.

[62] T. Ferger, D. Fischer, M. Schulz, R. Moshammer, A. B. Voitkiv, B. Najjari, and J. Ullrich, "Mutual ionization in 200−keV $h^- + He$ collisions," *Phys. Rev. A*, vol. 72, p. 062709, Dec 2005.

[63] M. Schulz, F. Herrmann, W. Zhang, D. V. Chicharro, A. Dorn, M. Grieser, F. Grussie, H. Kreckel, O. Novotny, F. Trost, A. Wolf, T. Pfeifer, C. D. Schröter, and R. Moshammer, "Multiple differential electron spectra from detachment in collisions of 30–300-kev anions with atoms and molecules," *Phys. Rev. A*, vol. 110, p. 022818, Aug 2024.

[64] F. Herrmann, W. Zhang, M. Schulz, D. V. Chicharro, A. Dorn, M. Grieser, F. Grussie, H. Kreckel, O. Novotny, F. Trost, A. Wolf, T. Pfeifer, C. D. Schröter, and R. Moshammer, "Momentum imaging of electrons and recoil ions from anion–neutral interactions at a cryogenic ion storage ring," *Phy. Rev. R*, 2025. Accepted.

[65] H. Tawara and T. Kato, "Total and partial ionization cross sections of atoms and ions by electron impact," *Atomic Data and Nuclear Data Tables*, vol. 36, no. 2, pp. 167–353, 1987.

[66] B. Zarour and U. Saalmann, "Multiple electron transfer in slow collisions of highly charged ions and atoms," *Nuclear Instruments and Methods in Physics Research Section B: Beam Interactions with Materials and Atoms*, vol. 205, pp. 610–613, 2003. 11th International Conference on the Physics of Highly Charged Ions.

[67] D. Fischer, B. Feuerstein, R. D. DuBois, R. Moshammer, J. R. C. López-Urrutia, I. Draganic, H. Lörch, A. N. Perumal, and J. Ullrich, "State-resolved measurements of single-electron capture in slow ne7+- and ne8+-helium collisions," *Journal of Physics B: Atomic, Molecular and Optical Physics*, vol. 35, p. 1369, feb 2002.

[68] V. Lepère, I. Ismail, M. Barat, J. Fayeton, Y. Picard, K. Wohrer, C. Jouvet, and S. Martrenchard, "Lifetime and yield of metastable ar-2(+) ions," *The Journal of chemical physics*, vol. 123, p. 174307, 12 2005.

[69] K. B. Blagoev, "Radiative lifetimes of excited ar ii states," *Journal of Physics B: Atomic and Molecular Physics*, vol. 16, p. 33, jan 1983.

[70] A. Niehaus, "A classical model for multiple-electron capture in slow collisions of highly charged ions with atoms," *Journal of Physics B: Atomic and Molecular Physics*, vol. 19, p. 2925, sep 1986.

[71] S. Knoop, *Electron Dynamics in Ion-Atom Interactions*. Phd thesis, Rijksuniversiteit Groningen, 2006.

[72] I. Blank, *Double Electron Transfer in Collisions of Highly Charged Ions and Ultracold Atoms*. Diplomarbeit, Fakult¨at f¨ur Mathematik und Physik, Albert-Ludwigs-Universit¨at Freiburg, 2008.

[73] A. Leredde, A. Cassimi, X. Fléchard, D. Hennecart, H. Jouin, and B. Pons, "Atomic-matter-wave diffraction evidenced in low-energy na^++rb charge-exchange collisions," *Phys. Rev. A*, vol. 85, p. 032710, Mar 2012.

[74] T. Miteva, Y.-C. Chiang, P. Kolorenč, A. I. Kuleff, K. Gokhberg, and L. S. Cederbaum, "Interatomic coulombic decay following resonant core excitation of ar in argon dimer," *The Journal of Chemical Physics*, vol. 141, p. 064307, 08 2014.

[75] Y. K. Bae, J. R. Peterson, A. S. Schlachter, and J. W. Stearns, "Observation of the metastable negative argon ion ar^-," *Phys. Rev. Lett.*, vol. 54, pp. 789–791, Feb 1985.

[76] I. Ben-Itzhak, O. Heber, I. Gertner, and B. Rosner, "Production and mean-lifetime measurement of metastable ar^- ions," *Phys. Rev. A*, vol. 38, pp. 4870–4871, Nov 1988.

[77] L. Yang, D. A. Church, S. Tu, and J. Jin, "Measured lifetimes of selected metastable levels of Ar^{q+} ions (q=2, 3, 9, and 10) stored in an electrostatic ion trap," *Physical Review A*, vol. 50, pp. 177–185, July 1994.

[78] D.-M. Han, Y.-X. Liu, F. Gao, W.-Y. Liu, J. Xu, and Y.-N. Wang, "Measurements of argon metastable density using the tunable diode laser absorption spectroscopy in ar and ar/o2*," *Chinese Physics B*, vol. 27, p. 065202, jun 2018.

[79] Z. Donkó, P. Hartmann, I. Korolov, D. Schulenberg, S. Rohr, S. Rauf, and J. Schulze, "Metastable argon atom kinetics in a low-pressure capacitively coupled radio frequency discharge," *Plasma Sources Science and Technology*, vol. 32, p. 065002, jun 2023.

[80] A. Muller, H. Klinger, and E. Salzborn, "Role of metastable argon ions in ari++ar charge-exchange collisions," *Journal of Physics B: Atomic and Molecular Physics*, vol. 9, p. 291, feb 1976.

[81] P. Schef, A. Derkatch, P. Lundin, S. Mannervik, L.-O. Norlin, D. Rostohar, P. Royen, and E. Biémont, "Lifetimes of metastable levels in Ar II," *Eur. Phys. J. D*, vol. 29, pp. 195–199, May 2004.

[82] K. B. MacAdam, J. C. Day, J. C. Aguilar, D. M. Homan, A. D. MacKellar, and M. J. Cavagnero, "Transient molecular-ion formation in rydberg-electron capture," *Phys. Rev. Lett.*, vol. 75, pp. 1723–1726, Aug 1995.

[83] D. R. Schultz, C. O. Reinhold, and P. S. Krstić, "Analysis of unexplained oscillations in intermediate-energy ion-atom collisions," *Phys. Rev. Lett.*, vol. 78, pp. 2720–2723, Apr 1997.

[84] P. S. Krstic, C. O. Reinhold, and D. R. Schultz, "Interference oscillations in the excitation cross section for slow ion - hydrogen collisions," *Journal of Physics B: Atomic, Molecular and Optical Physics*, vol. 31, p. L155, feb 1998.

[85] F. Werner, C. Bauer, S. Bernhard, M. Capasso, S. Diebold, F. Eisenkolb, S. Eschbach, D. Florin, C. Föhr, S. Funk, A. Gadola, F. Garrecht, G. Hermann, I. Jung, O. Kalekin, C. Kalkuhl, J. Kasperek, T. Kihm, R. Lahmann, A. Marszalek, M. Pfeifer, G. Principe, G. Pühlhofer, S. Pürckhauer, P. Rajda, O. Reimer, A. Santangelo, T. Schanz, T. Schwab, S. Steiner, U. Straumann, C. Tenzer, A. Vollhardt, D. Wolf, and K. Zietara, "Performance verification of the flashcam prototype camera for the cherenkov telescope array," *Nuclear Instruments and Methods in Physics Research Section A: Accelerators, Spectrometers, Detectors and Associated Equipment*, vol. 876, p. 31–34, Dec. 2017.

[86] S. Gibson, D. D. Hickstein, R. Yurchak, M. Ryazanov, D. Das, and G. Shih, "Pyabel/pyabel: v0.9.0," Dec. 2022.

Appendix

A Supplemental

A.1 Breakout Box Circuit Drawing

Fig. A.1 shows the circuit drawing of the breakout box. The breakout box provides the voltages for the individual parts of the detector via a voltage divider and couples the signals from the MCP and the delay line wires out via out-coupling capacities. Tab. A.1 shows a list of example voltages of the ion detector provided by the breakout box voltage divider for 3 kV connected to the HV2 SHV plug of the breakout box (HV1 on ground).

A.2 MCPs

The CSR-ReMi uses rimless Photonis Extended Dynamic Range (EDR) MCPs with 120 mm diameter, a channel diameter of 25 µm, a channel center-to-center distance of 32 µm and a bias angle of 12°. The open area ratio (OAR) of all front MCPs is ≥ 0.65.

A.3 Double Hit Rate

The round trip time around the CSR at 30 keV is $T = 92000\,\mathrm{ns}$ for Ar^+. If a beam cross section area of around $A_{\mathrm{beam}} \approx 1\,\mathrm{cm}^2$ is assumed and with $N_{\mathrm{beam}} \approx 10^8$ argon ions in the ring the ion beam luminosity $\mathcal{L}$ is

$$\mathcal{L} = \frac{N_{\mathrm{beam}}}{A_{\mathrm{beam}} T} \approx 1.087 \cdot 10^{16}\,\mathrm{m}^{-2}\mathrm{s}^{-1} = 1.087 \cdot 10^{12}\,\mathrm{cm}^{-2}\mathrm{s}^{-1}. \tag{A.1}$$

The probability of a beam particle to collied inside the gas jet is given by (from scattering theory mean free path derivation)

$$P = \rho_{\mathrm{jet}} \sigma d \tag{A.2}$$

with $\rho_{\mathrm{jet}} \approx 10^8 \frac{\mathrm{particles}}{cm^3}$ the density of the gas jet, $\sigma = \pi(2r)^2$ the scattering cross section with $r = 0.1\,\mathrm{nm}$ (assumed) and $d \approx 0.5\,\mathrm{mm}$ the diameter of the gas jet.

The drop in intensity $\mathrm{d}I$ corresponds to the event rate, if one assumes that the every collision leads to a charge transfer.

$$\mathrm{d}I = I \cdot P = \mathcal{L} \cdot P = 6829.8\,\mathrm{cm}^{-2}\mathrm{s}^{-1} \tag{A.3}$$

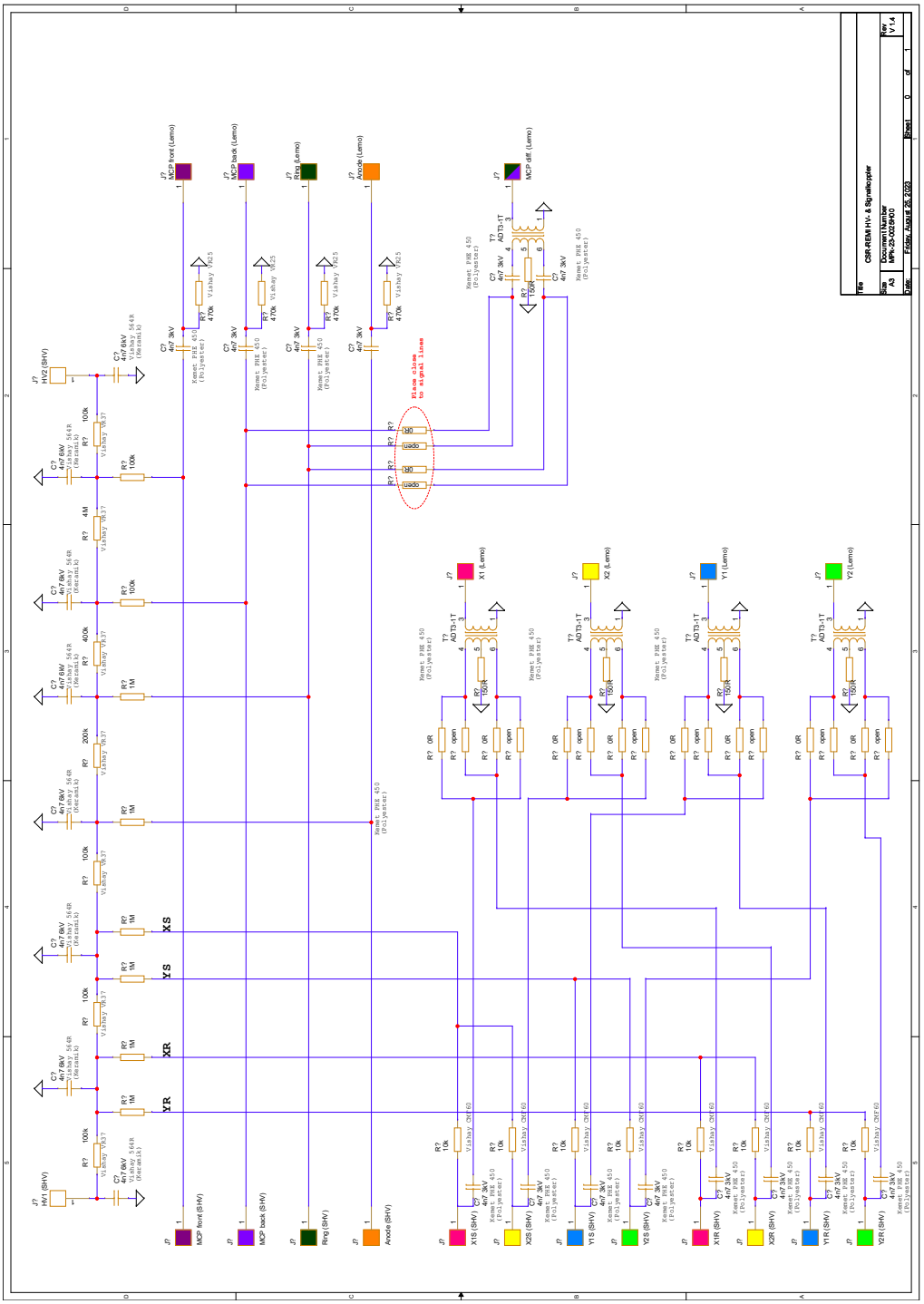

Figure A.1: Circuit drawing of the breakout box. This box contains the voltage divider to supply all detector parts with the needed voltage and couples the signal out and applies a differential amplifier to the signal and reference wires of the delay line anode to subtract the background.

Table A.1: Detector voltages (for ion detector) for 3 kV (max voltage for detector, limit by wire breakdown voltage) input voltage, cf. Fig. A.1 for circuit diagram.

	voltage
HV1	GND
reference wires	75 V
signal wires	150 V
anode plate	225 V
ring anode	375 V
MCP back	675 V
MCP front	2925 V
HV2	3000 V
Grid no2	acceleration or energy filter voltage
Grid no1	spectrometer end voltage

if this is multiplied by the overlap area $A = 5\,\mathrm{mm}^2$ of gas jet and ion beam one gets an count rate of 341.4 Hz for single collision. The recoil ion count rate during the experiments was between 300 Hz and 1 kHz depending on storage time and collision system.

For a double collision the particle needs to collied again, therefore

$$\mathrm{d}I_{\mathrm{double}} = \mathrm{d}I \cdot P = I \cdot P^2 = 4.29 \cdot 10^{-5}\,\mathrm{cm}^{-2}\mathrm{s}^{-1} \tag{A.4}$$

then

$$\mathrm{d}I_{\mathrm{double}} \cdot A = 2.15 \cdot 10^{-6}\,\mathrm{Hz} \widehat{=} \frac{1.3}{\mathrm{week}} \tag{A.5}$$

$\Rightarrow$ double hits are very unlikely.

A.4 2D Projection with Abel Inversion

For the photo-detachment measurement discussed in chapter 3. As already mentioned and used above a reaction microscope can usually reconstruct all three momentum components. But this needs accurate time-of-flight information, if this is not given only the 2D projection is available. The extraction field is increased to 4.9 V/cm to make sure all electrons are collected, the other parameters are the same as in chapter 3. For this extraction field the electrons have only time to make about 2/3 of a turn in their cyclotron motion and the image will be rotated but there is no ambiguity in the electron turn number. Fig. A.2 shows the electron hit position on the left rotated by 290° to align the laser direction with the x axis (−230° to turn back the electron cyclotron motion and −60° because of the angle between ion

beam and laser, a pointing error of 5° for this laser system is possible). In the center the small dot of the zero momentum electrons can just barely been made out. The electron hit position shows at higher radius a two lobe structure like Fig. 3.4. To see if the Δ state is hidden in the projection the image is Abel inverted. On the right the image is Abel inverted using the PyAbel package [86] with the Hansen-Law methode. The dot is also barely visible.

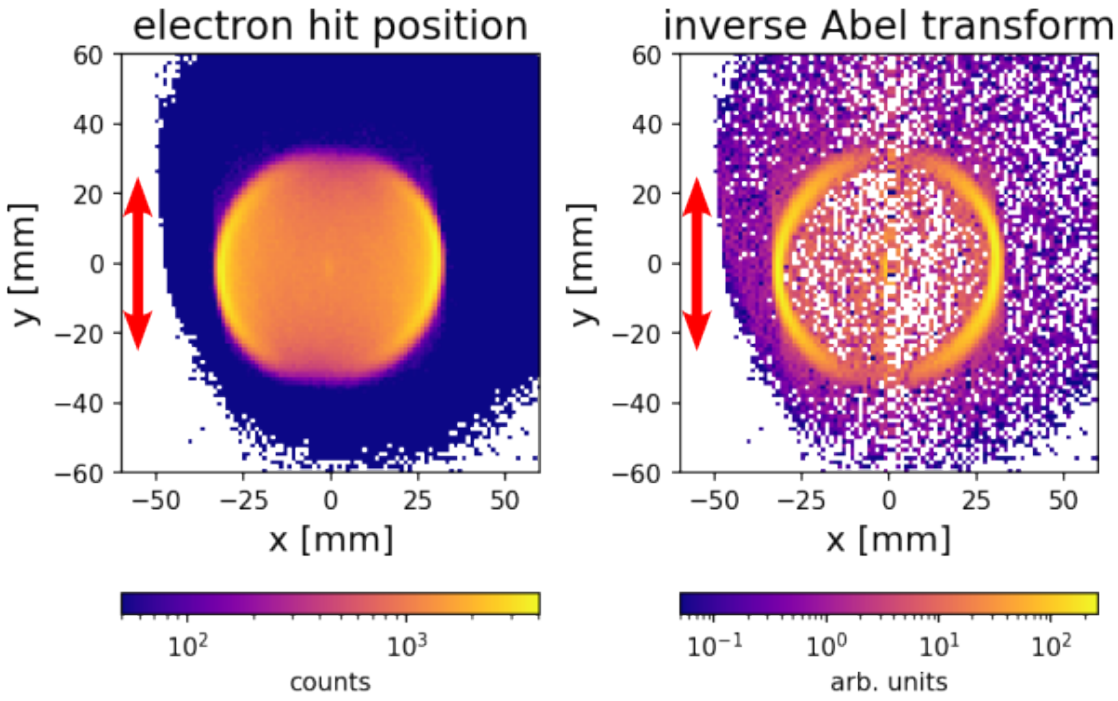

Figure A.2: Electron hit position for 4.9 V/cm extraction field with electron photodetached from CH^- with 60 mW laser power in the xy plane with horizontal laser polarization and Abel inverted image. The images are rotated by $-290°$ to compensate for electron cyclotron motion and align the laser direction with x axis. The red double arrow indicates the laser polarization direction.

B Lists

B.1 List of Figures

B.2 List of Tables

Acknowledgements

Something like this thesis is never really the work of a single person. I would like to thank the many people who helped me along the way.
First, Robert Moshammer, my supervisor, who always took time from his schedule, if I had a question.
Thomas Pfeifer, who was always open for discussions and is now my first referee.
My second referee, Wolfgang Quint, who will hopefully like what's in here, and the other members of my thesis committee Mark Ladd and Tilman Plehn.
Alexander Dorn, for discussions and agreeing to be the third member of my TAC.
My special thanks to Claus Dieter Schröter, with whom I spend a lot of time in the lab, building and testing the CSR-ReMi. And to Michael Schulz, without his insights, this thesis would be a whole lot shorter :-).
I also thank the PostDocs I worked with Patrick Froß and David Chicharro Vacas, and now more recent Md Abul Kalam Azad Siddiki, and my colleagues, especially Weiyu Zhang for a lot of help and enduring me during the beam times.
And no beam times would have happened, if the CSR team wouldn't have adopted me so graciously event-though I build this strange machine into the ring. Thank you Viviane Schmidt, Oldrich Novotney, Florian Grussie, Holger Kreckel, Manfred Grieser, Lukas Berger and all others.
Of cause for everything that works, a technician is needed to make it work, this burden has fallen on Ranko Grimm, Alexander von der Dellen, Manfred König, Max Trebis, Dirk Kaiser, Erik Werner, Natalie Zahn, Christian Kaiser and their co-workers. Together with the team from the precision engineering department under Thomas Spranz and Martin Beckmann, who build all parts I asked for, after the construction department under Frank Müller made me a drawing. Especially Yannick Steinhauser was always ready to help me, when I needed to know if there is space or not.
And, at the end, I want to thank my family, who supported me and in particular, my favourite human Junia Göller ♡.